






Universitat Autònoma de Barcelona

ADVERTIMENT. L'accés als continguts d'aquesta tesi queda condicionat a l'acceptació de les condicions d'ús establertes per la següent llicència Creative Commons:  http://cat.creativecommons.org/?page_id=184

ADVERTENCIA. El acceso a los contenidos de esta tesis queda condicionado a la aceptación de las condiciones de uso establecidas por la siguiente licencia Creative Commons:  <http://es.creativecommons.org/blog/licencias/>

WARNING. The access to the contents of this doctoral thesis it is limited to the acceptance of the use conditions set by the following Creative Commons license:  <https://creativecommons.org/licenses/?lang=en>



**Universitat Autònoma
de Barcelona**

**New perspectives on the glass
transition: Crossover between
cooperative relaxation and liquid growth
dynamics**

Doctoral Thesis submitted by
Ana Vila Costa
to apply for the degree of Doctor in Physics

Supervised by
Dr. Marta González Silveira
and
Dr. Cristian Rodríguez Tinoco

Group of Thermal Properties of Nanoscale Materials
Physics department
November 2022

La Dra. Marta González Silveira, professora agregada del Departament de Física de la Facultat de Ciències de la Universitat Autònoma de Barcelona i el Dr. Cristian Rodríguez Tinoco, professor lector Serra Hunter del Departament de Física de la Facultat de Ciències de la Universitat Autònoma de Barcelona,

CERTIFIQUEN que l'Ana Vila Costa, Graduada en Física per la Universitat Autònoma de Barcelona, i en possessió del Màster oficial en Nanociència i Nanotecnologia Avançades, ha realitzat sota la direcció d'ambdós el treball que porta com a títol *New perspectives on the glass transition: Crossover between cooperative relaxation and liquid growth dynamics*, el qual es recull en aquesta memòria per tal d'optar al Títol de Doctor en Física per la Universitat Autònoma de Barcelona.

Dra. Marta González Silveira
Bellaterra, Novembre 2022

Dr. Cristian Rodríguez Tinoco
Bellaterra, Novembre 2022

Als meus pares

Agraïments

Ja diuen que el més important del viatge no és el destí, sinó el camí seguit fins arribar-hi, i la veritat, no podria estar més agraïda a la gent amb qui m'ha tocat compartir-lo. Al llarg d'aquests darrers anys, que han culminat en aquest treball, he tingut el plaer de coincidir amb una gran quantitat de persones que han fet d'aquesta experiència una de les més enriquidores que he viscut, tant a nivell d'aprenentatge científic com personal. Fent que el camí recorregut fins al final d'aquesta etapa hagi estat ple de dies on, tot i que la feina pogués ser esgotadora, les rialles mai han faltat. Per tot això i més, moltes gràcies a tots.

Per començar, vull agrair a la gent del meu grup de recerca, GTNaM. En especial agrair als meus directors de tesi, la Marta Gonzàlez i al Cristian Rodríguez, per ensenyar-me tant i per estar sempre disposats a ajudar-me quan ho he necessitat. Perquè m'han repetit les coses tants cops com ha sigut necessari, fent-me sentir acompanyada i guiada durant tot el doctorat, i perquè al final del camí, a més de mentors, han esdevingut amics. Gràcies al Javier Rodríguez, per donar-me aquesta oportunitat i per totes les hores dedicades a resolució i discussió de dubtes que m'han servit per aprendre tant. Agrair també a la Gemma Garcia els consells durant la meva primera etapa al grup, tant en matèria científica com per animar-me a intentar tot allò que em semblés interessant. Gràcies a l'Aitor Lopeandía, per tota l'ajuda tècnica que m'ha brindat des del primer moment. Al Jordi Fraxedas per tot el coneixement impartit en AFM i per les llargues hores de mesures. Especials gràcies, com no, a la “dupla” de Martas, Marta Rodríguez i Marta Ruiz (Marta Ro & Marta Ru, Marta Jr & Marta Mini), per les bones estones al laboratori i fora d'ell. A la Marta Jr per saber aguantar-me quan sembla que la ciència ha decidit no voler posar de la seva part o per les hores fent mostres que semblen no acabar mai. Però sobretot gràcies pel suport i les bones estones compartides, pels “viernes de bailoteo al lab” i les infinites rialles durant aquests anys. A la Marta Mini, per la seva simpatia, bon humor i predisposició d'ajudar en el que calgui. Agrair també al Joan, a qui li dec gran part del coneixement que tinc en quant a laboratori, gràcies per tots els consells al principi del doctorat i la predisposició per ajudar-me sempre que m'ha calgut (tot i que fos per videotrucada). Gràcies al Pablo per la seva simpatia, energia contagiosa i ajuda científica. A l'Antonio, per ser tan divertit, perquè quan té un dels seus dies et pot fer riure fins plorar. Al Gustavo, per totes les hores compartides al laboratori, per les nostres “baralles” simulant alguna art marcial inventada quan necessitàvem un descans, així com pel pão de

queijo i el brigadeiro. Gràcies també a la Claudia, l'Ivan, Noa, Roger, Michele, Llorenç, Lluïsa, Hugo, Sara i altres estudiants del grup per la seva simpatia. I would also like to thank Tapas for his help, not only with the microscopy data, but also with any other question that might have come along the way.

Vull estendre el meu agraïment també al personal del departament de física. Al Francesc Pi per les evaporacions i als tècnics, pel suport donat al laboratori durant aquests anys. Especial agraïment a la Dori Pacho i a la Lara González, per ser tan simpàtiques i resolutives en tot moment. Així com a la Camilla i al Miguel per les estones compartides ja sigui anant o tornant amb el bus o quan ens trobàvem per la facultat. Donar les gràcies també al Marcos Rosado i la Jessica Padilla de l'ICN2 per les mesures de SEM i Raig-X.

I would also like to thank Prof. Paeng for giving me the opportunity to join his group during my 3-month international stay. Although it was a short period of time, I was able to learn a new experimental technique surrounded by people eager to learn and always up to help me during my time there. I want to extend my gratitude to all the students in Prof. Paeng's group: 이향석, 김동훈, 김태우, 진태영, 김기명, 이수현 and 김민석, thank you for welcoming me with open arms since the first day I arrived at your lab, for taking me out for lunch and dinner almost every day and for doing your best to communicate with me in English even though you were not comfortable speaking it. 나를 환영해주고 응원해준 모든 친구들에게 감사합니다.

Special thanks to Theo, for his incalculable help and advice in vacuum systems and for always being ready to jump to action in case we found any problem with our experimental set ups.

Per suposat també agrair a totes les persones que en aquests últims anys han compartit part de la rutina amb mi. A les persones que han estat amb mi des de abans de començar el doctorat com la Sandra, l'Helena, la Rosa, el Bernat i el Jordi. Gràcies per el suport i els ànims sempre. A la Jessica i el Xavi, per animar-me a sortir al gimnàs i oblidar-me durant una estona de mesures i anàlisi de dades. Perquè anar al SAF s'ha convertit en una de les parts preferides del meu dia a dia. Gràcies també als companys de pis que durant aquests anys han fet que pugui anomenar "casa" a un piset lluny d'Eivissa. Gràcies Alejandro, Jaume, Laura, Juan, David, Josep i Maria per tant. Agrair també a tots els amics d'Eivissa (Anna Jordi, Anna Juan, Maria Graó, Maria Sala, Lourdes, Cati, Joan,

Jose, Iván, Jordi, Zota), per ser pilars en els que sempre em puc recolzar i que sempre han cregut en la meva capacitat per fer tot allò que em proposés.

I per últim, però no menys important, als meus pares, perquè són les persones que m'impulsen dia a dia a ser la millor versió de mi mateixa i perquè sense el seu suport mai hagués arribat on soc. Mamà, papà, gràcies. Agrair també als meus germans, Martí i Xico, pel seu suport incondicional.

A totes aquelles persones que han contribuït d'una manera o altra en aquesta etapa, moltes gràcies a tots!

Content

Motivation and objectives	1
Chapter 1. Theoretical framework	7
1.1 The glass transition	7
1.2 Slowing down dynamics: Viscosity and Relaxation Time	9
1.3 Two step relaxation process.....	11
1.4 Dynamic heterogeneities and breakdown of the Stokes-Einstein relation	13
1.5 Heat capacity signature of the glass transition.....	14
1.6 Theoretical views of the glass transition.....	17
1.6.1 Adam-Gibbs Theory	18
1.6.2 Goldstein landscape scenario.....	18
1.6.3 Random First Order Transition Theory (RFOT)	19
1.6.4 Mode Coupling Theory (MCT).....	20
1.6.5 Frustration-limited-domains (FLD) theory.....	21
1.6.6 Dynamical Facilitation Theory (DFT).....	21
References.....	23
Chapter 2. Vapor-deposited glasses	27
2.1 Formation mechanism.....	28
2.2 Properties of highly stable glasses	30
2.3 Transformation mechanism in vapor-deposited glasses	33
2.3.1 Front propagation mechanism	33
2.3.2 Bulk transformation mechanism.....	35
References.....	38
Chapter 3. Experimental methods	43
3.1 Physical vapor deposition process	43
3.2 Characterization techniques: the basics	44
3.2.1 Differential scanning calorimetry (DSC)	45
3.2.2 Quasi-adiabatic fast scanning Nanocalorimetry	46
3.2.3 Atomic Force Microscopy (AFM).....	54
3.3 Experimental set up	57
3.3.1 Deposition chamber	57
3.3.2 Experimental set up for nanocalorimetry measurements and measurement protocol.....	61

3.3.3	Experimental set up for DSC measurements.....	65
3.3.4	Experimental set up for AFM measurements.....	66
3.4	Materials.....	67
	References.....	69
Chapter 4.	Access to bulk transformation in thin film vapor-deposited glasses.....	71
4.1	Identification of the transformation mechanism.....	72
4.2	Suppressing the front transformation.....	75
4.3	Summary.....	79
	References.....	80
Chapter 5.	Bulk glass transition in ultrastable glasses.....	81
5.1	Sample preparation and thermal protocol.....	82
5.2	Glass transition in capped thin film ultrastable glasses.....	83
5.2.1	Liquid formation during the isotherm.....	86
5.2.2	Softening of the stable glass.....	89
5.3	Glass transition in UG thick films.....	91
5.4	Dynamics of liquid formation: KJMAE formalism.....	93
5.5	Validity of the KJMAE model on nanocalorimetry specific heat data.....	101
5.6	Summary.....	105
	References.....	107
Chapter 6.	AFM study of the glass transition in capped ultrastable glasses.....	109
6.1	Sample preparation and thermal protocol.....	111
6.2	AFM measurements: localized wrinkling induced by liquid formation.....	112
6.3	Transformation kinetics from thermal wrinkling patterns.....	117
6.3.1	Nucleation rate and growth velocity calculation.....	118
6.4	Summary.....	122
	References.....	124
Chapter 7.	Effect of glass stability on the bulk transformation dynamics.....	127
7.1	Preparation of the samples and thermal protocol.....	128
7.2	Calorimetric measurements.....	129
7.3	Formation and growth of the liquid regions.....	132
7.3.1	Evaluation of front velocity for glasses with different stabilities.....	134
7.3.2	Liquid nuclei formation dynamics.....	139
7.4	Softening of the glass matrix.....	144
7.5	Summary.....	148
	References.....	150

Chapter 8. Crossover between softening and emergence of liquid regions	153
8.1 Sample preparation and thermal protocol	155
8.2 Crossover between equilibrated liquid formation and cooperative relaxation	156
8.3 Summary	163
References.....	164
Chapter 9. Summary	167
List of publications	173

Motivation and objectives

Glasses can be defined as non-equilibrium solids lacking long-range order. Unlike crystals, which have well-defined unit cells that arrange in an ordered pattern in all directions within the material, a glass presents a disordered structure that resembles more closely the structure of a liquid. It is this combination of the microscopic disordered structure (characteristic of liquids) with the macroscopic mechanical properties of solids, what makes glassy systems of critical interest in current and developing technologies. In our everyday lives, we use the term “glass” to describe, primarily, silicate oxide glasses used in applications such as windows, tableware and household appliances. However, the range of materials that fit under the same definition is significantly wider. Metallic glasses, consisting of alloys of two or more components, are responsible for modern power transmission [1] and are finding increasing use in applications due to their excellent properties, such as corrosion resistance or soft magnetism [2]. Glasses are also crucial in the processing of foods [3] and most engineering plastics are amorphous solids, being polymer glasses of great interest as replacements for metals in new commercial aircrafts for instance [4]. Organic glasses have shown to be the basis for organic light emitting diodes (OLEDs) and other organic electronics [5,6], as well as constituting an important field of research in the pharmaceutical industry. It is also remarkable the importance of glassy systems in modern communication technologies, where amorphous silicates for optical fibers play a critical role for high-speed data transmissions. The silicon used in many photovoltaic cells is also amorphous [7] and, curiously, most water in the Universe is also believed to exist in a glassy state [8].

However, despite the large presence of glassy systems in both nature and in an important number of applications, there are still many open questions that makes research on amorphous and non-crystalline solids the focus of lively discussions in the solid-state physics community up to this day. For instance, understanding the physics of glass formation upon cooling a liquid and its converse effect, the transition to a supercooled liquid upon heating the glass, is still a challenge despite the intense experimental and theoretical research over the last 100 years [9]. In fact, Nobel Prize laureate Philip Anderson even referred to it as “the deepest and most interesting unsolved problem in solid-state theory” [10]. The mechanisms governing the drastic slowdown of the

molecular motion (upon cooling) that brings the system to an apparent arrest is one of the primary challenges of glass science and, the large timescales involved, one of the main problems in order to have experimental access to them.

The fast development over the last 15 years of new methodologies to produce highly stable glasses via new experimental [11,12] and simulation techniques [13,14] has led to significant advances in the characterization and study of these amorphous materials. In the experimental field, physical vapor deposition has emerged as a key technique to produce glasses spanning a broad range of stabilities (among other characteristics) by essentially controlling two deposition parameters: deposition rate and deposition temperature. In fact, with the proper deposition conditions glasses with remarkable low energy states can be prepared, gaining access to (until recently) inaccessible regions of the energy landscape. This access to low-energy glasses together with the development of characterization techniques with high temperature and time resolutions made possible, in the recent years, to explore the dynamics of glasses in a wide range of temperatures and stabilities unachievable to date.

This work aims to further deepen the knowledge on the transformation mechanism by which thin film glasses transform into the supercooled liquid after a jump to higher temperatures. This process has been extensively researched for highly stable glasses, whose transformation has been reported to take place via liquid fronts that starts at the free surface/interface and propagate at a constant rate inside the glass [15–20]. However, fewer studies have focused on the homogeneous devitrification of highly stable glasses in the bulk [21–23] once the formation of this front is avoided. This thesis intends to perform a systematic study on this transformation mechanism in hopes to better understand the bulk dynamics in thin film glasses in a wide stability range by means of quasi-adiabatic fast scanning nanocalorimetry, while also providing visual evidence of the process via microscopy techniques.

This manuscript consists of eight chapters:

- In Chapter 1 a brief theoretical framework is provided in order to introduce some of the main concepts that will be addressed in this work. Since the theory on glassy physics is very extensive, we focus mainly on introducing the glass transition and

its basic features, including the slowdown of the dynamics, the two-step relaxation or the jump in heat capacity at the glass transition. The signature of the glass transition during a heat capacity scan is also discussed since calorimetry is the main technique used to characterize the samples in this study. Finally, an overview of the different theoretical views of the glass transition is also presented.

- Chapter 2 is focused on providing a state of the art on vapor-deposited glasses. We present the experimental, theoretical and simulation studies performed to date to provide an overview of the research being done in this area. We also provide detail on how highly stable glasses can be obtained, their formation mechanism and their main properties. Special emphasis will be given to the transformation mechanism of uncapped vapor-deposited glasses into the supercooled liquid when heated above their glass transition temperature.
- In Chapter 3 the characterization techniques used for the development of this work are presented, as well as the experimental set up. Since all the samples studied in this thesis are grown by physical vapor deposition in an ultra-high vacuum chamber, a detailed description of the deposition chamber will be provided. In this chapter, we introduce as well the different characterization techniques. This includes fast-scanning quasi-adiabatic nanocalorimetry, which allows an *in situ* thermal characterization of the vapor-deposited glasses, conventional DSC and Atomic Force Microscopy (AFM).
- Chapter 4 is devoted to the analysis of the front transformation in vapor-deposited glasses. The procedure for identifying the different mechanisms acting during the glass transition is presented and we also show how the transformation front can be blocked using capping layers with a material that has a higher T_g , gaining access to the bulk transformation of highly stable glasses.
- Chapters 5 and 6 analyze the bulk transformation in ultrastable thin film glasses during an isothermal treatment above T_g by means of two different techniques: quasi-adiabatic fast-scanning nanocalorimetry and AFM. Chapter 5 reports the bulk transformation to take place via two competing processes: i) the formation of liquid regions inside the glass that grow transforming the sample and ii) the softening of the yet not transformed glass matrix. The main parameters of the

transformation are inferred from the calorimetric data using the KJMAE model. In Chapter 6 an equivalent study is presented using AFM. This technique allows, by means of wrinkling patterns on the capping material, a direct visualization of the emergence of liquid regions and their growth, as well as the observation of large length scales between initiation sites.

- The main objective of Chapters 7 and 8 is to study the effect of stability in the bulk transformation mechanism of vapor-deposited glasses. Chapter 7 is focused on analyzing the changes in the bulk transformation dynamics of glasses grown at different deposition temperatures (ranging from $0.85T_g$ to T_g). We will see that regardless of the stability, all glasses follow similar dynamics: softening of the glass matrix and emergence of liquid regions. Chapter 8 shows that independently of the experimental protocol followed to obtain the glass (physical vapor deposition or cooled from the liquid phase) the transformation of the glass into the supercooled liquid takes place via the emergence of liquid regions inside the glass as long as, at the measuring temperature, the contrast between the mobility of the liquid regions and the mobility of the glass is high enough.
- The final chapter is dedicated to a general summary and final conclusions of this work.

References

- [1] V. R.V. Ramanan, *Metallic Glasses in Distribution Transformer Applications: An Update*, Journal of Materials Engineering **13**, 119 (1991).
- [2] A. L. Greer, *Metallic Glasses*, Science (1979) **267**, 1947 (1995).
- [3] L. Slade, H. Levine, J. Ievolella, and M. Wang, *The Glassy State Phenomenon in Applications for the Food Industry: Application of the Food Polymer Science Approach to Structure–Function Relationships of Sucrose in Cookie and Cracker Systems*, J Sci Food Agric **63**, 133 (1993).
- [4] C. Soutis, *Carbon Fiber Reinforced Plastics in Aircraft Construction*, Materials Science and Engineering: A **412**, 171 (2005).
- [5] Y. Shirota, *Photo- and Electroactive Amorphous Molecular Materials—Molecular Design, Syntheses, Reactions, Properties, and Applications*, J Mater Chem **15**, 75 (2005).
- [6] S. R. Forrest and M. E. Thompson, *Introduction: Organic Electronics and Optoelectronics*, Chem Rev **107**, 923 (2007).
- [7] S. Sreejith, J. Ajayan, S. Kollem, and B. Sivasankari, *A Comprehensive Review on Thin Film Amorphous Silicon Solar Cells*, Silicon **14**, 8277 (2022).
- [8] P. Jenniskens and D. F. Blake, *Structural Transitions in Amorphous Water Ice and Astrophysical Implications*, Science (1979) **265**, 753 (1994).
- [9] C. A. Angell, K. L. Ngai, G. B. McKenna, P. F. McMillan, and S. W. Martin, *Relaxation in Glassforming Liquids and Amorphous Solids*, J Appl Phys **88**, 3113 (2000).
- [10] P. W. Anderson, *Through the Glass Lightly*, Science (1979) **267**, 1610 (1995).
- [11] S. F. Swallen, K. L. Kearns, M. K. Mapes, Y. S. Kim, R. J. McMahon, M. D. Ediger, T. Wu, L. Yu, and S. Satija, *Organic Glasses with Exceptional Thermodynamic and Kinetic Stability*, Science (1979) **315**, 353 (2007).
- [12] M. D. Ediger, *Perspective: Highly Stable Vapor-Deposited Glasses*, Journal of Chemical Physics **147**, (2017).
- [13] L. Berthier, D. Coslovich, A. Ninarello, and M. Ozawa, *Equilibrium Sampling of Hard Spheres up to the Jamming Density and Beyond*, Phys Rev Lett **116**, 238002 (2016).
- [14] A. Ninarello, L. Berthier, and D. Coslovich, *Models and Algorithms for the Next Generation of Glass Transition Studies*, Phys Rev X **7**, 21039 (2017).
- [15] D. M. Walters, R. Richert, and M. D. Ediger, *Thermal Stability of Vapor-Deposited Stable Glasses of an Organic Semiconductor*, J Chem Phys **142**, 134504 (2015).
- [16] J. Ràfols-Ribé, M. Gonzalez-Silveira, C. Rodríguez-Tinoco, and J. Rodríguez-Viejo, *The Role of Thermodynamic Stability in the Characteristics of the Devitrification Front of Vapour-Deposited Glasses of Toluene*, Phys. Chem. Chem. Phys **19**, 11089 (2017).
- [17] C. Rodríguez-Tinoco, M. Gonzalez-Silveira, J. Ràfols-Ribé, A. Vila-Costa, J. C. Martinez-Garcia, and J. Rodríguez-Viejo, *Surface-Bulk Interplay in Vapor-Deposited Glasses: Crossover Length and the Origin of Front Transformation*, Phys Rev Lett **123**, (2019).

- [18] S. Léonard and P. Harrowell, *Macroscopic Facilitation of Glassy Relaxation Kinetics: Ultrastable Glass Films with Frontlike Thermal Response*, J Chem Phys **133**, 244502 (2010).
- [19] A. Wisitsorasak and P. G. Wolynes, *Dynamical Heterogeneity of the Glassy State*, J Phys Chem B **118**, 7835 (2014).
- [20] R. Gutiérrez and J. P. Garrahan, *Front Propagation versus Bulk Relaxation in the Annealing Dynamics of a Kinetically Constrained Model of Ultrastable Glasses*, Journal of Statistical Mechanics: Theory and Experiment **2016**, 074005 (2016).
- [21] K. L. Kearns, M. D. Ediger, H. Huth, and C. Schick, *One Micrometer Length Scale Controls Kinetic Stability of Low-Energy Glasses*, J Phys Chem Lett **1**, 388 (2010).
- [22] J. Ràfols-Ribé, A. Vila-Costa, C. Rodríguez-Tinoco, A. F. Lopeandiá, J. Rodríguez-Viejo, and M. Gonzalez-Silveira, *Kinetic Arrest of Front Transformation to Gain Access to the Bulk Glass Transition in Ultrathin Films of Vapour-Deposited Glasses*, Physical Chemistry Chemical Physics **20**, 29989 (2018).
- [23] C. Rodríguez-Tinoco, J. Ràfols-Ribé, M. González-Silveira, and J. Rodríguez-Viejo, *Relaxation Dynamics of Glasses along a Wide Stability and Temperature Range*, Sci Rep **6**, 35607 (2016).

Chapter 1

Theoretical framework

1.1 The glass transition

Glasses are usually obtained by cooling the liquid from above the melting temperature of the material, T_m , at a pace fast-enough to bypass crystallization [1,2]. At temperatures above T_m , the material is in the liquid state with the corresponding enthalpy, entropy and specific volume of this equilibrium state. As the temperature is lowered these state variables experience a continuous decrease with temperature as depicted in Figure 1.1. Further cooling the sample, around T_m , the system can undergo a first order phase transition towards the crystal phase, experiencing a sudden drop in its enthalpy/entropy/volume. However, if the liquid can be driven below T_m without crystallizing, the system enters in the supercooled liquid regime, a metastable state. Upon further cooling this liquid phase, both viscosity and the structural relaxation time increase considerably [3–6], producing a slowing down of the molecular motions. Eventually, the molecules/atoms rearrange so slowly that they cannot efficiently sample configurations in the given laboratory timescale and the system moves out-of-equilibrium, becoming a glass. This slowing down of the dynamics can be observed in Figure 1.1 by the change in the rate at which the enthalpy and volume evolve upon cooling. The temperature at which this falling out-of-equilibrium takes place is known as the glass transition temperature, T_g , and it is material dependent. However, even for the same material this temperature is not unique and it changes depending on the cooling rate [5–8]. If the system is rapidly cooled, the time provided for the molecules to rearrange is limited and the system will fall out-of-equilibrium at higher temperatures (glass I in Figure 1.1) than a liquid that is

slowly cooled, which will have more time to explore lower energy configurations allowing the sample to stay in equilibrium until lower temperatures (glass II in Figure 1.1). There is not, therefore, a single glassy state as the thermodynamic (and dynamic) properties of the glass will depend on the thermal history of the sample. The dependence of T_g with the cooling rate is weak, in general, with changes of 3-5°C when the cooling rate changes by an order of magnitude [9]. Below the glass transition temperature, almost all molecular motion ceases, except for thermal vibrations.

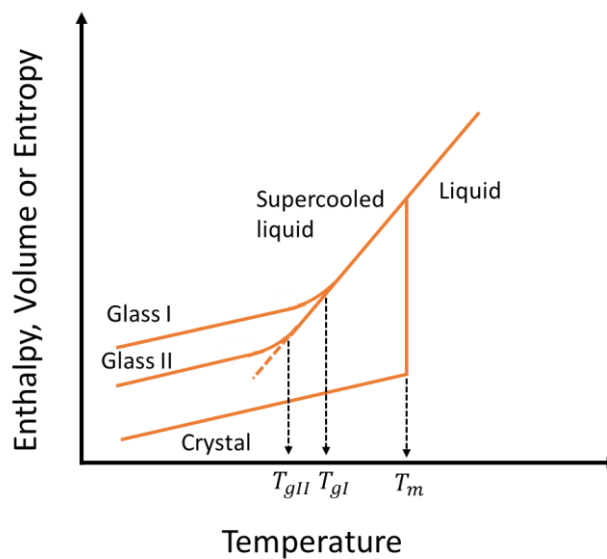


Figure 1.1. Schematic representation of the enthalpy evolution as a function of temperature (also valid for entropy and volume). When cooling the liquid from $T > T_m$, if the cooling rate is fast enough, crystallization is avoided and the liquid enters in the supercooled liquid regime. By further cooling, mobility is arrested and the system is not able to follow the equilibrium line, becoming a glass. The temperature at which the system falls out-of-equilibrium defines the glass transition temperature, T_g . The thermodynamic and dynamic properties of a glass depend on the cooling rate. In this case glass I was obtained by cooling at a faster rate than glass II.

One of the most important consequences of falling out-of-equilibrium during the glass transition is the breakdown of the ergodicity of the system. At T_g , the number of degrees of freedom accessible is suddenly reduced, causing a sharp drop (up to a factor 2) [10] of the constant pressure specific heat, c_p , to a value comparable to that of the crystalline solid (as it can be observed in Figure 1.2). In this case, the system loses the capacity to sample a representative fraction of the phase space in the experimental time scales and, therefore, we can say that the system is no longer ergodic. It is important to consider that,

differently from the transition from liquid to crystal in which the ergodicity is broken as a result of a true thermodynamic phenomenon (first order transition), in the case of glasses, the ergodicity is just dynamically broken in the sense that the system is only capable of exploring a small region of local minimums in the configurational space.

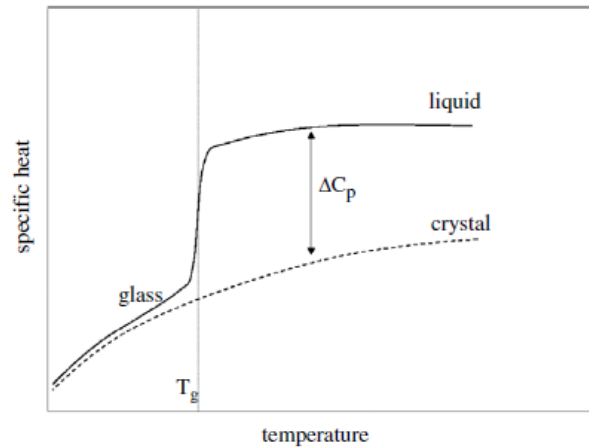


Figure 1. 2. Specific heat as a function of temperature during the glass transition. The jump from the liquid to the glassy phase is indicative of the reduction of the accessible number of degrees of freedom. The dashed line is the specific heat of the crystal phase. Figure reprinted from [10].

1.2 Slowing down dynamics: Viscosity and Relaxation Time

T_g can also be defined in terms of the structural relaxation time, τ_α (also known as alpha relaxation). The relaxation time is considered as the characteristic time needed for a system to go back to its equilibrium configuration after an external perturbation. For example, after stress is applied on a system due to an imposed deformation, the return to equilibrium does not take place immediately, but the process requires a certain amount of time. The relaxation time, which is temperature dependent, governs the dynamics of such change. Glasses are out-of-equilibrium systems and, therefore, their evolution with time will also be controlled by the different relaxation times present in the glass.

Upon decreasing temperature, the relaxation time of a liquid increases much faster the closer to the glass transition, reaching relaxation times several orders of magnitude higher when falling out-of-equilibrium and becoming a glass, all the while undergoing minute changes in the microscopic structure [11]. The temperature at which the relaxation time

of the material exceeds the experimental time available for the observer is considered as another way to define the glass transition temperature, T_g , and by convention is chosen at 100s [6].

The dependence of the relaxation time with temperature, however, can differ significantly from one material to another [6]. As it can be observed in Figure 1.3, the rate at which the relaxation time changes with temperature, upon approaching the glass transition temperature from the liquid, changes depending on the characteristics of the system. This representation, logarithm of the relaxation time (or viscosity) as a function of T_g/T , is known as the Angell plot and it allows us to classify the glass formers according to its strong or fragile nature [12]. Materials such as silica fall in the class of “strong” glass formers, exhibiting an Arrhenius-type (exponential) growth of the relaxation time upon cooling, i.e.,

$$\tau = \tau_0 \exp(E/k_B T) \quad (1.1)$$

where T is the temperature, τ_0 is a pre-factor and E the activation energy (both temperature-independent) and k_B is the Boltzmann constant. “Fragile” materials, however, have an even more drastic slow-down close to the glass transition temperature, where the relaxation time (or viscosity) varies in a super-Arrhenius fashion. The viscous slowdown in these systems is often well described by the phenomenological Vogel-Tammann-Fulcher (VFT) equation [13]:

$$\tau = \tau_0 \exp\left(\frac{DT_0}{T-T_0}\right) \quad (1.2)$$

where τ_0 is a temperature-independent constant and T_0 depends on the fragile or strong nature of the system, ranging from 0 (for ideal strong systems) to higher values (for more fragile systems). The parameter D , called the strength parameter, is linked with the fragility of the system, higher values of D are typically correlated with more fragile systems. The relaxation time increases when approaching T_0 , diverging at $T = T_0$.

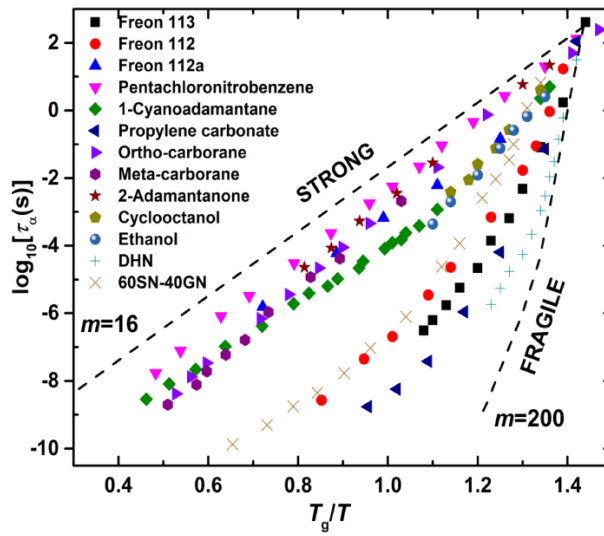


Figure 1.3. Angell's plot for the relaxation time of different systems. The logarithm of transformation time is represented versus the inverse of temperature, normalized by the glass transition temperature of each material. Figure reprinted from [14].

Along with relaxation time, viscosity, η , is another important property in the study of glass-forming liquids and the glass transition. Viscosity, relaxation time and shear modulus, G_∞ , are related by the equation:

$$\eta = G_\infty \tau \quad (1.3)$$

The viscosity of the liquid is proportional to the relaxation time and roughly follows the same temperature dependence since the variation of G_∞ with temperature is not as pronounced as that of the relaxation time. Therefore, in a similar way to relaxation time, the viscosity of a supercooled liquid grows abruptly when approaching the glass transition. Although Equation 1.3 is strictly valid only for Maxwell liquids (shear stress has only one exponential relaxation time) the proportionality between viscosity and relaxation time ($\eta \propto \tau$) is assumed for all glass formers [10].

1.3 Two step relaxation process

One of the main characteristics that defines a supercooled liquid approaching the glass transition is the emergence of a two-step relaxation process [10,15]. In a normal high temperature liquid, the correlations between particles decay to zero in a rapid and simple exponential fashion since they can move freely and, therefore, decorrelate easily of their initial positions (see Figure 1.4 at high temperatures $T=5.0$). However, when lowering the

temperature, a fast-initial decay is observed followed by the emergence of a plateau which remains constant during a certain time, indicating the transient freezing of particles. Only at sufficiently long times the correlation function will completely decorrelate, fully decaying to zero. The faster initial relaxation corresponds to the β -relaxation process, and it is related to non-collective atomic movements, like the vibration of the molecules around equilibrium positions in the glass matrix. In contrast, the slowest phenomenon, that can be seen after the plateau in Figure 1.4, corresponds to the primary or α -relaxation. This relaxation involves a cooperative rearrangement of the structural units that seek thermodynamic equilibrium. Interestingly, this final decorrelation process is not a simple exponential decay (as in high temperature liquids) but rather a slower decay, which can often be described by the stretched exponential or Kohlrausch-Williams-Watts (KWW) function [16,17]:

$$C(t) = \exp \left[- \left(\frac{t}{\tau} \right)^\beta \right] \quad \beta < 1 \quad (1.4)$$

where $C(t)$ can be any correlation function, τ is the characteristic relaxation time of the system, whose temperature dependence is often non-Arrhenius (characteristic of fragile liquids) and β is the stretched exponent. This slowing down of the decorrelation function contrasts with the behavior of liquids above the melting point, where the exponent β has a value close to 1. That is, the system can be described by a simple exponential relaxation [6]. However, for a typical fragile glass former, β decreases with temperature as it approaches T_g , showcasing a non-exponential behavior which suggests the existence of a broad distribution of relaxation times.

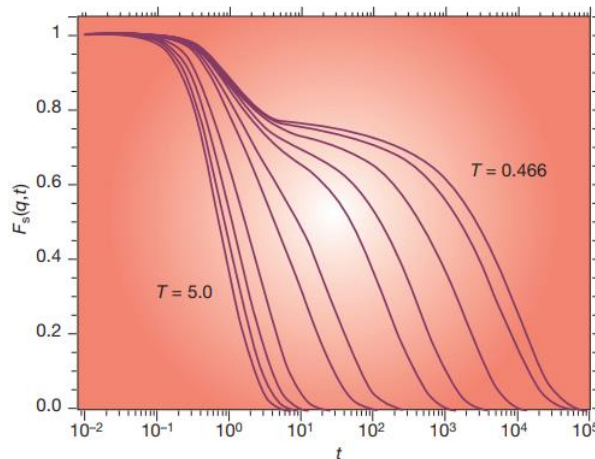


Figure 1.4. Typical two-step relaxation process of the intermediate scattering function observed for liquid and glassy systems when approaching the glass transition. In this case, the temperature is given in computational units. At high temperatures ($T=5.0$), the system relaxes following a single stretched exponential function. As temperature decreases, a two-step relaxation process can be observed with the appearance of a plateau at intermediate times. The fast relaxation before the plateau corresponds to the β -relaxation. Figure reprinted from [6].

1.4 Dynamic heterogeneities and breakdown of the Stokes-Einstein relation

The stretched exponential nature of the α -relaxation (Equation 1.4) is often interpreted in terms of a mixture of exponential functions with different local relaxation time, reflecting the coexistence of regions with slower and faster relaxation dynamics in the glass, that is the presence of dynamic heterogeneities. This phenomenon describes a heterogeneous dynamic structure in the glass with regions of dynamically arrested particles (strongly correlated with their neighbors), and clusters of higher mobility rearranging particles. From the dynamic heterogeneity point of view, therefore, there is a set of different environments in the system, each one relaxing at a different rate. Whether each of these spatially heterogeneous domains relaxes exponentially or not is still object of debate and a matter of considerable current interest [18,19]. Computer simulations [20], as well as experimental [18] and theoretical studies [21,22], have played a central role in establishing the existence of these spatiotemporal fluctuations in the dynamics. It has been seen that near T_g , this heterogeneity can lead to regions with relaxation times that differ by orders of magnitude between points separated only a few nanometers [19,23].

It is also interesting to see how this phenomenon, initially found in supercooled liquids, has been shown to be common for many systems that undergo glass transitions, such as colloid and granular media [24–26], active matter [27,28] and even some quantum systems [29,30].

One of the most striking consequences of dynamic heterogeneity is the violation of the Stokes-Einstein (SE) relation between the diffusion coefficient and the viscosity. According to this relationship, above the melting temperature of a material viscosity, η , and diffusion coefficient, D , are related as [10],

$$D \sim \frac{T}{\eta} \quad (1.5)$$

However, when we approach T_g ($1.2T_g$ and below) the self-diffusion coefficient D decreases at a slower pace compared with the sharp increase in viscosity, showing a decoupling of these two parameters that gets accentuated as the temperature is lowered [31]. Cicerone and Ediger [32] explained this phenomenon by proposing that diffusion is dominated by fast regions, while the slow regions dominate the structural relaxation and, therefore, the viscosity.

1.5 Heat capacity signature of the glass transition

Heat capacity, C_p , is probably one of the most broadly used magnitudes to study the glass transition. The heat capacity can be defined as the amount of heat that needs to be supplied to a system to increase its temperature by one Kelvin, where heat refers to the amount of energy transferred to the system without exerting any work. The magnitude usually used to measure C_p is the specific heat capacity (or simply specific heat), c_{sp} , which is defined as the heat capacity per unit mass.

Heat capacity can give us important information regarding the physico-chemical properties of the glass. The change in heat capacity during the glass transition yields a characteristic curve that gives information regarding the kinetic and thermodynamic state of the system. Information such as, entropy, enthalpy or phase transition temperatures can be obtained.

The glass transition signature in heat capacity measurements consists of a jump (orange dashed line in Figure 1.5a) due to the reduction in the number of degrees of freedom

available when the system falls out-of-equilibrium, as already seen in Section 1.1. Typically, the heat capacity in glasses is measured during heating temperature ramps. Therefore, it is the devitrification process what is usually measured rather than the formation of the glass.

Figure 1.5a (solid blue curve) shows an example of the heat capacity curves obtained during the devitrification process of a glassy system. From this heating temperature scan several kinetic and thermodynamic properties of the sample can be obtained, being the most significant ones the onset devitrification temperature and the fictive temperature, intimately related to the kinetic and thermodynamic stability of the samples, respectively.

The onset temperature, T_{on} , is the temperature at which the devitrification starts, and it depends on the characteristics of the glass and the conditions of the experiment (i.e., the thermal history of the sample and the heating rate). Since the formation and devitrification of a glass are kinetic events, different cooling and heating rates would yield different transition temperatures. In contrast with the glass transition temperature, defined in terms of the transition from liquid to glass in cooling, the onset temperature is used when referring to the transition from glass to liquid in heating. These two parameters, T_g and T_{on} , typically match when both the cooling and subsequent heating are performed at the same rate (neglecting aging effects, i.e., stabilization of the glass below T_g). However, if the heating rate is lower or higher than the cooling rate, the system will have more or less time to relax towards equilibrium, giving raise to shifts of this devitrification onset towards lower or higher temperatures, respectively.

The onset temperature is associated to the kinetic stability of the glass. Glasses which are kinetically more stable will require higher temperatures or times, when heated at the same heating rate, to go back to equilibrium, delaying the onset of the devitrification process.

In addition to the heat capacity jump, the heating scan can also be characterized by a peak overshoot (as showed by the solid blue line in Figure 1.5a). The area of this peak is the excess enthalpy and it is related to the thermodynamic stability of the system. The thermodynamic stability of the glass can be quantified from the enthalpy curve via a parameter called the limiting fictive temperature, T_f , which can be defined as the temperature at which a property of the glass (enthalpy, volume, density, etc.) is equal to that of the supercooled liquid [35,36].

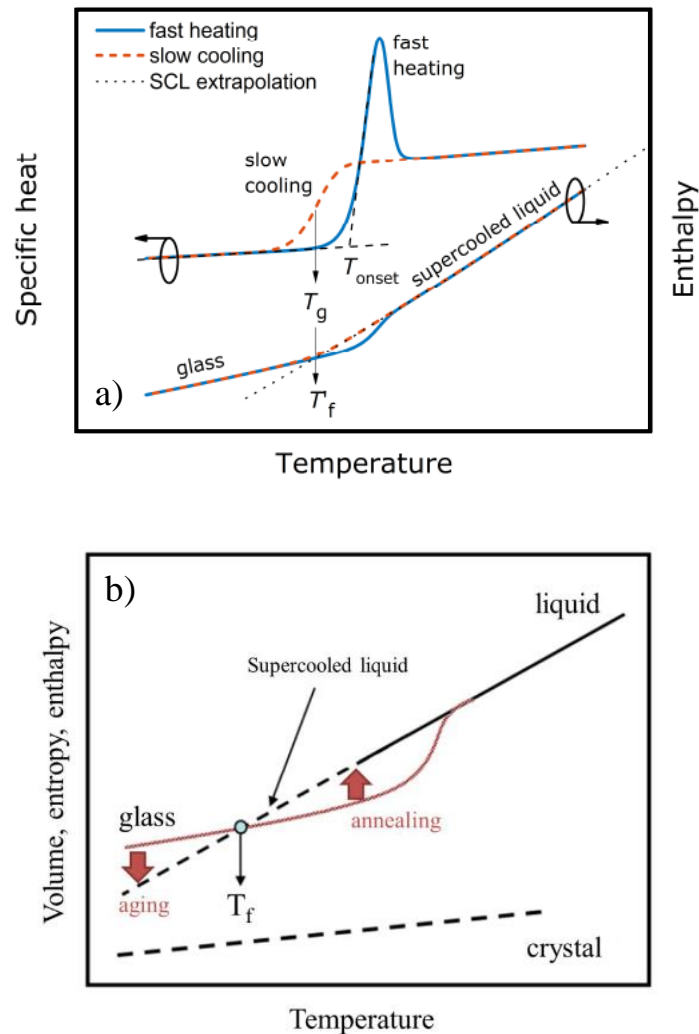


Figure 1. 5. a) Representation of the specific heat signature of the glass transition during a slow cooling (top dashed line) and a subsequent faster heating rate ramp (top solid line). The curves on the bottom represent the corresponding enthalpy for both cooling/heating processes. The black dashed curve corresponds to the SCL extrapolation line. b) Enthalpy (entropy and volume) as a function of temperature. The intersection between the enthalpy of the glass and the enthalpy of the liquid extrapolated at low temperatures defines the limiting fictive temperature, T_f . Below this temperature, the glass increases its stability with time via physical aging, while above T_f , the glass will rejuvenate into the liquid state. Figure adapted from [33] and [34].

From calorimetric measurements, the enthalpic T_f is evaluated from the intersection between the enthalpy of the glass, obtained from the integration of the heat capacity curve, and the extrapolation of the enthalpy of the supercooled liquid line at low temperatures. In this case, the lower the T_f , the higher the thermodynamic stability of the glass. T_f can also be evaluated from the specific heat data using the so-called area matching method

proposed by Moynihan *et al.* More details on this calculation method can be found elsewhere [36].

As we already discussed, the glass transition is a dynamic event that leaves the system in an out-of-equilibrium state. As a consequence, the glasses will evolve continuously towards its equilibrium phase (i.e., the supercooled liquid state), gaining or losing stability and, therefore, changing the overall value of T_f . The process by which a glass relaxes towards a more stable configuration (lower T_f) during an isotherm is known as (physical) aging [4,5,37]. On the contrary, rejuvenation [22,38], anti-aging [39] or devitrification refers to the process by which the glass evolves towards the equilibrium supercooled liquid, even if it corresponds to a less stable configuration (higher T_f), during an isothermal annealing above its fictive temperature (see Section Figure 1.5b).

It is important to note that the fictive temperature provides a global parameter to define the stability of the glass. However, as we have seen in Section 1.4, glasses present spatially heterogeneous dynamics that are manifested by clusters of different mobility, which implies a distribution of relaxation times. Therefore, strictly speaking, the system does not have a unique, macroscopic T_f , but rather a distribution of fictive temperatures [22].

1.6 Theoretical views of the glass transition

Understanding the physics of glass formation remains one of the major unsolved challenges of condensed matter science that persists to this day. The main difficulty stems from the apparent disagreement between the minimal structural changes and the huge variations of the dynamics across the glass transition. The complexity to explain this simple observation can be grasped from the many divergent views and associated models and theories that have been developed over the years to try to explain it from various perspectives [6,40–45]. Interpretations of this dramatic slowdown of the structural relaxation time in supercooled liquids upon cooling across the glass transition temperature can be broadly divided into two competing categories [41]: thermodynamic and kinetic. The first one defends that the kinetic slowdown in the supercooled liquid is due to the presence of an underlying “ideal” (thermodynamic) glass transition [4,44], closely linked to the emergence of a growing static correlation length. Contrary, the latter

assumes that the rich dynamical behavior near the glass transition is a consequence of kinetic constraints, while thermodynamics and static correlations play a very limited or no role at all [40,41,46].

Among the theories that support an underlying thermodynamic transition at a finite temperature we can find the Adam-Gibbs theory [47], the Goldstein energy landscape scenario [48], and the Random First Order Transition (RFOT) theory [49–51]. On the other hand, regarding the theories that advocate for kinetic constraints as the cause of the dramatic slowdown in kinetics during the glass transition, we can highlight: the Mode Coupling Theory (MCT) [40,52], Frustration-Limited Domains theory [10,53,54] and Dynamical Facilitation Theory [55–57]. In the following lines, we provide a brief description of some of these theories.

1.6.1 Adam-Gibbs Theory

Adam and Gibbs (1965) developed a theoretical framework in which the relaxation times in deeply supercooled liquids are driven by entropy considerations [47]. In this theory, they suggest that the relaxation of the glass towards equilibrium takes place via the rearrangement over large groups of correlated particles, the so-called Cooperative Rearranging Regions (CRR), which evolve independently of each other and their surroundings. The configurations that each CRR can adopt are significantly limited, since all its constituents are strongly dependent. One of the key ideas of the Adam-Gibbs model is the assumption that the number of configurations that a single CRR can adopt is constant regardless of the size of the CRR and the temperature [10].

1.6.2 Goldstein landscape scenario

Goldstein formulation of the energy landscape scenario (1969) [48] put the emphasis on the evolution of the system in the phase space, i.e., the space of all the configurational degrees of freedom. Over this space it is defined the total potential energy of the system, and the surface of this function is often called the potential energy landscape. In this scenario, each configuration is represented by a point in the phase space, and the dynamics of the system are described by the motion of this point over the potential energy landscape. In the Goldstein scenario, local minima correspond to locally stable

configurations, where the absolute minimum is given by the ground state, that is, the crystal. The remaining local minima above the crystalline phase correspond to defect crystals, polycrystals and particles arrangements that lack long-range order, i.e., the amorphous or glassy states. The latter is expected to have a potential energy that is extensively larger than the crystalline one.

In his studies, Goldstein suggested that as molecules in the liquid pack more closely with decreasing temperature there should be a point where free diffusion, characteristic of simple liquids and dense gases, can no longer occur because the molecules begin to “jam up” and energy fluctuations are needed to free them. That is, at low enough temperatures a system explores the phase space mainly by activated jumps between different energy minima, separated by potential energy barriers that increase when the temperature decreases or the number of particles to rearrange is higher. It is important to note that Goldstein stresses the importance to give this rearrangement regions a local nature.

However, when the temperature is increased, the thermal energy rises and becomes comparable or even higher than the typical potential energy barriers. In this regime, the liquid becomes very fluid and local rearrangements are no longer ruled by thermal activation, breaking down Goldstein’s scenario. This breakdown marks a conceptually useful border between two different regimes: a low-T activated and viscous regime, *versus* a high-T non-activated and fluid regime.

1.6.3 Random First Order Transition Theory (RFOT)

The Random First Order Transition theory (RFOT) or mosaic theory was formulated by Kirkpatrick, Thirumalai and Wolynes in the late 80’s [49–51] and it depicts the glass as a mosaic of glass droplets or “glassites” of linear size ξ , the length of which is fixed by a competition between the surface tension cost and the configurational entropy gain.

The mean-field version of RFOT approach predicts the presence of a dynamical transition at a non-zero temperature, T_d , below which the configuration space of the glass former splits into a collection of an exponential number of possible metastable states. Within mean field models, below T_d the system will remain trapped inside a metastable state, since the potential barriers separating states diverge. However, for finite systems the

dynamical transition, T_d , becomes a cross-over point: relaxation time and correlation functions become large, but finite, leading to the phenomenological glass transition.

In RFOT, the system explores the whole collection of possible states with lower free energy via activation events as the temperature is decreased. Upon further lowering the temperature, the states with the lowest free energy are reached at a temperature T_k where most RFOT models predict an equilibrium phase transition with a real divergence of the relaxation time. Therefore, the mosaic picture presents two characteristic temperatures T_d and T_k , that separate three different regimes: at high temperature, $T > T_d$, the landscape is simple and presents a single minimum, the high temperature liquid state. This is followed by an intermediate temperature regime, $T_k < T < T_d$ where an exponentially large number of minima appear, and the system enters the so-called glass phase. And finally, a low temperature regime, $T < T_k$ where the configurational entropy vanishes and the system, if equilibrated, enters an ideal glass state.

It is important to note that what actually drives the rearrangement in the mosaic theory are thermal fluctuations. That is, once the region has been pushed out from its original state by thermal fluctuations, the probability that the droplet will remain in the original state or change to another state will depend on entropic considerations of the number of the available states.

Beyond the differences the RFOT presents with the Adam-Gibbs theory, it recovers the most important result from the latter: a characteristic length scale that increases with decreasing configurational entropy.

1.6.4 Mode Coupling Theory (MCT)

The Mode Coupling Theory [40,52] makes use of the dynamical correlation function of density fluctuations to explain the behavior of the supercooled liquid approaching the glass transition.

The key idea we need to take from this model is that MCT developed a set of self-consistent equations in which introducing only static observables like the structure factor, $S(k)$, which can be obtained directly from scattering experiments, we end up with a set of dynamical equations. This is possible thanks to the implementation of non-linear

interactions, which gives rise to a direct dependence between the static structure and the dynamics.

An interesting result of the MCT is that this model is able to reproduce the two-step relaxation near the glass transition of the dynamical correlation function, meaning there are “fast” and “slow” dynamics in the supercooled liquid. In this scenario, a plateau emerges and its length scale increases when decreasing temperature (as shown in Figure 1.4 for real systems). However, due to the mean field character of this model (which forbids to restore ergodicity), MCT predicts that the length of the plateau and, therefore, of the relaxation time, will diverge at a finite temperature, T_c . Nevertheless, for temperatures above T_c the predictions of the MCT are in good agreement with what is observed in supercooled liquids and the theory is widely supported.

1.6.5 Frustration-limited-domains (FLD) theory

The frustration-limited-domains theory [10,46,53] is based in two concepts: locally preferred structure (LPS) and geometric frustration. Similar to the Adam-Gibbs or mosaic theories, the LPS can be defined as an arrangement of molecules that minimize some local free energy. However, in this case, the origin of the cooperative regions is not of thermodynamic origin but due to geometric frustration. It is this frustration, which arises from the incompatibility of the LPS regions to attain long-range order, what controls much of the physics of the system and, in particular, the characteristic slowing down of the glass-forming liquids.

1.6.6 Dynamical Facilitation Theory (DFT)

The dynamical facilitation theory [55–57] defends that all the physical aspects in glass-forming liquids can be understood purely at the dynamical level. The main idea of this theory is that the mobility of the supercooled liquid is localized in very specific regions. At low temperatures, all the system is arrested and only few particles will be mobile. These particles, which can be interpreted as mobility defects, will be the ones that will prompt, or facilitate, mobility in its neighboring regions. This is known as dynamic (or kinetic) facilitation.

In this context, the slowdown of the dynamics is a consequence of the effective dynamical constraints among the particles when the temperature is lowered.

Despite the proliferation of many different theories and views, none of them is able to describe fully the physics behind the glass transition, which is why different theories are often combined. For instance, RFOT is often combined with MCT to describe the high temperature range and with dynamic facilitation theory to help explain the growth of the liquid phase in stable glasses [22].

References

- [1] D. Turnbull, *Under What Conditions Can A Glass Be Formed?*, *Contemp Phys* **10**, 473 (1969).
- [2] C. A. Angell, *Structural Instability and Relaxation in Liquid and Glassy Phases near the Fragile Liquid Limit*, *J Non Cryst Solids* **102**, 205 (1988).
- [3] C. A. Angell, K. L. Ngai, G. B. McKenna, P. F. McMillan, and S. W. Martin, *Relaxation in Glassforming Liquids and Amorphous Solids*, *J Appl Phys* **88**, 3113 (2000).
- [4] V. Lubchenko and P. G. Wolynes, *Theory of Structural Glasses and Supercooled Liquids*, *Annual Review of Physical Chemistry*.
- [5] M. D. Ediger, C. A. Angell, and S. R. Nagel, *Supercooled Liquids and Glasses*, *J Phys Chem* **100**, 13200 (1996).
- [6] P. G. Debenedetti and F. H. Stillinger, *Supercooled Liquids and the Glass Transition*, *Nature* **410**, 259 (2001).
- [7] R. Brüning and K. Samwer, *Glass Transition on Long Time Scales*, *Phys Rev B* **46**, 11318 (1992).
- [8] C. T. et al. Moynihan, *The Glass Transition and the Nature of the Glassy State*, Vol. 279 (1976).
- [9] S. R. Nagel, *Susceptibility Studies of Supercooled Liquids and Glasses*, in *Phase Transitions and Relaxation in Systems with Competing Energy Scales*, edited by T. Riste and D. Sherrington (Springer Netherlands, Dordrecht, 1993), pp. 259–283.
- [10] A. Cavagna, *Supercooled Liquids for Pedestrians*, *Phys Rep* **476**, 51 (2009).
- [11] I. Tah, A. Mutneja, and S. Karmakar, *Understanding Slow and Heterogeneous Dynamics in Model Supercooled Glass-Forming Liquids*, *ACS Omega* **6**, 7229 (2021).
- [12] C. A. Angell, *Formation of Glasses from Liquids and Biopolymers*, *Science* (1979) **267**, 1924 (1995).
- [13] C. M. Roland, *Characteristic Relaxation Times and Their Invariance to Thermodynamic Conditions*, *Soft Matter* **4**, 2316 (2008).
- [14] Q. Gao and Z. Jian, *Critical Cooling Rate Prediction by the Reduced Glass Temperature and Fragility Index*, *Physica Status Solidi (b)* **256**, 1900012 (2019).
- [15] W. Kob and H. C. Andersen, *Testing Mode-Coupling Theory for a Supercooled Binary Lennard-Jones Mixture. II. Intermediate Scattering Function and Dynamic Susceptibility*, *Phys Rev E* **52**, 4134 (1995).
- [16] R. H. A. Kohlrausch, *Theorie Des Elektrischen Rückstandes in Der Leidener Flasche*, *Ann Phys* **167**, 179 (1874).
- [17] G. Williams and D. C. Watts, *Non-Symmetrical Dielectric Relaxation Behaviour Arising from a Simple Empirical Decay Function*, *Transactions of the Faraday Society* **66**, 80 (1970).
- [18] E. Vidal Russell and N. E. Israeloff, *Direct Observation of Molecular Cooperativity near the Glass Transition*, *Nature* **408**, 695 (2000).
- [19] M. D. Ediger, *Spatially Heterogeneous Dynamics in Supercooled Liquids*, *Annu Rev Phys Chem* **51**, 99 (2000).

-
- [20] L. Berthier, *Trends Dynamic Heterogeneity in Amorphous Materials*, Physics (College Park Md) **4**, 42 (2011).
- [21] D. N. Perera and P. Harrowell, *Consequences of Kinetic Inhomogeneities in Glasses*, Phys Rev E **54**, 1652 (1996).
- [22] P. G. Wolynes, *Spatiotemporal Structures in Aging and Rejuvenating Glasses*, Proc Natl Acad Sci U S A **106**, 1353 (2009).
- [23] U. Tracht, M. Wilhelm, A. Heuer, H. Feng, K. Schmidt-Rohr, and H. W. Spiess, *Length Scale of Dynamic Heterogeneities at the Glass Transition Determined by Multidimensional Nuclear Magnetic Resonance*, Phys Rev Lett **81**, 2727 (1998).
- [24] O. Dauchot, G. Marty, and G. Biroli, *Dynamical Heterogeneity Close to the Jamming Transition in a Sheared Granular Material*, Phys Rev Lett **95**, 265701 (2005).
- [25] A. S. Keys, A. R. Abate, S. C. Glotzer, and D. J. Durian, *Measurement of Growing Dynamical Length Scales and Prediction of the Jamming Transition in a Granular Material*, Nat Phys **3**, 260 (2007).
- [26] L. Berthier, G. Biroli, J.-P. Bouchaud, L. Cipelletti, and W. van Saarloos, *Dynamical Heterogeneities in Glasses, Colloids, and Granular Media*, in (2011).
- [27] T. E. Angelini, E. Hannezo, X. Trepant, M. Marquez, J. J. Fredberg, and D. A. Weitz, *Glass-like Dynamics of Collective Cell Migration*, Proceedings of the National Academy of Sciences **108**, 4714 (2011).
- [28] M. C. Marchetti, J. F. Joanny, S. Ramaswamy, T. B. Liverpool, J. Prost, M. Rao, and R. A. Simha, *Hydrodynamics of Soft Active Matter*, Rev Mod Phys **85**, 1143 (2013).
- [29] B. Olmos, I. Lesanovsky, and J. P. Garrahan, *Facilitated Spin Models of Dissipative Quantum Glasses*, Phys Rev Lett **109**, 20403 (2012).
- [30] Z. Nussinov, P. Johnson, M. J. Graf, and A. v Balatsky, *Mapping between Finite Temperature Classical and Zero Temperature Quantum Systems: Quantum Critical Jamming and Quantum Dynamical Heterogeneities*, Phys Rev B **87**, 184202 (2013).
- [31] A. P. Sokolov, E. Rössler, A. Kisliuk, and D. Quitmann, *Dynamics of Strong and Fragile Glass Formers: Differences and Correlation with Low-Temperature Properties*, Phys Rev Lett **71**, 2062 (1993).
- [32] M. T. Cicerone and M. D. Ediger, *Enhanced Translation of Probe Molecules in Supercooled O-terphenyl: Signature of Spatially Heterogeneous Dynamics?*, J Chem Phys **104**, 7210 (1996).
- [33] Joan Ràfols-Ribé, *Organic Vapour-Deposited Stable Glasses: From Fundamental Thermal Properties to High-Performance Organic Light-Emitting Diodes.*, Universitat Autònoma de Barcelona, 2017.
- [34] Cristian Rodríguez-Tinoco, *Calorimetric Study of Vapour Deposited Glasses: Beyond Conventional Stability and Temperature Limits*, Universitat Autònoma de Barcelona, 2016.
- [35] P. Badrinarayanan, W. Zheng, Q. Li, and S. L. Simon, *The Glass Transition Temperature versus the Fictive Temperature*, J Non Cryst Solids **353**, 2603 (2007).

- [36] C. T. Moynihan, S.-K. Lee, M. Tatsumisago, and T. Minami, *Estimation of Activation Energies for Structural Relaxation and Viscous Flow from DTA and DSC Experiments*, *Thermochim Acta* **280–281**, 153 (1996).
- [37] E. Gruber, *L. G. E. Struik: Physical Aging in Amorphous Polymers and Other Materials*. Elsevier Sci. Publ. Comp., Amsterdam-Oxford-New York 1978. 229 Seiten, 141 Abbildungen, Preis: US \$ 42,50, Holl. Gulden 97,50., *Berichte Der Bunsengesellschaft Für Physikalische Chemie* **82**, 1019 (1978).
- [38] A., Vila-Costa, J. Ràfols-Ribé, M. Gonzalez-Silveira, A. F. Lopeandia, Ll. Abad-Muñoz, J. Rodriguez-Viejo, *Nucleation and Growth of the Supercooled Liquid Phase Control Glass Transition in Bulk Ultrastable Glasses*, *Phys Rev Lett* **124**, 076002 (2020).
- [39] M. Lüttich, V. M. Giordano, S. le Floch, E. Pineda, F. Zontone, Y. Luo, K. Samwer, and B. Ruta, *Anti-Aging in Ultrastable Metallic Glasses*, *Phys Rev Lett* **120**, 135504 (2018).
- [40] L. M. C. Janssen, *Mode-Coupling Theory of the Glass Transition: A Primer*, *Front Phys* **6**, 1 (2018).
- [41] G. Biroli and J. P. Garrahan, *Perspective: The Glass Transition*, *J Chem Phys* **138**, 12A301 (2013).
- [42] T. Hecksher and J. C. Dyre, *A Review of Experiments Testing the Shoving Model*, *J Non Cryst Solids* **407**, 14 (2015).
- [43] J. F. Stanzione, K. E. Strawhecker, and R. P. Wool, *Observing the Twinkling Fractal Nature of the Glass Transition*, *J Non Cryst Solids* **357**, 311 (2011).
- [44] J. C. Mauro, Y. Yue, A. J. Ellison, P. K. Gupta, and D. C. Allan, *Viscosity of Glass-Forming Liquids*, *Proceedings of the National Academy of Sciences* **106**, 19780 (2009).
- [45] V. Lubchenko, *Theory of the Structural Glass Transition: A Pedagogical Review*, *Adv Phys* **64**, 283 (2015).
- [46] G. Tarjus, S. A. Kivelson, Z. Nussinov, and P. Viot, *The Frustration-Based Approach of Supercooled Liquids and the Glass Transition: A Review and Critical Assessment*, *Journal of Physics: Condensed Matter* **17**, R1143 (2005).
- [47] G. Adam and J. H. Gibbs, *On the Temperature Dependence of Cooperative Relaxation Properties in Glass-Forming Liquids*, *J Chem Phys* **43**, 139 (1965).
- [48] M. Goldstein, *Viscous Liquids and the Glass Transition: A Potential Energy Barrier Picture*, *J Chem Phys* **51**, 3728 (1969).
- [49] T. R. Kirkpatrick and D. Thirumalai, *Dynamics of the Structural Glass Transition and the P-Spin--Interaction Spin-Glass Model*, *Phys Rev Lett* **58**, 2091 (1987).
- [50] T. R. Kirkpatrick and P. G. Wolynes, *Connections between Some Kinetic and Equilibrium Theories of the Glass Transition*, *Phys Rev A (Coll Park)* **35**, 3072 (1987).
- [51] T. R. Kirkpatrick and P. G. Wolynes, *Stable and Metastable States in Mean-Field Potts and Structural Glasses*, *Phys Rev B* **36**, 8552 (1987).
- [52] U. Bengtzelius, W. Gotze, and A. Sjolander, *Dynamics of Supercooled Liquids and the Glass Transition*, *Journal of Physics C: Solid State Physics* **17**, 5915 (1984).

- [53] D. Kivelson, S. A. Kivelson, X. Zhao, Z. Nussinov, and G. Tarjus, *A Thermodynamic Theory of Supercooled Liquids*, *Physica A: Statistical Mechanics and Its Applications* **219**, 27 (1995).
- [54] G. Tarjus and D. Kivelson, *Breakdown of the Stokes–Einstein Relation in Supercooled Liquids*, *J Chem Phys* **103**, 3071 (1995).
- [55] J. P. Garrahan and D. Chandler, *Geometrical Explanation and Scaling of Dynamical Heterogeneities in Glass Forming Systems*, *Phys Rev Lett* **89**, 35704 (2002).
- [56] L. Berthier and J. P. Garrahan, *Nontopographic Description of Inherent Structure Dynamics in Glassformers*, *J Chem Phys* **119**, 4367 (2003).
- [57] J. P. Garrahan and D. Chandler, *Coarse-Grained Microscopic Model of Glass Formers*, *Proceedings of the National Academy of Sciences* **100**, 9710 (2003).

Chapter 2

Vapor-deposited glasses

The most common way of obtaining a glass is by cooling a liquid at a pace fast enough to avoid crystallization. However, getting access to low energy states by this route is impracticably slow [1,2]. As discussed in Chapter 1, when a supercooled liquid is cooled down, the relaxation time increases dramatically as the temperature is reduced, until a certain temperature, where the mobility becomes too slow to allow the molecules to reach equilibrium and the glass is formed [1,3]. Because glasses are thermodynamically unstable, lower energies in the landscape are eventually achieved when the glass is kept at a certain temperature (conventional aging). However, this process is so slow that the time needed to reach states deep in the landscape is unattainable in laboratory timescales.

This scenario changed in 2007, when it was discovered that glasses grown by physical vapor deposition (PVD) under specific conditions could show remarkable properties compared with liquid cooled ones. Swallen *et al.* [4] reported that via vapor deposition it is possible to bypass the kinetic restrictions caused by the slowdown during the cooling process, achieving glasses with outstanding thermodynamic and kinetic stability as well as atypical high densities. In their work, they analyzed PVD glasses of the organic molecules 1,3-bis-(1-naphthyl)-5-(2-naphthyl) benzene (TNB) and indomethacin (IMC) and realized that vapor deposited samples grown in the vicinity of $0.85T_g$ at low deposition rates ($\sim 5\text{nm/s}$) present much higher onset devitrification temperatures (enhanced kinetic stability) and lower enthalpy and fictive temperature values (i.e. enhanced thermodynamic stability) when compared with glasses obtained by cooling from the liquid phase. Thus, making it possible to access glasses that are much deeper in the potential energy landscape.

Even though most of the work on highly stable glasses has involved organic molecules, by means of vapor deposition, one can prepare glasses with high stabilities for a wide variety of materials [5]. After the first measurements in 2007 [4] with TNB and IMC, more than 45 different organic molecules [5], as well as some polymers [6] and metallic glasses [7] have shown their ability to form highly stable glasses if grown under the adequate conditions.

2.1 Formation mechanism

The fact that physical vapor deposition yields glasses with enhanced stabilities was rather remarkable given that, before 2007, the literature on vapor-deposited glasses mainly reported glasses characterized for exhibiting low density and low stability [8–10]. It was thought that the molecules, as soon as they arrived on the cold substrate, would be arrested due to the extremely fast cooling rates on the surface, trapping the system in a less stable state than the liquid cooled sample. It has been seen, however, that this description does not match with reality and that in fact, depending on the deposition conditions, molecules do have enough energy and time to explore the different configurations achieving glasses with much higher densities and stabilities [4,11–13]. The formation of these high-density glasses can be rationalized by a surface equilibration mechanism: if the mobility at the glass surface is high enough, the molecules will be able to efficiently sample the energy landscape and attain the optimal configuration according to the substrate temperature before being buried by the upcoming ones, even if the temperature is below T_g [5]. For low deposition rates, the molecules at the surface will be able to get closer to equilibrium configurational states and a glass with higher stability will be obtained [11,14]. In contrast, if the deposition rate is fast, molecules will be locked inside the bulk of the film after sampling just a small fraction of the energy landscape, obtaining in this way a less stable glass.

Initially, the equilibration mechanism was thought to be related to the enhanced diffusion that molecules exhibit at the surface of a material compared with its bulk counterpart. In general, measured surface diffusion coefficients on organic glasses range from 10^{-11} to 10^{-16} m²/s at T_g , which is 4 to 8 orders of magnitude larger than the bulk [5,15–17]. This enhancement of surface diffusion with respect to the bulk [18] allows to overcome the

kinetic restrictions to molecular rearrangement due to the slow bulk dynamics, reaching in this way stable packing configurations in timescales which are comparable with the residence time of the molecules at the surface. In contrast with bulk diffusion, which follows a super-Arrhenius dependence with temperature, surface diffusion typically follows an Arrhenius type behavior [5,15].

Although the enhanced surface diffusion seems to correlate well with the obtention of some organic glasses with high stabilities, recent studies suggest that surface equilibration cannot be explained by surface diffusion alone. Experimental studies involving different organic molecules have reported the possibility to obtain glasses with similar stability states regardless of the fact that, some of these molecules present enhanced surface diffusion, and others do not [19], concluding that this parameter is not a requisite for the formation of highly stable glasses. This uncorrelation between equilibration and surface diffusion has also been observed with molecular dynamics simulations [20,21].

A possible explanation for this uncorrelation is that stable glass formation, which relies on the improvement of local packing arrangements, may involve other processes that are not related to translational molecular movements, but to a local surface relaxation mechanism [22,23]. Some authors [24] have associated the stable glass formation with the secondary Johari-Goldstein (JG) relaxation found in many glass formers. In this approach, the JG-beta relaxation has been linked to surface mobility in an analogous way as structural relaxation is linked to the bulk dynamics. Alternatively, other works [25,26] have reported the presence of a two-step enthalpy recovery with two different enthalpy plateaus in polymer thin films and spheres which have been aged at different temperatures for certain amounts of time. This double plateau can be associated to two different equilibration time scales: a faster one with an activation energy significantly smaller than the structural relaxation at T_g (related with the surface dynamics) and a slower one, comparable with the bulk structural relaxation process.

Even when there is a significant number of hypotheses which try to explain the nature of this phenomenon, the surface equilibration mechanism is yet not completely agreed upon. However, there seems to be consensus on the fact that these fast dynamics are not exclusively superficial but propagate into the bulk. In general, most authors propose that this enhanced mobility of the surface penetrates several times the cooperative length-scale of the material [19,27].

Regardless of the true nature of the equilibration mechanism, the enhanced surface mobility allows us to surpass the slow dynamics near T_g and access low regions of the potential energy landscape, unreachable by conventional aging in laboratory time scales. It is estimated that aging an ordinary glass, i.e. a glass obtained from the melt, to a similar position in the landscape would require thousands or millions of years [11]. Because of their high stability, vapor-deposited glasses prepared at deposition temperatures around $0.85T_g$ and low deposition rates are referred to as highly stable or ultrastable glasses (UG).

2.2 Properties of highly stable glasses

Glasses prepared by physical vapor deposition present remarkable properties. Among them, the most prominent one is the enhancement of their thermodynamic and kinetic stability. Since the first reports of stable glass formation by PVD [4], many other systems (mostly organic) have reported higher kinetic stabilities and lower enthalpies via many different techniques, such as calorimetry [11,28–30], ellipsometry [31,32], dielectric relaxation spectroscopy [33,34] or neutron reflectivity [4], among many others.

In calorimetry measurements, the kinetic stability is typically measured by the shift of the onset of devitrification (T_{on}), that is, the temperature at which the sample starts to transform into the supercooled liquid on heating. As we discussed in Chapter 1, glasses with high kinetic stability present, for the same heating rate, high values of the onset temperature. For highly stable glasses shifts in T_{on} of around 5% relative to T_g are typically reported [5].

Another way to quantify the kinetic stability is by comparing the time needed to transform the material into the supercooled liquid phase during an isotherm at a temperature above T_f (t_{trans}) with the alpha relaxation time (τ_α). It has been seen that highly stable glasses require up to 10^5 times the structural relaxation time of the supercooled liquid to fully transform [35].

On the other hand, the thermodynamic stability, which is measured by the decrease of a state variable (enthalpy, volume) with respect to the liquid-cooled glass, is generally described by the fictive temperature (T_f), i.e. the lower the fictive temperature, the higher

the thermal stability. In this case, T_f reductions of around 6-13% are typically reached in highly stable glasses [5].

Figure 2.1 shows T_{on} and T_f as a function of the substrate temperature for two organic semiconductor molecules grown at deposition rates between 0.1nm/s and 1nm/s. These systems present a maximum of stability for deposition temperatures between $0.8-0.9T_g$ as it can be observed by the maximum values of the onset temperature and minimum values of the fictive temperature. This behavior can be generalized to most glass formers, which report the highest stabilities when grown at these specific conditions.

As it can be observed in Figure 2.1, at temperatures just below T_g , the limiting fictive temperature matches the deposition temperature. In this temperature range, the deposition molecules are in thermodynamic equilibrium with the liquid and the glasses present macroscopic properties that resemble those expected for the supercooled liquid [31]. However, at lower temperatures (generally below $0.8T_g$), this trend falls apart and the glass does not follow anymore the extrapolation line of the supercooled liquid, falling out of this thermodynamic equilibrium.

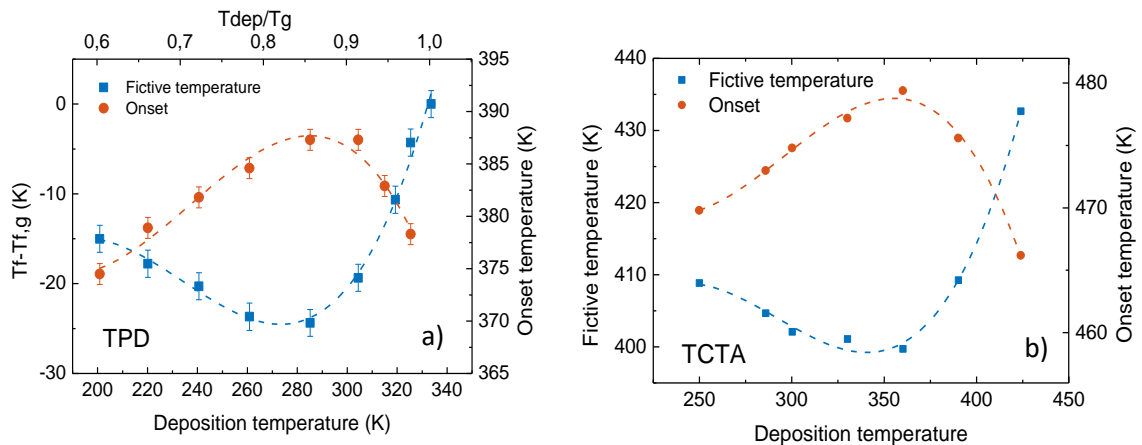


Figure 2. 1. Limiting fictive temperature (left-axis) and onset devitrification temperature (right-axis) for TPD glasses (a) and TCTA glasses (b) as a function of deposition temperature. The uncertainty in T_f corresponds to the square sum of statistical uncertainty and instrumental uncertainty. Figure adapted from [36].

Another important characteristic of many vapor-deposited glasses is the existence of molecular anisotropy. In contrast with liquid cooled glasses, which present mainly isotropic packing [37], vapor-deposited glasses generally exhibit certain molecular

arrangements that depend predominantly on the deposition conditions (deposition temperature and deposition rate) and on the molecules' shape [38,39]. The most accepted view regarding the origin of anisotropy in vapor-deposited glasses can be understood combining the surface equilibration mechanism and the existence, in equilibrium, of preferred anisotropic molecular arrangements at the glass surface [12,38]. Recent studies [39] have reported that while the bulk of the liquid is completely isotropic, the surface molecular layer presents a range of specific patterns (see Figure 2.2a). During deposition, molecules near the surface strive to equilibrate towards the packing preferred at the equilibrium interface. It has been seen that for low deposition temperatures, only the top layer equilibrates, obtaining glasses with molecules predominately laying parallel to the substrate. At higher temperatures, however, the top two layers manage to equilibrate and further deposition leads to glasses in which vertical orientation is trapped [12,40]. As a result, modifying the deposition conditions it is possible to tailor preferred molecular orientations on VD glasses (see Figure 2.2b).

It is important to remark that even though most vapor-deposited glasses show some degree of anisotropy, no correlation has been found between anisotropy and glass stability.

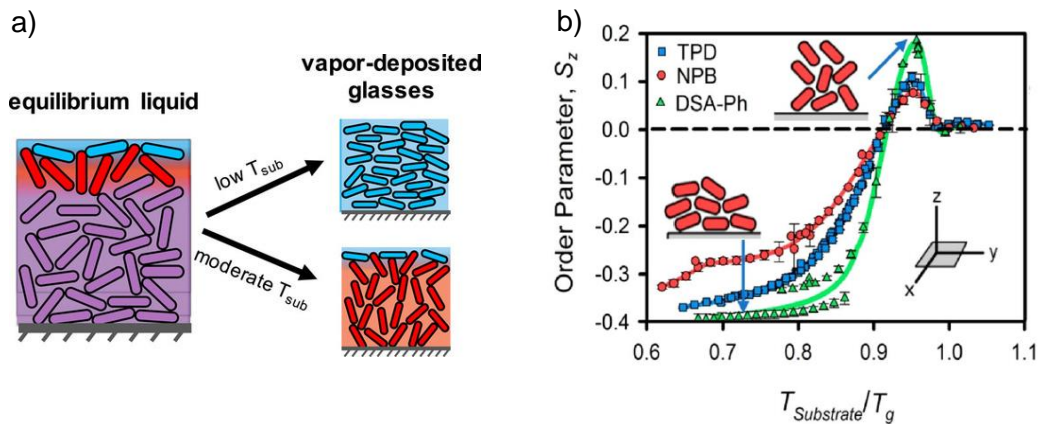


Figure 2. 2. (a) Schematic representation of the anisotropic molecular packing in vapor-deposited glasses as a function of depth for different deposition conditions. (b) Order parameter, S_z , as a function of deposition temperature. Here the deposition temperature is normalized by T_g . $S_z < 0$ corresponds to molecules orientated parallel to the substrate with $S_z < -0.5$ referring to a complete horizontal orientation of the molecules. $S_z = 0$ corresponds to isotropic samples while $S_z > 0$ is obtained for molecules which tend to be perpendicular to the substrate. Image reprinted from [5].

Besides the enhancement of thermodynamic and kinetic stability and the presence of anisotropic packing, highly stable vapor-deposited glasses exhibit other remarkable properties when compared to the conventional glass. Some of the most striking ones are:

- Higher densities: density scales with stability [41–44] and ultrastable glasses can be up to 1.5% denser than the conventional glass.
- Enhanced mechanical properties, such as higher mechanical moduli and sound velocities can also be achieved with the proper deposition conditions [43,45,46].
- Suppression of β -relaxation in some molecules such as toluene or n-propanol [47].
- Suppression of the two-level systems at low temperatures [77].
- Heterogeneous transformation mechanism into the supercooled liquid when heated above T_g [29,35,42,48–50].

This last property is one of the main focuses of this thesis and, therefore, it will be studied in further detail in the following sections.

2.3 Transformation mechanism in vapor-deposited glasses

One of the most striking characteristics of vapor-deposited glasses is the mechanism by which they transform into the supercooled liquid when heated. In contrast with liquid cooled glasses, that transform into the liquid via a cooperative rearrangement of the molecules which takes place homogeneously in the whole volume of the sample [51], vapor-deposited stable glasses transform via a heterogeneous process that resembles the melting of a crystal [52–54].

2.3.1 Front propagation mechanism

In highly stable glasses, the increased density and tight molecular packing are believed to be the cause for the transformation to start at regions of the sample where the mobility is higher. The transformation takes place, as a result, via liquid parallel fronts that start at the free surfaces and mobile interfaces and then propagate into the glass at a constant speed, v_{gr} , with a well-defined interface between the super cooled liquid and the not-yet transformed stable glass [12]. This phenomenon was first identified by Swallen *et al.* in 2008 with the study of the translational motion in protio-/deuterio-tris(naphthylbenzene) (TNB) multilayer films using neutron reflectivity [55]. Since then, a wide variety of techniques have been used to study the dynamics of the propagating fronts in several systems. Experimentally, they have been identified by secondary ion mass spectrometry

(SIMS) [35,48], spectroscopic ellipsometry [42,43] and calorimetric techniques such as AC-calorimetry [56] or fast-scanning nanocalorimetry [29].

All these studies are consistent with transformation rates independent of film thickness but strongly dependent on temperature [42,48,57–60]. Specially, for many organic glasses it was suggested that the velocity of the front follows an empirical relationship with the structural relaxation time of the supercooled liquid, τ_α , and the deposition conditions:

$$v_{gr}(T_{dep}) = C(T_{dep})\tau_\alpha^{-\gamma} \quad (2.1)$$

where C depends on the deposition conditions [58] and is independent of temperature, τ_α is the α -relaxation time of the liquid and T_{dep} refers to the deposition conditions. The value of the γ exponent depends exclusively on the material and for organic glasses has been found to be in the range 0.7-0.95 [34,58]. The relationship expressed in Equation 2.1. was initially found for vapor-deposited glasses of IMC and TNB [35] in a limited temperature range around the glass transition temperature of these materials. However, later studies, have shown that this same expression is valid to describe the velocity of the front for a large range of temperatures, going from T_g up to $T_g + 75K$, in the case of indomethacin glasses [29], and up to $T_g + 25K$ (spanning 8 orders of magnitude in relaxation time) for Toluene glasses [61]. Interestingly, this relationship also holds for glasses with lower stabilities [28,61]. In this case, the transformation rate presents the same temperature dependence but an absolute value that increases for lower stability glasses. The more stable the glass, the slower the front velocity.

This transformation mechanism by propagating fronts has been discussed in detail in several theoretical/computational works. Gutierrez and Garrahan [62] used a three-dimensional East model with soft constraints to recreate the front transformation in stable glasses. Wolyness *et al.* [52,63] described the existence of moving fronts within RFOT by an analogy to a combustion process. More recently, the SWAP methodology [64] has enabled Berthier and coworkers to produce *in-silico* glasses with stabilities that compare well to the highly stable glasses created in the laboratory by vapor deposition [4,30]. These simulated stable glasses, if made thin enough, completely transform into the liquid by moving fronts.

All these observations can be rationalized in terms of the big contrast between the relaxation time (or density) of the actual glass (much denser and with less mobility) and the liquid-like upmost layer of the film together with the concept of kinetic facilitation [65]. The mismatch in relaxation times (and mobilities), prompts the early transformation of the more mobile surface layer into the supercooled liquid which afterwards mediates the transformation inside the bulk via a propagating front with dynamics that are characteristic of the interface between the liquid and the glass [66]. Originally, the dynamics of the growth front were believed to be dominated exclusively by the relaxation dynamics of the fastest component, i.e., the supercooled liquid [67,68]. However, recent works have suggested the necessity of considering extra transition layers to describe the interface between the glass and the more mobile liquid region [5,66,69,70]. Rodriguez-Tinoco *et al.* [66] considered that the front dynamics can be explained by the existence of a progression of transforming intermediate layers with a lifetime given by the average between the transformation time of the bulk and the α -relaxation time of the liquid.

2.3.2 Bulk transformation mechanism

The front transformation mechanism is the dominating mechanism for samples with thicknesses lower than a certain characteristic length: the crossover length. A front that propagates a long distance from the free surface into a stable glass will eventually be disrupted by regions of the sample that have already transformed into the supercooled liquid by a process initiated in the bulk [61,66,71]. We can define, thus, the crossover length, ξ , as the distance that the propagation front travels before the bulk transformation is triggered. A common way to determine the crossover length is measuring the transformation time of a film as a function of its thickness at a constant temperature. The transformation time for films thinner than the crossover length increases linearly with thickness, suggesting that a propagating front with constant velocity controls the transformation in this regime. Films thicker than the crossover length, however, always take the same time to transform into the liquid phase regardless of the thickness, indicating a transformation that is taking place simultaneously in the whole volume [53,66,72].

The value of this crossover length varies widely depending on the molecules under study, the deposition conditions (which determine stability, density and molecular orientation) and the temperature [34,53,61,66], spanning from values of several micrometers (5 μ m for UG methyl-m-toluate [34]) to only a few nanometers in low stability glasses [58,62]. These variations can be understood, in an analogous way to the front transformation, by the interplay between the dynamics of the glass and liquid during the transformation process [66].

The first experimental studies regarding the bulk transformation in ultrastable glasses were reported by Kearns *et al.* [53] and they suggested that samples thicker than the crossover length transform into the supercooled liquid mainly via the emergence of liquid patches inside the glass which grew transforming the sample following an Avrami-like kinetics.

Different theoretical approaches and simulations have also tried to describe the bulk transformation mechanism in ultrastable glasses yielding similar results: the return to equilibrium after a temperature jump above T_f in high stable glasses takes place via the growth of equilibrated regions that expand into the surrounding glass matrix. Douglass and Harrowell, use the facilitated kinetic Ising model to study the relaxation of the glass into the supercooled liquid and the high mobility regions are introduced as inherent dynamic heterogeneities [73]. Gutiérrez and Garrahan use local excitations to initiate the transition in the kinetically constrained model when simulating ultrastable glasses [62]. Lulli *et al.* introduce equilibrated higher temperature regions in a model based on a distinguishable-particle lattice, where they follow the spatial profiles of particle displacement and their interactions to study the relaxation of the glass [74]. Jack and Berthier use a triangular plaquette model based on spin variables considering simple interactions to reproduce the relaxation of glasses equilibrated at different temperatures (i.e. of different stability) [54]. They find that the transition in stable glasses takes place via the nucleation and growth of equilibrated liquid regions. On the contrary, glasses equilibrated at higher temperatures, relax via a relaxation with a broad range of relaxation times, as expected for this type of glasses. Wolyness and coworkers, within Random First Order theory (RFOT) [52], consider the formation of entropy drops in the glass to explain the glass transition. These are small mobile glassy regions that by statistical fluctuations relax fully into the equilibrated liquid and once relaxed, propagate the relaxation into the

less mobile adjacent regions via a kinetic facilitation process [65]. This relaxation would spread as a flame, accelerating the transition of the glass into the liquid. The spreading of this equilibrated liquid into the adjacent regions would be faster than the time required for each of the individual regions to relax, dominating the transition of the whole glass into the liquid. Another recent work by Fullerton and Berthier [75] used the Swap Monte Carlo approach to generate in-silico glasses of ultra-high stability. The transition of this type of glasses into the liquid state takes place via the formation of liquid patches that grow until consuming the static glass matrix, following an Avrami-like kinetics [76]. The basic requirement in all these models for the liquid regions to appear and develop consuming the glass is a big contrast in mobility between these equilibrated liquid regions and the glass matrix, which can be achieved by a jump to higher temperatures (the lower the stability of the glass, the higher the temperature jump required to achieve this mobility contrast).

Regardless of the numerous theoretical and simulation studies, the bulk-like transformation of stable glasses has not been experimentally analyzed in detail yet. Being the only experimental work addressing it the original work by Kearns *et al.* aforementioned [53]. In this sense, the development of this work is committed to contribute to the experimental observation of the bulk transition of highly stable glasses and help to better understand the transformation dynamics of these glasses in the recovery to equilibrium after a temperature jump.

References

- [1] M. D. Ediger, C. A. Angell, and S. R. Nagel, *Supercooled Liquids and Glasses*, J Phys Chem **100**, 13200 (1996).
- [2] D. J. Plazek and J. H. Magill, *Physical Properties of Aromatic Hydrocarbons. I. Viscous and Viscoelastic Behavior of 1:3:5-Tri- α -Naphthyl Benzene*, J Chem Phys **45**, 3038 (1966).
- [3] C. A. Angell, K. L. Ngai, G. B. McKenna, P. F. McMillan, and S. W. Martin, *Relaxation in Glassforming Liquids and Amorphous Solids*, J Appl Phys **88**, 3113 (2000).
- [4] S. F. Swallen, K. L. Kearns, M. K. Mapes, Y. S. Kim, R. J. McMahan, M. D. Ediger, T. Wu, L. Yu, and S. Satija, *Organic Glasses with Exceptional Thermodynamic and Kinetic Stability*, Science (1979) **315**, 353 (2007).
- [5] C. Rodriguez-Tinoco, M. Gonzalez-Silveira, M. A. Ramos, and J. Rodriguez-Viejo, *Ultrastable Glasses: New Perspectives for an Old Problem*, La Rivista Del Nuovo Cimento **45**, 325 (2022).
- [6] Y. Guo, A. Morozov, D. Schneider, J. W. Chung, C. Zhang, M. Waldmann, N. Yao, G. Fytas, C. B. Arnold, and R. D. Priestley, *Ultrastable Nanostructured Polymer Glasses*, Nat Mater **11**, 337 (2012).
- [7] D. P. B. Aji, A. Hirata, F. Zhu, L. Pan, K. M. Reddy, S. Song, Y. Liu, T. Fujita, S. Kohara, and M. Chen, *Ultrastrong and Ultrastable Metallic Glass*, 1 (2013).
- [8] H. Hikawa, M. Oguni, and H. Suga, *Construction of an Adiabatic Calorimeter for a Vapor-Deposited Sample and Thermal Characterization of Amorphous Butyronitrile*, J Non Cryst Solids **101**, 90 (1988).
- [9] O. Haida, H. Suga, and S. Seki, *New Finding of 3 Kinds of Glassy State for Cyclohexene as a Single Compound*, Chem. Lett. **2**, 79 (1973).
- [10] K. Takeda, O. Yamamuro, M. Oguni, and H. Suga, *Calorimetric Study on Structural Relaxation of 1-Pentene in Vapor-Deposited and Liquid-Quenched Glassy States*, J Phys Chem **99**, 1602 (1995).
- [11] K. L. Kearns, S. F. Swallen, M. D. Ediger, T. Wu, Y. Sun, and L. Yu, *Hiking down the Energy Landscape: Progress Toward the Kauzmann Temperature via Vapor Deposition*, J Phys Chem B **112**, 4934 (2008).
- [12] M. D. Ediger, *Perspective: Highly Stable Vapor-Deposited Glasses*, Journal of Chemical Physics **147**, (2017).
- [13] P. Luo et al., *Ultrastable Metallic Glasses Formed on Cold Substrates*, Nat Commun **9**, 1389 (2018).
- [14] Y. Z. Chua, M. Ahrenberg, M. Tyllinski, M. D. Ediger, and C. Schick, *How Much Time Is Needed to Form a Kinetically Stable Glass? AC Calorimetric Study of Vapor-Deposited Glasses of Ethylcyclohexane*, J Chem Phys **142**, 054506 (2015).
- [15] Y. Chen, M. Zhu, A. Laventure, O. Lebel, M. D. Ediger, and L. Yu, *Influence of Hydrogen Bonding on the Surface Diffusion of Molecular Glasses: Comparison of Three Triazines*, J Phys Chem B **121**, 7221 (2017).

- [16] Y. Zhang, R. Potter, W. Zhang, and Z. Fakhraai, *Using Tobacco Mosaic Virus to Probe Enhanced Surface Diffusion of Molecular Glasses*, *Soft Matter* **12**, 9115 (2016).
- [17] L. Zhu, C. W. Brian, S. F. Swallen, P. T. Straus, M. D. Ediger, and L. Yu, *Surface Self-Diffusion of an Organic Glass*, *Phys Rev Lett* **106**, 256103 (2011).
- [18] Y. Chen, Z. Chen, M. Tylinski, M. D. Ediger, and L. Yu, *Effect of Molecular Size and Hydrogen Bonding on Three Surface-Facilitated Processes in Molecular Glasses: Surface Diffusion, Surface Crystal Growth, and Formation of Stable Glasses by Vapor Deposition*, *J Chem Phys* **150**, 024502 (2019).
- [19] S. Samanta, G. Huang, G. Gao, Y. Zhang, A. Zhang, S. Wolf, C. N. Woods, Y. Jin, P. J. Walsh, and Z. Fakhraai, *Exploring the Importance of Surface Diffusion in Stability of Vapor-Deposited Organic Glasses*, *J Phys Chem B* **123**, 4108 (2019).
- [20] L. Berthier, P. Charbonneau, E. Flenner, and F. Zamponi, *Origin of Ultrastability in Vapor-Deposited Glasses*, *Phys Rev Lett* **119**, 188002 (2017).
- [21] N. Kuon, E. Flenner, and G. Szamel, *Comparison of Single Particle Dynamics at the Center and on the Surface of Equilibrium Glassy Films*, *J Chem Phys* **149**, 074501 (2018).
- [22] Y. Chai, T. Salez, J. D. McGraw, M. Benzaquen, K. Dalnoki-Veress, E. Raphaël, and J. A. Forrest, *A Direct Quantitative Measure of Surface Mobility in a Glassy Polymer*, *Science* (1979) **343**, 994 (2014).
- [23] Z. Fakhraai and J. A. Forrest, *Measuring the Surface Dynamics of Glassy Polymers*, *Science* (1979) **319**, 600 (2008).
- [24] K. L. Ngai, L.-M. Wang, and H.-B. Yu, *Relating Ultrastable Glass Formation to Enhanced Surface Diffusion via the Johari–Goldstein β -Relaxation in Molecular Glasses*, *J Phys Chem Lett* **8**, 2739 (2017).
- [25] D. Cangialosi, V. M. Boucher, A. Alegría, and J. Colmenero, *Direct Evidence of Two Equilibration Mechanisms in Glassy Polymers*, *Phys Rev Lett* **111**, 95701 (2013).
- [26] N. G. Perez-De Eulate and D. Cangialosi, *The Very Long-Term Physical Aging of Glassy Polymers*, *Physical Chemistry Chemical Physics* **20**, 12356 (2018).
- [27] J. D. Stevenson and P. G. Wolynes, *On the Surface of Glasses*, *J Chem Phys* **129**, 234514 (2008).
- [28] C. Rodríguez-Tinoco, M. Gonzalez-Silveira, J. Ràfols-Ribé, G. Garcia, and J. Rodríguez-Viejo, *Highly Stable Glasses of Celecoxib: Influence on Thermo-Kinetic Properties, Microstructure and Response towards Crystal Growth*, *J Non Cryst Solids* **407**, 256 (2015).
- [29] C. Rodríguez-Tinoco, M. Gonzalez-Silveira, J. Ràfols-Ribé, A. F. Lopeandía, M. T. Clavaguera-Mora, and J. Rodríguez-Viejo, *Evaluation of Growth Front Velocity in Ultrastable Glasses of Indomethacin over a Wide Temperature Interval*, *J Phys Chem B* **118**, 10795 (2014).
- [30] E. Leon-Gutierrez, A. Sepúlveda, G. Garcia, M. T. Clavaguera-Mora, and J. Rodríguez-Viejo, *Stability of Thin Film Glasses of Toluene and Ethylbenzene Formed by Vapor Deposition: An in Situ Nanocalorimetric Study*, *Physical Chemistry Chemical Physics* **12**, 14693 (2010).
- [31] S. S. Dalal, Z. Fakhraai, and M. D. Ediger, *High-Throughput Ellipsometric Characterization of Vapor-Deposited Indomethacin Glasses*, *J Phys Chem B* **117**, 15415 (2013).

- [32] D. M. Walters, R. Richert, and M. D. Ediger, *Thermal Stability of Vapor-Deposited Stable Glasses of an Organic Semiconductor*, J Chem Phys **142**, 134504 (2015).
- [33] Z. Chen, A. Sepúlveda, M. D. Ediger, and R. Richert, *Dynamics of Glass-Forming Liquids. XVI. Observation of Ultrastable Glass Transformation via Dielectric Spectroscopy*, J Chem Phys **138**, 12A519 (2013).
- [34] A. Sepúlveda, M. Tyllinski, A. Guiseppi-Elie, R. Richert, and M. D. Ediger, *Role of Fragility in the Formation of Highly Stable Organic Glasses*, Phys Rev Lett **113**, 45901 (2014).
- [35] A. Sepúlveda, S. F. Swallen, L. A. Kopff, R. J. McMahon, and M. D. Ediger, *Stable Glasses of Indomethacin and α,α,β -Tris-Naphthylbenzene Transform into Ordinary Supercooled Liquids*, J Chem Phys **137**, 204508 (2012).
- [36] Joan Ràfols-Ribé, *Organic Vapour-Deposited Stable Glasses: From Fundamental Thermal Properties to High-Performance Organic Light-Emitting Diodes.*, Universitat Autònoma de Barcelona, 2017.
- [37] D. Yokoyama, *Molecular Orientation in Small-Molecule Organic Light-Emitting Diodes*, J Mater Chem **21**, 19187 (2011).
- [38] M. D. Ediger, J. de Pablo, and L. Yu, *Anisotropic Vapor-Deposited Glasses: Hybrid Organic Solids*, Acc Chem Res **52**, 407 (2019).
- [39] C. Bishop, J. L. Thelen, E. Gann, M. F. Toney, L. Yu, D. M. DeLongchamp, and M. D. Ediger, *Vapor Deposition of a Nonmesogen Prepares Highly Structured Organic Glasses*, Proceedings of the National Academy of Sciences **116**, 21421 (2019).
- [40] I. Lyubimov, L. Antony, D. M. Walters, D. Rodney, M. D. Ediger, and J. J. de Pablo, *Oriental Anisotropy in Simulated Vapor-Deposited Molecular Glasses*, J Chem Phys **143**, 094502 (2015).
- [41] S. S. Dalal, A. Sepúlveda, G. K. Pribil, Z. Fakhraai, and M. D. Ediger, *Density and Birefringence of a Highly Stable α,α,β -Trisnaphthylbenzene Glass*, J Chem Phys **136**, 204501 (2012).
- [42] D. M. Walters, R. Richert, and M. D. Ediger, *Thermal Stability of Vapor-Deposited Stable Glasses of an Organic Semiconductor*, J Chem Phys **142**, 134504 (2015).
- [43] S. S. Dalal, Z. Fakhraai, and M. D. Ediger, *High-Throughput Ellipsometric Characterization of Vapor-Deposited Indomethacin Glasses*, J Phys Chem B **117**, 15415 (2013).
- [44] S. S. Dalal, D. M. Walters, I. Lyubimov, J. J. de Pablo, and M. D. Ediger, *Tunable Molecular Orientation and Elevated Thermal Stability of Vapor-Deposited Organic Semiconductors*, Proceedings of the National Academy of Sciences **112**, 4227 (2015).
- [45] J. M. Torres, N. Bakken, J. Li, and B. D. Vogt, *Substrate Temperature to Control Moduli and Water Uptake in Thin Films of Vapor Deposited N,N' -Di(1-Naphthyl)- N,N' -Diphenyl-(1,1'-Biphenyl)-4,4'-Diamine (NPD)*, Journal of Physical Chemistry B **119**, 11928 (2015).
- [46] K. L. Kearns, T. Still, G. Fytas, and M. D. Ediger, *High-Modulus Organic Glasses Prepared by Physical Vapor Deposition*, Advanced Materials **22**, 39 (2010).
- [47] H. B. Yu, M. Tyllinski, A. Guiseppi-Elie, M. D. Ediger, and R. Richert, *Suppression of β -Relaxation in Vapor-Deposited Ultrastable Glasses*, Phys Rev Lett **115**, 185501 (2015).

- [48] S. F. Swallen, K. Traynor, R. J. McMahon, M. D. Ediger, and T. E. Mates, *Stable Glass Transformation to Supercooled Liquid via Surface-Initiated Growth Front*, Phys Rev Lett **102**, 65503 (2009).
- [49] C. Rodríguez-Tinoco, M. Gonzalez-Silveira, J. Ràfols-Ribé, A. F. Lopeandía, and J. Rodríguez-Viejo, *Transformation Kinetics of Vapor-Deposited Thin Film Organic Glasses: The Role of Stability and Molecular Packing Anisotropy*, Physical Chemistry Chemical Physics **17**, 31195 (2015).
- [50] D. Bhattacharya and V. Sadtschenko, *Enthalpy and High Temperature Relaxation Kinetics of Stable Vapor-Deposited Glasses of Toluene*, J Chem Phys **141**, 094502 (2014).
- [51] E. Vidal Russell and N. E. Israeloff, *Direct Observation of Molecular Cooperativity near the Glass Transition*, Nature **408**, 695 (2000).
- [52] P. G. Wolynes, *Spatiotemporal Structures in Aging and Rejuvenating Glasses*, Proc Natl Acad Sci U S A **106**, 1353 (2009).
- [53] K. L. Kearns, M. D. Ediger, H. Huth, and C. Schick, *One Micrometer Length Scale Controls Kinetic Stability of Low-Energy Glasses*, J Phys Chem Lett **1**, 388 (2010).
- [54] R. L. Jack and L. Berthier, *The Melting of Stable Glasses Is Governed by Nucleation-and-Growth Dynamics*, Journal of Chemical Physics **144**, (2016).
- [55] S. F. Swallen, K. L. Kearns, S. Satija, K. Traynor, R. J. McMahon, and M. D. Ediger, *Molecular View of the Isothermal Transformation of a Stable Glass to a Liquid*, J Chem Phys **128**, 214514 (2008).
- [56] K. L. Kearns, K. R. Whitaker, M. D. Ediger, H. Huth, and C. Schick, *Observation of Low Heat Capacities for Vapor-Deposited Glasses of Indomethacin as Determined by AC Nanocalorimetry*, J Chem Phys **133**, 014702 (2010).
- [57] M. Tylinski, A. Sepúlveda, D. M. Walters, Y. Z. Chua, C. Schick, and M. D. Ediger, *Vapor-Deposited Glasses of Methyl-m-Toluate: How Uniform Is Stable Glass Transformation?*, J Chem Phys **143**, 244509 (2015).
- [58] C. Rodríguez-Tinoco, M. Gonzalez-Silveira, J. Ràfols-Ribé, A. F. Lopeandía, and J. Rodríguez-Viejo, *Transformation Kinetics of Vapor-Deposited Thin Film Organic Glasses: The Role of Stability and Molecular Packing Anisotropy*, Physical Chemistry Chemical Physics **17**, 31195 (2015).
- [59] A. Sepúlveda, S. F. Swallen, and M. D. Ediger, *Manipulating the Properties of Stable Organic Glasses Using Kinetic Facilitation*, J Chem Phys **138**, 12A517 (2013).
- [60] Z. Chen, A. Sepúlveda, M. D. Ediger, and R. Richert, *Dynamics of Glass-Forming Liquids. XVI. Observation of Ultrastable Glass Transformation via Dielectric Spectroscopy*, J Chem Phys **138**, 12A519 (2013).
- [61] J. Ràfols-Ribé, M. Gonzalez-Silveira, C. Rodríguez-Tinoco, and J. Rodríguez-Viejo, *The Role of Thermodynamic Stability in the Characteristics of the Devitrification Front of Vapour-Deposited Glasses of Toluene*, Phys. Chem. Chem. Phys **19**, 11089 (2017).
- [62] R. Gutiérrez and J. P. Garrahan, *Front Propagation versus Bulk Relaxation in the Annealing Dynamics of a Kinetically Constrained Model of Ultrastable Glasses*, Journal of Statistical Mechanics: Theory and Experiment **2016**, 074005 (2016).

-
- [63] A. Wisitsorasak and P. G. Wolynes, *Dynamical Heterogeneity of the Glassy State*, J Phys Chem B **118**, 7835 (2014).
- [64] A. Ninarello, L. Berthier, and D. Coslovich, *Models and Algorithms for the Next Generation of Glass Transition Studies*, Phys Rev X **7**, 21039 (2017).
- [65] A. S. Keys, J. P. Garrahan, and D. Chandler, *Calorimetric Glass Transition Explained by Hierarchical Dynamic Facilitation*, Proceedings of the National Academy of Sciences **110**, 4482 (2013).
- [66] C. Rodríguez-Tinoco, M. Gonzalez-Silveira, J. Ràfols-Ribé, A. Vila-Costa, J. C. Martinez-Garcia, and J. Rodríguez-Viejo, *Surface-Bulk Interplay in Vapor-Deposited Glasses: Crossover Length and the Origin of Front Transformation*, Phys Rev Lett **123**, (2019).
- [67] P. G. Wolynes, *Some Quantum Weirdness in Physiology*, Proceedings of the National Academy of Sciences **106**, 17247 (2009).
- [68] G. M. Hocky, L. Berthier, and D. R. Reichman, *Equilibrium Ultrastable Glasses Produced by Random Pinning*, J Chem Phys **141**, 224503 (2014).
- [69] J. H. Mangalara, M. D. Marvin, and D. S. Simmons, *Three-Layer Model for the Emergence of Ultrastable Glasses from the Surfaces of Supercooled Liquids*, J Phys Chem B **120**, 4861 (2016).
- [70] W. Ogieglo, K. Tempelman, S. Napolitano, and N. E. Benes, *Evidence of a Transition Layer between the Free Surface and the Bulk*, J Phys Chem Lett **9**, 1195 (2018).
- [71] E. Flenner, L. Berthier, P. Charbonneau, and C. J. Fullerton, *Front-Mediated Melting of Isotropic Ultrastable Glasses*, Phys Rev Lett **123**, 175501 (2019).
- [72] Z. Chen, A. Sepúlveda, M. D. Ediger, and R. Richert, *Dynamics of Glass-Forming Liquids. XVI. Observation of Ultrastable Glass Transformation via Dielectric Spectroscopy*, J Chem Phys **138**, 12A519 (2013).
- [73] I. Douglass and P. Harrowell, *Can a Stable Glass Be Superheated Modelling the Kinetic Stability of Coated Glassy Films*, Journal of Chemical Physics **138**, (2013).
- [74] M. Lulli, C. S. Lee, H. Y. Deng, C. T. Yip, and C. H. Lam, *Spatial Heterogeneities in Structural Temperature Cause Kovacs' Expansion Gap Paradox in Aging of Glasses*, Phys Rev Lett **124**, (2020).
- [75] C. J. Fullerton and L. Berthier, *Density Controls the Kinetic Stability of Ultrastable Glasses*, EPL (Europhysics Letters) **119**, 36003 (2017).
- [76] M. Avrami, *Kinetics of Phase Change. I General Theory*, J Chem Phys **7**, 1103 (1939).
- [77] T. Pérez-Castañeda, C. Rodríguez-Tinoco, J. Rodríguez-Viejo, M. A. Ramos, *Suppression of tunneling two-level systems in ultrastable glasses of indomethacin*, Proceedings of the National Academy of Sciences of the United States of America **111**, 31 (2014).

Chapter 3

Experimental methods

In this chapter, we describe the experimental methods used for the development of this work. We start explaining the basis of physical vapor deposition, which is the technique we use to prepare all the samples in this thesis. We continue by providing the basics of the different characterization techniques employed and finish up with a detailed description of the actual experimental setup used in this work.

3.1 Physical vapor deposition process

Physical vapor deposition (PVD) describes a variety of vacuum deposition methods which can be used to produce thin films and coatings. PVD relies on a physical process that transforms the precursor material (solid or liquid) into a vapor phase, which is transported afterwards through vacuum or a low-pressure environment to the substrate, where it condenses. PVD processes can be used to deposit films of elemental materials, alloys and compound materials as well as some polymeric materials [1–3]. Typically, PVD processes are used to grow films with thicknesses that can range from few nanometers to several microns, even though they can also be used to produce very thick samples, graded composition deposits or freestanding structures [4]. There are different methods to produce the vapor phase, such as thermal evaporation, sputtering deposition, arc vapor deposition, e-beam deposition or pulsed laser deposition. A variation of the later, MAPLE (Matrix Assisted Pulsed Laser Evaporation), has been recently used for the deposition of polymers [5]. In this work, we produce glasses of two organic compounds

with relatively low melting temperature, thus thermal evaporation is the most suitable approach.

Thermal evaporation is a process in which material from a source is thermally vaporized (by heating the material above or near its melting point, in the case of solids) and transported to the substrate with little or no collision with the other molecules in the space separating the source and the substrate. In this sense, a high enough vacuum environment is essential in order to achieve a long mean free path of the deposited molecules. The vacuum environment also provides the ability to highly reduce gaseous contamination in the deposition chamber. Typically, vacuum deposition takes place in vacuum environments with gas pressure lower than 10^{-6} mbar [4].

Thermal evaporation is generally achieved using thermally heated sources such as tungsten wire coils or by a high energy electron beam (e-beam) directly heating the source material. Due to this direct heating, the substrate is usually mounted at a prudential distance from the source to reduce radiant heating.

3.2 Characterization techniques: the basics

One of the most widely used magnitudes to study the glass transition and the properties of glasses is heat capacity. Typically, heat capacity data is obtained by using conventional calorimetry. However, when the samples under study consist of very thin films, the thermal processes will involve small amounts of energy and conventional calorimetry does not offer sufficient resolution. Quasi-adiabatic fast scanning nanocalorimetry, in this sense, has proven to be able to achieve very high resolution [6–9], making it an ideal tool for characterizing small mass samples such as thin films. For the development of this work, conventional differential scanning calorimetry and quasi-adiabatic fast scanning calorimetry have been the mainly used techniques to study the glass transformation mechanism in different organic glasses grown by physical vapor deposition.

In addition to the changes in thermodynamic and kinetic parameters probed with calorimetry, the transformation mechanism of thin films is also studied by means of atomic force microscopy. In this case, we take advantage of the changes in the surface morphology of the film during the glass transition to obtain crucial information regarding the spatial dynamics of the studied system, not accessible by other techniques.

3.2.1 Differential scanning calorimetry (DSC)

When materials experiment a transition between two different states, there is generally a transfer of heat either from the material to its surroundings (exothermic reaction) or from the surroundings to the material (endothermic reaction). Differential Scanning Calorimetry (DSC) is a technique that allows us to monitor this heat exchange in order to infer the dynamics behind the transition, the energy involved in the process and the evolution of the heat capacity of the system, among many others.

Conventional differential scanning calorimetry relies on the monitoring of the heat flux and temperature of two almost identical cells: sample and reference. There are two modalities of this technique: heat-flux and power compensation DSC, but only the latter will be used for this particular work. In this modality, two identical cells, one of them set as the reference and a second one containing the sample, are heated independently and kept at a set temperature. In order to maintain both cells at the same temperature the system is divided in two control loops: the first, corresponds to the temperature control which ensures that both cells, the sample and the reference, follow the same temperature program, and the second, guarantees that if there is a difference in temperature between them (due to an exothermal or endothermic reaction in the sample), the provided power amount will change to compensate this difference.

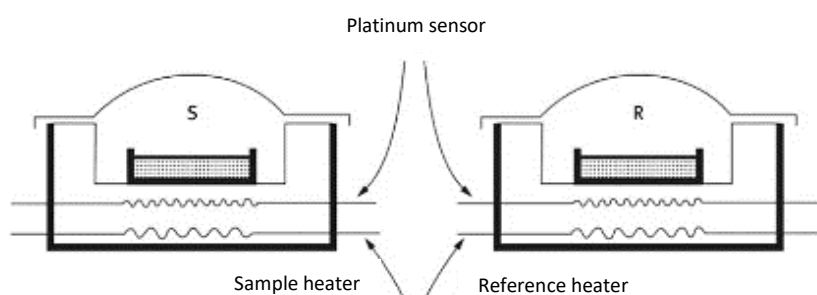


Figure 3. 1. Schematic of the operation principle of a power compensated DSC. In this modality each of the calorimetric cells are heated independently, providing different amounts of power in order to ensure that both cells remain at a set temperature. Figure reprinted from [10].

Before measurements can be performed, the device should be calibrated. This calibration is performed by measuring a reference material which will follow a transformation of known temperature and latent heat. In our case, we used as reference the melting

temperature and latent heat of a known mass of indium. It is also important to notice that the calibration factor depends on the heating rate and, therefore, a new calibration needs to be carried out for each different heating rate used for the experiments. In conventional DSC techniques, the accessible heating rates range, typically, between 0.1 K/min and 150 K/min.

3.2.2 Quasi-adiabatic fast scanning Nanocalorimetry

Conventional calorimetry faces two main limitations. In first place, the heating rates which can be imposed and monitored with this technique are limited across a restricted range. In addition, another important disadvantage for conventional DSC is the resolution of the device, basically due to the large mass of the addenda. The need for samples with masses in the order of, at least, several milligrams is a major limitation for the study of some specific nano-scaled systems, because of the small amounts of energy involved in the reactions.

In that sense, the advances in microfabrication techniques driven by the Si technological industries supposed a big step forward in the development of devices with enhanced mass and energy resolutions, which was marked by the reduction of the heat capacity addenda of their calorimetric cells [11]. Making possible, in this way, the measurement of nanoscale systems and opening the path to the development of a whole new branch of techniques based on microfabricated membrane-based devices.

A powerful technique to measure thermal processes in nano-size systems is quasi-adiabatic fast scanning nanocalorimetry. This technique is characterized by using thin dielectric free-standing membranes (generally made of silicon nitride) that allow the measurement of the small amounts of energy involved in thermal processes of nanoscopic samples (down to a few nanometers in thickness). It is possible, thus, to get access to the transformation dynamics, specific heat (C_p), entropy changes, transition temperatures and transformation enthalpies of nanosized layers, making it the ideal tool for the development of this work.

Allen and co-workers [12] settled down the basis for adiabatic nanocalorimetry, also known as thin-film differential scanning calorimetry (TDSC), in 1995. This technique combined the membrane-based technology with high heating rates, above 10^4 K/s,

achieving extraordinary heat capacity resolutions (better than 1 nJ) in samples of just a few nanograms. Since then, many more efforts were made in order to achieve higher resolutions, either reducing the dimensions of the calorimetric cells, increasing the heating rates or changing the surrounding conditions (pressure, gas...), expanding in this way the range of possible studies and measurements that can be carried out.

In that sense, in 2001, the Group of Thermal Properties of Nanoscale Materials (GTNaM) designed and microfabricated an ultrathin calorimeter based on a thin film dielectric membrane [8,9]. This device was designed using a single metallic thin film element as a heater and thermometer, which greatly reduced the heat capacity addenda per unit area (down to $500 \text{ nJK}^{-1}\text{mm}^{-2}$ at room temperature), making it possible to reach high heating rates (up to 10^6 Ks^{-1}).

3.2.2.1 Device description and microfabrication process

The calorimeters used for the development of this work are shown in Figure 3.2. These devices consist of a $3 \times 6 \text{ mm}^2$ and 180 nm thick silicon nitride free standing membrane held by a silicon frame. On the top side of this membrane, a 100 nm thick platinum serpentine circuit is deposited. This serpentine circuit acts both as a temperature sensor (monitoring the change in resistance as a function of temperature) and heater (by Joule effect). Four platinum contacts permit the external connection to the control devices (intensity source and voltage acquisition system). This 4-wire configuration allows to measure only the central area of the calorimeter known as the sensing area, which has a surface of 1.085 mm^2 .

On the other side of the membrane, and on top of the sensing area, a 200 nm thermal plate of Aluminum is deposited. The main function of this thermal plate is to improve the profile temperature homogeneity on the sensing area both in the steady state conditions and during the calorimetric scan (see Section 3.2.2.2).

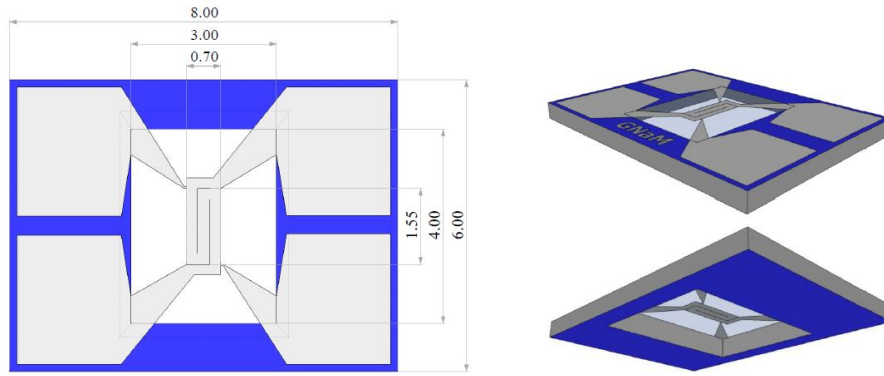


Figure 3. 2. Sketch of the nanocalorimeters used in the development of this work from different angles. The images show the most significant sizes in mm. Figure reprinted from [13].

The microfabrication process is described in Figure 3.3. It starts with a double-sided polished p-silicon wafer oxidized with a 50 nm thick silicon oxide film on top of which a 180nm thick low stress Si_3N_4 is grown by low pressure chemical vapor deposition (Figure 3.3a). Once the Si_3N_4 has been deposited, squared windows in the backside of the device are opened exposing the underlying silicon (Figure 3.3b). On the other side, in the front side of the calorimeter, the metallic elements are deposited forming the meander circuit and electrodes that define the calorimetric cell (Figure 3.3c). Finally, the silicon on the backside is removed by KOH anisotropic etching (Figure 3.3d), giving as a result a device with a trapezoidal cross-section and a free-standing silicon membrane. More details of the process can be found elsewhere [14].

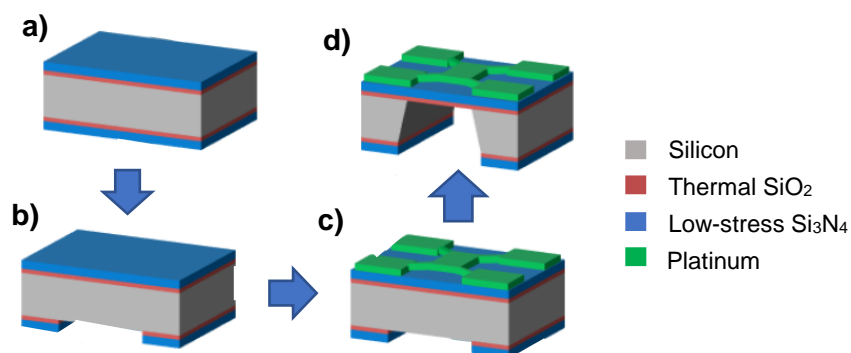


Figure 3. 3. Schematics of the different steps of the microfabrication process of the nanocalorimeters. (a) Thermal oxidation of the silicon wafer and growth of the 180 nm thick, low stress silicon nitride layers. (b) Opening of squared windows on the backside. (c) Deposition of the metallic elements. (d) KOH anisotropic etching of the silicon to release the silicon nitride membrane. Figure adapted from [13].

3.2.2.2 Operation principle

In general, any quantitative calorimetric measurement requires the simultaneous monitoring of the temperature evolution, the injected power and the heat losses to the surroundings. The calorimeter layout has a 4-wire configuration (Figure 3.4a): two contacts to inject current, $I(t)$, into the serpentine and two contacts to measure the voltage drop, $V(t)$, across the sensing area. When current is injected in the metallic element, it produces an increase in the temperature of the calorimetric cell and of the sample deposited just beneath it due to Joule effect. From the measurement of the instant voltage drop the power released to the sensing area can be inferred as $P_{in} = V(t)I(t)$. From the resistance of the heating element, $R(t) = V(t)/I(t)$, the temperature in the sensing area can be determined from the relation $R(T)$, previously obtained by calibrating the device, a procedure that is described in more detail in Section 3.3.1.2.

Figure 3.4c shows a sketch of the heat losses in the nanocalorimeters. In a vacuum environment, the thermal losses mainly consist of conduction across the SiN_x membrane and losses by thermal radiation (since conduction through air is suppressed in vacuum conditions). One of the fundamental distinctiveness of quasi-adiabatic nanocalorimetry is the injection of relatively high intensity pulses in very reduced time intervals (typically of the order of a few ms), which induces heating rates on the calorimetric cell of the order of $\beta \sim 10^4 \text{ K/s}$. These fast-heating rates, combined with the low thermal conductance across the membrane ($\sim 4 \mu\text{W/K}$ at room temperature) will minimize the thermal conduction between the sensing area and its surroundings during the measurements. On the other hand, for temperatures lower than 500 K, the losses for thermal radiation are minor and they can be corrected with a baseline subtraction [13]. Given that our experiments are performed in ultra-high vacuum (UHV) and in a range of temperatures below 500K, we can assume the measurements performed by this technique to be in the quasi-adiabatic regime.

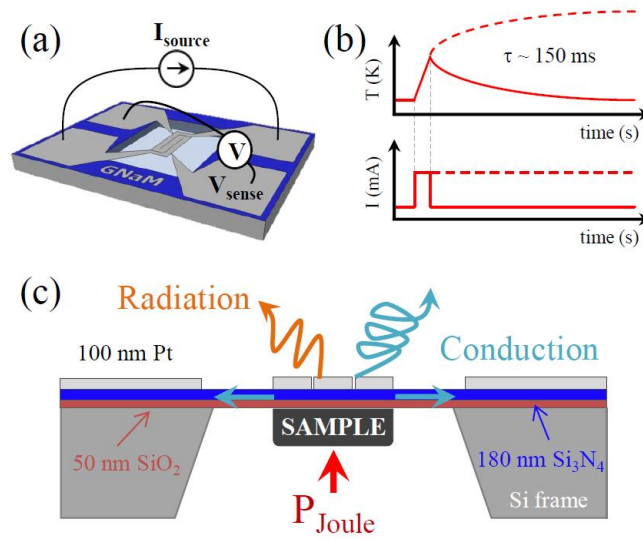


Figure 3. 4. Schematics of the principle of operation of the devices used for the development of this work. (a) Scheme of the connections of the nanocalorimeter with two contacts for current feeding and two for measuring the voltage drop. (b) Temperature dynamics in the nanocalorimeter in pulse mode (continuous line) and steady-state mode (dashed line). (c) Schematics of the cross-section of a nanocalorimeter, indicating the different parts and their size as well as power input and energy dissipation mechanisms. Figure reprinted from [13].

Even though we can minimize thermal losses by conduction imposing high heating rates, they are not completely negligible. Furthermore, in steady-state, heat conduction becomes even more relevant, and the temperature map tends to be parabolic, inducing temperature differences in the sensing area of several degrees [13]. Figure 3.5 shows the simulated temperature maps of the calorimetric cell obtained by COMSOL Multiphysics for a calorimeter in steady-state conditions (Figure 3.5a) and after a heating ramp at 8×10^4 K/s (Figure 3.5b). The specific values used for the simulation can be found elsewhere [13]. Although the temperature profile looks more homogeneous during a fast-heating ramp, a close look to the temperature distribution (see Figure 3.6a) shows that the dispersion is not only not negligible, but it also changes as a function of temperature (indicated as elapsed time in the graphical representation).

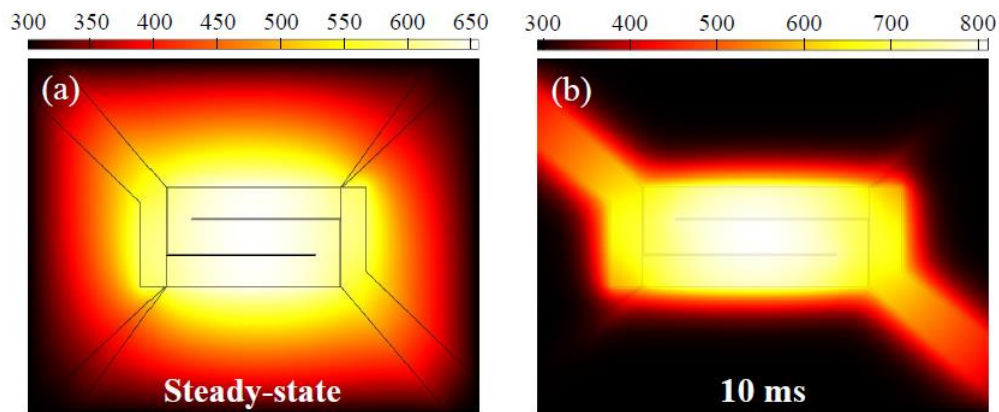


Figure 3.5. COMSOL simulation of the temperature profile in a calorimetric cell (a) in steady state conditions and (b) during a heating scan at 8×10^4 K/s. Figure reprinted from [13].

In order to reduce the temperature inhomogeneity across the sensing area a thermal diffusive layer is deposited on top of the membrane, even at expenses of increasing the specific heat of the device, therefore, reducing the sensitivity. As it can be observed in Figure 3.6b, including a thermal plate of 200 nm of Aluminum avoids the degradation of the temperature profile on top of the sensing area over time and temperature.

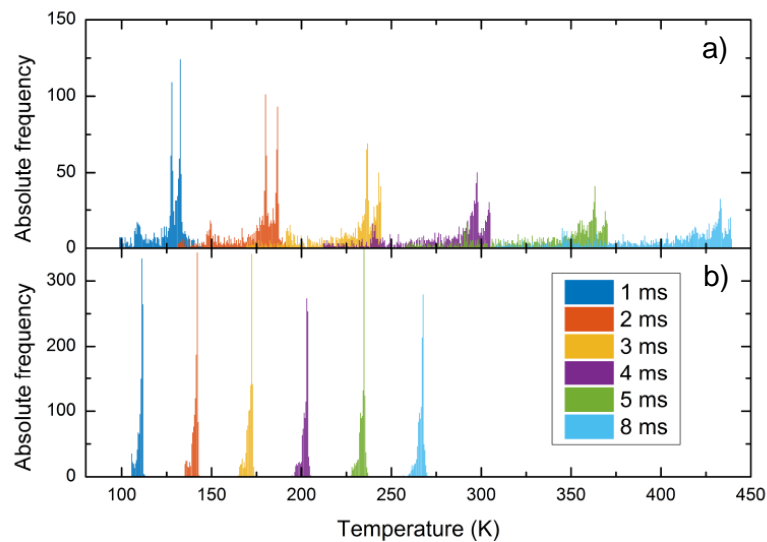


Figure 3. 6. Histogram of the temperature profile at the sensing area of (a) a nanocalorimeter without thermal plate and (b) a nanocalorimeter with a 200nm Aluminum plate for same intensity current pulses during different amounts of time (indicated in the legend). Longer current pulses translate into higher temperatures in the sensing area and the thermal plate avoids the degradation of the temperature profile. Reprinted from [15].

Measuring in differential mode allows for a significative enhancement of the sensitivity. In this configuration, a couple of twin calorimeters with almost identical heat capacity and temperature-resistance dependence ($R(T)$ relationship) are used simultaneously. One of the calorimeters is loaded with the sample and the other is used as reference to subtract the background contribution, allowing to amplify the calorimetric signal generated by the sample while excluding from the amplification the information coming from the surroundings. A measurement performed with a single calorimeter can be amplified around a factor 3 while, using the differential mode, the differential signal can be amplified up to 500 times.

3.2.2.3 Heat capacity derivation

The heat capacity of the samples is extracted from the voltage drop across the devices after injecting a short intensity pulse. Under adiabatic conditions, all the input power, $P = V \cdot I$, is spent on heating the sensing area. This increase in temperature is related to the heat capacity of the system as

$$C_p(T)dT = V(t)I(t)dt = P(t)dt \quad (3.1)$$

The heat capacity of the calorimetric cells can also be expressed as a function of the measured variables V and I . In that case the expression for $C_p(T)$ can be written as

$$C_p(T(t)) = \frac{V(t)I(t)}{\beta(t)} \quad (3.2)$$

where $\beta(t) = \frac{dT(R)}{dt}$ is the heating rate. The temperature as function of time, $T(R)$, can be obtained by measuring the resistance and applying the relationship between resistance and temperature found in the calibration process (see Section 3.3.2.2).

In the differential configuration, the heat capacity of the sample can be measured as the differential calorimetric signal of both sensors, sample and reference:

$$\Delta C_p(T(t)) = \frac{V_S I_S}{\beta_S} - \frac{V_R I_R}{\beta_R} = \frac{V_R I_R}{\beta_R} \left(\frac{V_S I_S \beta_R}{V_R I_R \beta_S} - 1 \right) \quad (3.3)$$

where subscripts S and R stand for sample and reference, respectively. Note that for simplicity and since all the magnitudes depend on time, we have omitted this variable from the equations. Up until now no assumptions or simplifications have been made in

the development of this calculation, however for this work some assumptions can be safely made in order to simplify our analysis. In first place, the two calorimeters are connected in series to ensure that the same current is fed to both of them. Therefore, $I_S = I_R = I$. In second place, for our measurements the calorimeters are fed with constant current pulses (intensity constant over time). Thus, the voltage and resistance derivative are related by $dV = d(IR) = IdR$ since $V = IR$. Finally, we can include the differential voltage, ΔV , which contains the information of the sample with the relation $\Delta V = V_S - V_R$. Using all the considerations above, the expression for the heat capacity can be rewritten as:

$$\Delta C_p = \frac{I\Delta V}{\beta_S} + \frac{IV_R}{\beta_S} \left(1 - \frac{\beta_S}{\beta_R}\right) \quad (3.4)$$

In this expression, the term ΔV can be heavily amplified. However, the term $\frac{\beta_S}{\beta_R}$ introduces a lot of noise in our signal. A strategy to significantly reduce this noise and obtain reliable data is following the development used by Efremov *et al* [7]. This approach consists of substituting the term $\frac{\beta_S}{\beta_R}$ for an indirect calculation using parameters obtained during the calorimetric measurements (specifically from the differential signal, ΔV). Including this change in Equation 3.3 we obtain:

$$\frac{d\Delta V}{dt} = \frac{dV_S}{dT_S} \beta_S - \frac{dV_R}{dT_R} \beta_R \rightarrow \frac{\beta_S}{\beta_R} = \frac{(d\Delta V/dt)}{\beta_R(dV_S/dT_S)_t} + \frac{(dV_R/dT_R)_t}{(dV_S/dT_S)_t} \quad (3.5)$$

where the subscript “t” refers to the derivative at constant time. Finally, introducing all the considerations made until now, the final expression for the difference between both heat capacities can be written as:

$$\Delta C_p(T_S(t)) = \frac{I\Delta V}{\beta_S} - \frac{V_R(d\Delta V/dt)_t}{\beta_S\beta_R(dR_S/dT_S)_t} + \frac{IV_R}{\beta_S} \left(1 - \frac{(dR_R/dT_R)_t}{(dR_S/dT_S)_t}\right) \quad (3.6)$$

where the temperature derivative of the resistance can be calculated using the $R(T)$ relationship of the metallic element (obtained following the procedure indicated in Section 3.3.2.2).

Even though the pair of calorimeters sample-reference are chosen to be as similar as possible, there are always some differences. Therefore, the differential signal obtained in the measurement does not correspond exclusively to the heat capacity of the sample, but

rather to a combination of the heat capacity of the sample and the excess heat capacity introduced by the difference in the C_p of the two cells. In order to take this into account, we need to previously carry out measurements with both cells empty so we can determine their heat capacity before the sample is deposited. This process is known as the baseline correction. When comparing the loaded sample cell, ΔC_p , and the empty one, ΔC_p^0 , we can see a mismatch between the measured temperatures in both calorimeters for a given time. This can be explained by the difference in mass: the loaded cell will have a higher heat capacity and therefore the heating rate will decrease substantially. Knowing the relative temperature evolution between both cells and between the baseline and the loaded sample measurements, it is possible to determine the excess subtracted heat capacity ($\Delta C_p - \Delta C_p^0$). The heat capacity of the sample can be expressed as:

$$C_p^{Sample}(T_S) = \Delta C_{p,S}(T_S) - \Delta C_{p,S}^0(T_S) + \Delta C_{p,R}(T_S) - \Delta C_{p,R}^0(T_S) \quad (3.7)$$

It is also possible to further reduce the noise by performing multiple scans and averaging the output data. This is used specially to reduce the noise in the baseline, where typically 100 scans are taken, as well as in measurements involving reversible processes.

3.2.3 Atomic Force Microscopy (AFM)

Atomic force microscopy (AFM) is a powerful tool to investigate surface properties and structure of materials in the nanometric scale. This technique is a high-resolution type of scanning probe microscopy (SPM) that can image almost any type of surface, including glass, polymers, ceramics, and biological samples, among others. One of the main advantages of AFM with respect to other SPM techniques is the fact that the type of surface and environment are not considered as important limitation factors, measurements can be made in atmosphere-controlled conditions, on liquid surfaces, vacuum, etc. Additionally, samples imaged by AFM require no special treatment (like metal or carbon coatings, drying or freezing procedures, etc.) that would irreversibly change or damage the sample, making it a very versatile tool for all kinds of experiments.

The atomic force microscope consists of a cantilever with a sharp tip (probe) - typically of less than 10 nm radius of curvature, which scans across the sample surface using a piezoelectric element controlled by a computer. When the tip is brought into proximity

of a sample, interaction forces between the tip and the sample lead to a deflection of the cantilever according to Hooke's law. This deflection is monitored using an optical detection system that consists of a laser beam which reflects off the back of the cantilever onto a four-quadrant photodiode, obtaining an electric signal which intensity is proportional to the displacement of this probe. A feedback loop maintains a constant interaction between the tip and the sample as the tip scans the sample (Figure 3.8). The system detects the cantilever motion during the scan, typically either by monitoring the vertical deflection (contact mode) or the amplitude (tapping mode). The tip movements, normal to the surface, are digitally recorded and can be processed and displayed in three dimensions. This technique has a lateral (X-Y) resolution of 1-5 nm with height resolutions of around $\sim 1 \text{ \AA}$, making it the ideal tool for surface imaging or measuring surface roughness.

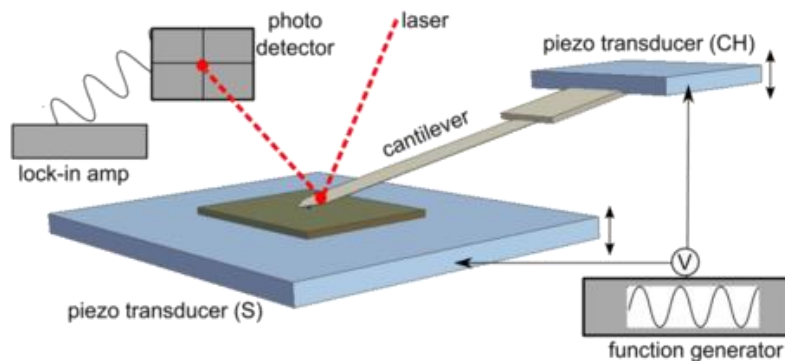


Figure 3. 7. Sketch of a typical atomic force microscope (AFM) set up. Generally, AFM uses the force existing between the probe and the sample to build an image of the scanned surface. The tip is brought in close contact with the sample through a set of piezoelectric materials that can move with sub-nanometer precision. The reflected laser beam focused on the back side of the cantilever is detected by a photodiode, which provides information on the position of the probe and how it changes on the surface of the sample. At each position the cantilever deflection is measured and from this measurement a topography map can be constructed. Figure reprinted from [16].

AFM can be operated in several modes depending on the application. The most used applications are topographic imaging, force measurements and sample manipulation.

For the development of this work, we will focus mainly on topographic imaging. In this category, three different modes can be used depending on the nature of the tip motion: Contact Mode, Tapping or Intermittent contact Mode and Non-contact Mode (see Figure

3.9). For the present study we use the Intermittent contact Mode, which will be briefly explained down below.

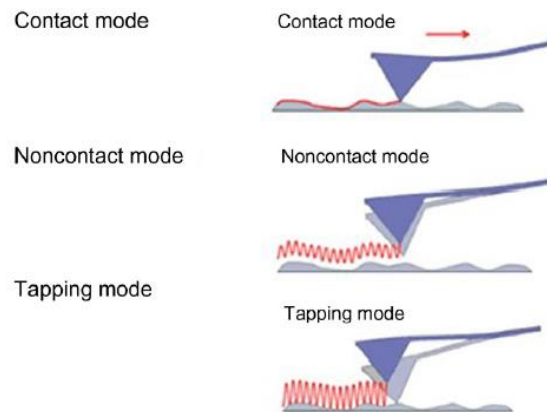


Figure 3. 8. Sketch of the movement of the probe on top of the sample surface for the three main AFM topographic imaging modes: contact mode, non-contact mode and tapping or intermittent mode. Figure extracted from [17].

The Intermittent contact mode, also known as Tapping Mode or Amplitude Modulation Mode (AM-AFM mode) is probably the most frequent used AFM mode when operating in ambient conditions or in liquids thanks to the wide range of properties that can be tackled by the tapping process.

In this mode, the cantilever oscillates at or near its resonant frequency using a piezoelectric as the mechanical excitation source. When the tip is not in contact with the surface (the so-called free amplitude) the piezoelectric motion causes the cantilever to oscillate with high amplitudes (in the order of tens of nm). When the tip approaches the surface, interactions with different attractive forces start to induce changes in the oscillations and the amplitude is slightly decreased. And finally, when the tip starts tapping or touching the surface, this amplitude of oscillation is again reduced and we enter the so-called semi-contact range. This is the range of work for the tapping mode and, once we achieve it, the system is ready to start scanning the sample.

In tapping mode, the frequency and amplitude of the driving signal are kept constant, leading to a constant amplitude oscillation of the cantilever as long as there is no interaction with the surface. When there are changes on the surface topography which reduce the distance between the cantilever and the sample, the amplitude of oscillation

decreases due to the reduction in space to oscillate; and, in an opposite way, when the probe scans over a zone where the cantilever is further away from the surface the amplitude of oscillation increases since the cantilever has more room to oscillate (Figure 3.10). Using these changes in oscillation, the system is set to keep the amplitude of the vibration constant to a desired setpoint so the distance between the probe and the surface remains constant and this way the topography of the surface is revealed.



Figure 3. 9. Sketch of the amplitude oscillation changes in tapping mode to probe the samples' surface.

In contrast with contact mode, the tapping mode presents poorer resolution because of the larger distances between the tip and the sample (thus, weaker interactions). However, this is one of the most suitable working modes to imagine soft organic surfaces due to reduced sample degradation. In tapping mode, the mechanical contact is strongly reduced and this translates into lower probabilities of the material to be pulled sideways by shear forces, modifying the measured surfaces or getting stuck on the tip.

3.3 Experimental set up

3.3.1 Deposition chamber

The UHV (ultra-high vacuum) chamber used for the deposition of the samples studied in this work is shown in Figure 3.10. In this Figure we can also see highlighted the main elements needed for the correct growth and later study of the thin films. Since all the samples were grown by PVD in the same chamber, most elements are common in all depositions. However, depending on the posterior characterization, whether it is *in situ*

(for nanocalorimetry measurements) or *ex situ* (for DSC and AFM measurements), the sample setup will change slightly as we will see further below.

The UHV is achieved in the chamber thanks to a turbomolecular pump attached to a dry scroll pump. For this set up a Variant SH-110 scroll pump has been used to generate the primary vacuum and then a Variant Turbo-V 301 turbomolecular pump (Figure 3.10 (1)) has been added to achieve the UHV levels needed for the deposition process, 3×10^{-8} mbar. The pressure of the system is measured by a Bayard-Alpert hot filament ionization gauge located at one of the front ports (Figure 3.10(3)).

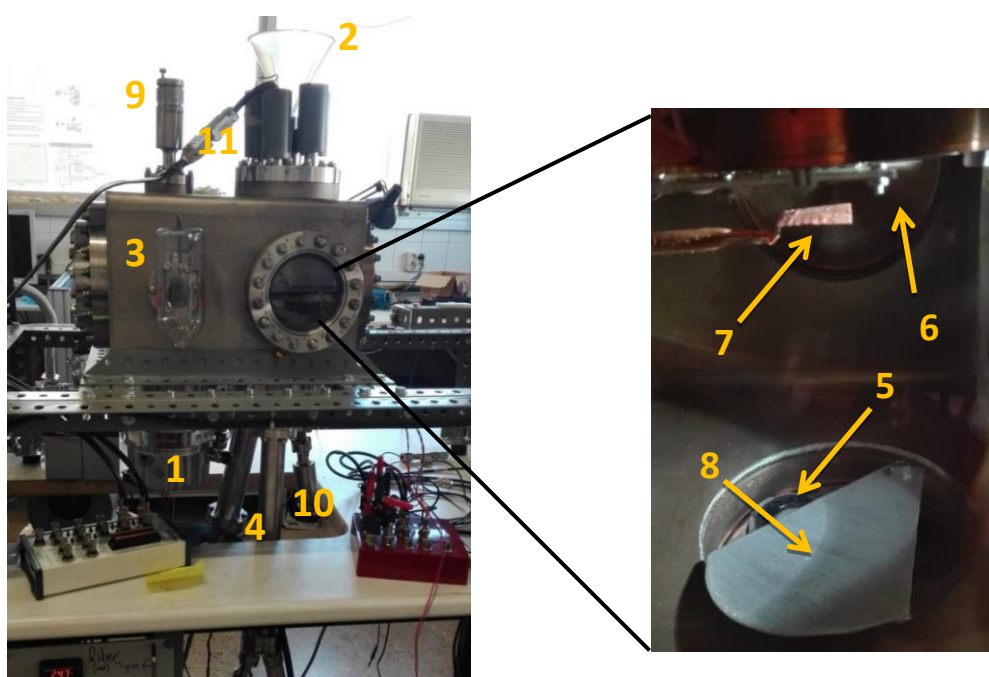


Figure 3. 10. Set up of the UHV deposition chamber used for the growth of the films studied in this thesis. (1) Turbomolecular pump. (2) Nitrogen *cold trap*. (3) Bayard-Alpert hot filament ionization gauge. (4) Effusion cells. (5) Effusion cells inside the deposition chamber, where the crucibles are placed. (6) Quartz crystal microbalance (QCM). (7) and (8) shutters. (9) and (10) external ports of the shutters. (11) electrical feedthrough.

To further improve the vacuum level a copper *cold trap* has been installed on top of the chamber with a feedthrough to the exterior so it can be filled with liquid nitrogen (Figure 3.10 (2)). This *cold trap* constitutes a big copper surface inside the chamber that when refrigerated at 77 K (liquid nitrogen boiling point) allows us to remove the remaining small molecules (not removed with the mechanical pumps), mainly water, by condensation on its surface. Using the *cold trap*, we can improve our vacuum level in

about one order of magnitude achieving environments of 10^{-9} mbar. A picture of the cold trap used for this work can be seen in Figure 3.11.



Figure 3. 11. (Upside down) Copper *cold trap* used to improve the vacuum level in the deposition chamber.

At the bottom part of the chamber, we installed two effusion cells as vapor sources, which allow an accurate control of the vapor pressure and deposition rate. For this work the chamber is equipped with two low temperature effusion cells (Figure 3.10 (4)) in order to grow multilayers of two different materials without breaking the vacuum. These evaporators consist typically of a crucible where the material is loaded and then heated radiatively via a hot filament (which ensures a good temperature uniformity across the cell) up to temperatures slightly above its melting point. For this specific experiment, a Createc low-temperature effusion cell and an organic effusion cell from MBE Komponenten were used with a stainless-steel and quartz crucible, respectively. The top openings of the effusion cells inside the chamber that lead the vapor to the substrate can be appreciated in Figure 3.10(5). The temperature is monitored and controlled by a K-type thermocouple with a proportional-integral-derivative (PID) system.

The evaporation rate of the samples is monitored with a quartz crystal microbalance (QCM) placed near the sample holder (Figure 3.10 (6)), which allows us to follow the thickness evolution of the deposited material in real time. In this work, we typically use an evaporation rate of 0.07-0.08 nm/s. QCMs measure mass variation per unit area by measuring the change in frequency of the quartz crystal, which depends, mainly, on the

mass that is arriving to the device. The changes in frequency however are also sensitive to thermal variations so before starting the deposition process it is important to ensure the thermal stability of the microbalance. Since the QCM is not in the same position as the substrate, it needs to be calibrated first to ensure a correct reading. This calibration is usually performed growing a few samples with different thicknesses and comparing the QCM reading with *ex situ* profilometry measurements.

There are two different shutters in the system: one, at a higher position (Figure 3.10(7)), used to (i) cover the substrate until having a stable evaporation rate to avoid material mixing when changing from one source to the other, and (ii) to terminate the evaporation process after reaching the desired thickness; and a second one, installed right on top of the evaporation sources (Figure 3.10(8)) to allow the evaporation of only the desired material. This configuration allows us to have both effusion cells at high temperature while only one of the materials can reach the substrate, increasing the time efficiency of the process. Numbers (9) and (10) in Figure 3.10 correspond to the external ports of shutters (7) and (8), respectively.

As discussed in Chapter 2, the substrate temperature during the deposition process is a critical factor for the growth of glasses with high stabilities. For that reason, the sensing devices and substrates (nanocalorimeters, and Si and Al substrates) are placed on a custom-build socket which allows us to control the temperature and extract the required electrical signals for the measurements. The socket is fabricated with a one-sided photoresist board where the circuit for the electrical connections is printed by means of conventional photolithography techniques. The circuit used for this work is shown in Figure 3.12a and consists basically of eight tracks, to connect both nanocalorimeters in a 4-wire configuration, and four extra tracks for the temperature sensor, in this case two Pt100.

For this specific set up, the socket is attached to the base of the *cold trap* which acts as a heat sink, allowing us to set the temperature bath for the sample's socket. A steel screw (Figure 3.12) provides the thermal link between the socket and the *cold trap* achieving base temperatures of around 130 K (~55 K above the cold trap temperature).

Depending on the subsequent characterization of the samples, if it is *in situ* or *ex situ*, two different configurations of the socket are used. For *in situ* measurements, the

configuration used is the one shown in Figure 3.12a. In this case, the deposition is made directly on the membrane of the nanocalorimeters.

In the case of *ex situ* measurements, the socket is covered with copper tape to achieve a more homogeneous temperature profile on the back side, where the substrates (typically Si for AFM measurements and Al for DSC) are assembled (see Figure 3.12b).

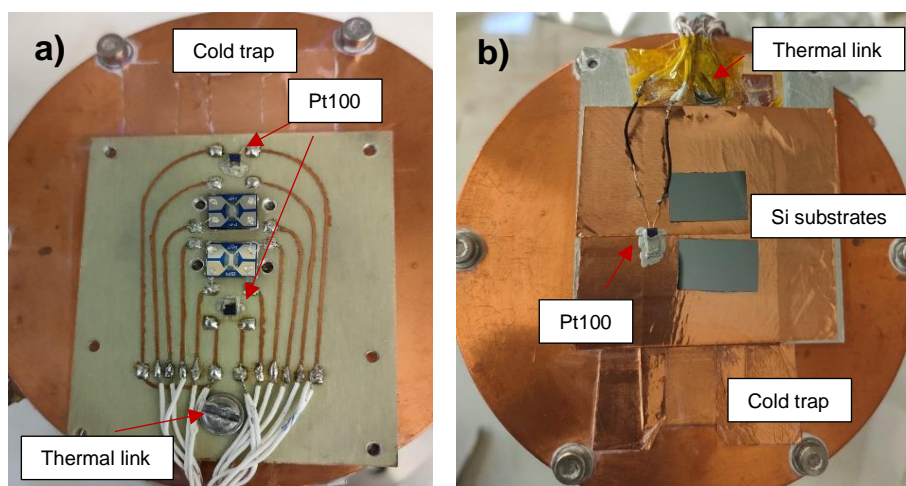


Figure 3. 12. Images of the temperature-controlled socket for (a) *in situ* measurements (nanocalorimetry) and (b) *ex situ* measurements (DSC and AFM). The socket is attached to the *cold trap*, which acts as a heat sink. The temperature is monitored and controlled by Pt100 sensors and a home-made Labview software.

In all cases, the temperature of the socket can be monitored and controlled thanks to an incorporated Pt100 sensor and a couple of resistances that act as heaters. Connections to the outside of the chamber are made via electrical feedthroughs (Figure 3.10 (11)). A home-made Labview software allows us to control the power supply and the resistance measurement for temperature monitoring and control.

3.3.2 Experimental set up for nanocalorimetry measurements and measurement protocol

Two temperature-calibrated nanocalorimeters are placed on the temperature-controlled socket and mounted inside the vacuum chamber, where they are set at a reference temperature (for most of the measurements in this thesis it will be 200 K). In first place, and with both calorimeters still empty, a sequence of temperature scans is performed and

averaged to obtain the baseline (typically pulses of 35 mA and 8 ms are used for this work). The raw voltage data is acquired with a data acquisition (DAQ) system NI PXIe-1073 (with an acquisition frequency of 4MHz) and box averaged to increase the signal-to-noise ratio.

After the measurement of the baseline, the sample is grown by physical vapor deposition on the calorimetric cell at a certain deposition temperature, which can be determined by feeding the calorimeter with a stationary current. Once the sample is deposited, another temperature scan using the same parameters as the ones used for the baseline is performed and the data acquired. These parameters are chosen according to the maximum temperature we want to achieve in the sensing area. For organic molecules, if the temperature during the scan reaches a high enough value, it can cause the sample to evaporate. This is one of the main advantages of this technique since it allows to do *in situ* measurements. The fact that the samples can be grown, measured and removed without having to break the vacuum allows us to do measurements consecutively saving time between measurements and avoiding the exposure of the samples to environmental conditions before their characterization.

Due to the low mass of the calorimetric cells, immediately after the intensity pulse, the passive cooling rates achieved are of the order of 500 K/s. These fast-cooling rates may have a crucial impact on the properties of the sample (for instance its stability) as we will see in following chapters.

3.3.2.1 Conditioning of the nanocalorimeters

When performing calorimetric studies, a precise measurement of the temperature is essential. Therefore, we need to know the exact relationship between the resistance of the platinum serpentine and the temperature, $R(T)$, in the working temperature range, which in our case expands from 200 K up to ~550 K. Before starting the calibration process, however, the devices go through a conditioning process consisting of several steps: i) cleaning of the calorimetric cells, ii) alignment of deposition masks and thermal plate evaporation and iii) thermal stabilization of the calorimetric device. After the conditioning process, the calorimetric devices are ready to be calibrated. The description of the three processes is detailed in the following lines:

- i) Cleaning of the calorimetric cells. To increase the survival rate of the membranes during the cutting and manipulation of the wafers, a 5 to 10 μm Si layer is maintained when doing the KOH etching process during the microfabrication process. This remaining layer is later removed by applying the same KOH solution at room temperature in controlled intervals of time. Figure 3.13 shows a sequence of images depicting the process.

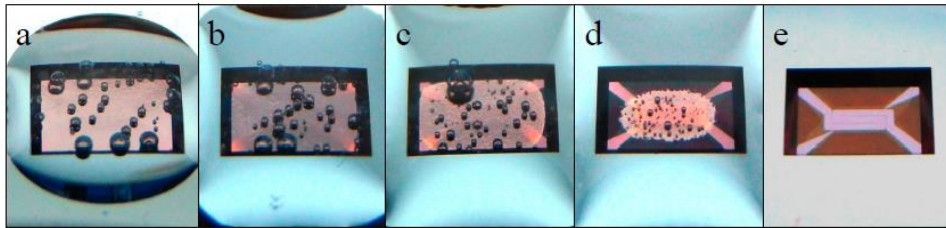


Figure 3.13. Sequence of images where the final Si etch onto the membrane with KOH can be observed. Figure reprinted from [13].

- ii) Alignment and thermal plate deposition. To ensure a good measurement of the sample and good temperature maps, it is important that the sample is selectively deposited on top of the sensing area of the calorimeter. Thus, a shadow mask was microfabricated in silicon to delimit the deposition area (see Figure 3.14). This mask is also used to delimit the physical vapor deposition of the 200nm Al thermal plate.

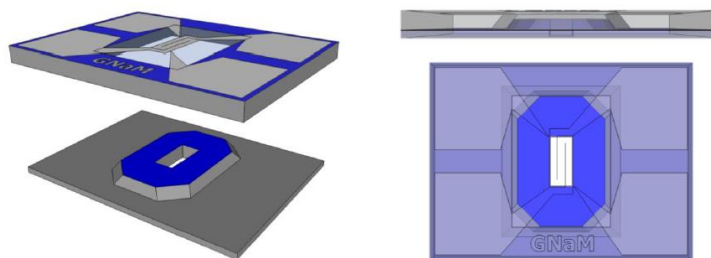


Figure 3.14. Sketch of the deposition masks (or shadow masks) together with a nanocalorimeter from different angles. Reprinted from [13].

- iii) Thermal stabilization of the calorimetric device. In order to avoid a degradation of the resistance as a function of temperature during the

measurements in the temperature working range, a thermal stabilization process is carried out. This process consists of two steps: an isothermal annealing above the highest temperature used during the experimental work (~600 K) followed by a sequence of 600 to 1000 high intensity pulses.

3.3.2.2 Calibration process

The resistance-temperature relationship of the platinum in the temperature range used for this work (between 200-550K) can be well approximated by a quadratic dependence, known as the Calendar-Van-Dusen equation:

$$R(T) = R_0(1 + \alpha(T - T_0) + \beta(T - T_0)^2) \quad (3.8)$$

In order to find the specific values for this relationship, the nanocalorimeters are placed in a temperature-controlled socket where measurements of the resistance at different temperatures are performed (Figure 3.12). For a better temperature homogeneity between the temperature-controlled socket and the sensing area of the calorimeters, the calibration process is carried out under argon atmosphere at near-ambient pressure conditions. Once the calorimeters are thermalized at a given temperature, current/voltage pulses of very low intensities are performed and the resistance is inferred. It is important to note that even though these pulses are performed at low intensities and for short amounts of time (typically 2mA to 5mA and times of 5ms) the devices can present self-heating. In order to find the value of the resistance when no self-heating has been produced, an extrapolation to $t=0$ s of the averaged measurement of the resistance is performed. Usually, the resistance is measured every 10K in the whole working temperature range in order to obtain enough data to ensure a proper fitting of Equation 3.8. For the lower temperature range, below room temperature, liquid nitrogen is used to refrigerate the socket.

Plotting the resulting resistance of the calorimeters used for this work for different temperatures and adjusting them by a second order polynomial fit, we obtain the calibration curves shown in Figure 3.15. From this calibration curves the values of R_0 , T_0 , α and β are obtained.

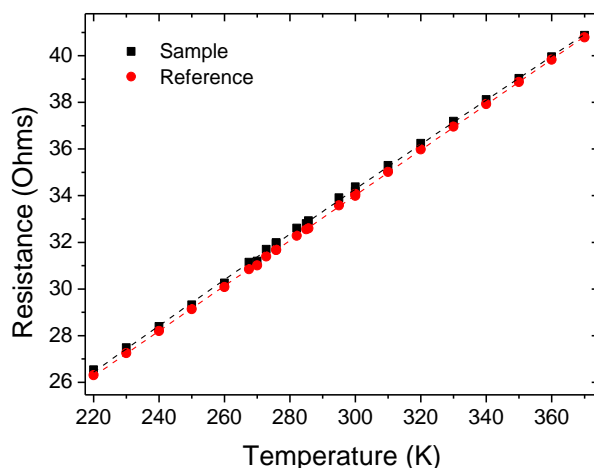


Figure 3. 15. Resistance versus temperature curves of the sample (black squares) and reference (red circles) nanocalorimeters used in this work. The $R(T)$ curve is calculated by a quadratic fitting of the measured values of resistance in the whole temperature range (marked as dashed lines in the figure).

3.3.3 Experimental set up for DSC measurements

For the DSC measurements, Aluminum substrates are placed on the temperature-controlled socket as shown in Figure 3.12b and the temperature is set at 285 K (0.85T_g for the TPD molecule). The samples are grown by physical vapor deposition with a thickness of around 35 μm.

Once the films are deposited, the samples are moved to a conventional DSC, in this particular case to a power compensated DSC7 from Perkin Elmer (Figure 3.16). The samples are introduced in one of the Aluminum pans while the other is left empty as a reference for the differential measurement. A cooling system maintains a base temperature of 273 K and Argon gas flows during the measurements helping the overall temperature homogeneity and providing a non-oxidizing environment. Finally, the calorimetric ramps consist of heating scans at 10 K/min from base temperature up to 380 K.

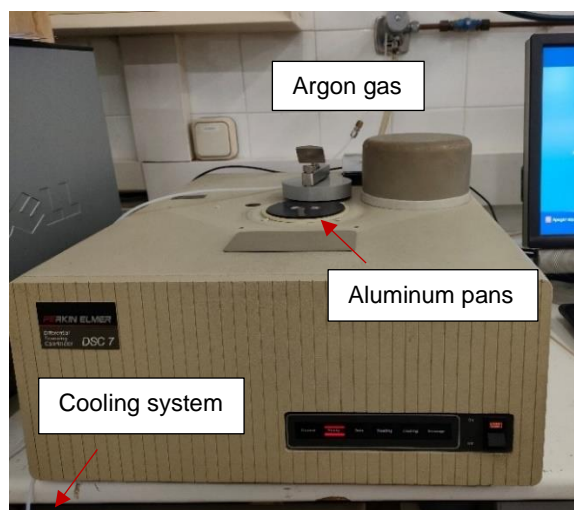


Figure 3. 16. Photo of the DSC used to measure the bulk samples. The heating/cooling ramps for the measurements were performed at 10K/min from the base temperature (273K) up to 380K.

3.3.4 Experimental set up for AFM measurements

Samples, in this case, are vapor deposited on top of Si substrates as shown in Figure 3.12b at a deposition temperature of 285K. In an analogous way to the DSC measurements, once the samples are deposited, they are extracted from the chamber and brought to the atomic force microscope to be characterized. The AFM measurements in this work were performed at Institut Català de Nanociència i Nanotecnologia (ICN2) with a Keysight Technologies 5500 AFM (Figure 3.17a).

The AFM used for our studies has a temperature stage that allows to heat up the sample to study the glass transition of the organic films (Figure 3.17b). The temperature is monitored with a Pt100 placed on top of the thermal plate as close as possible to the substrate to ensure an accurate measurement. The heating rates for the experiments are set at 5K/min (as recommended by the manufacturer) and in order to ensure not overheating the sample the thermal protocol is designed to stop at $T_g - 5K$ and wait until thermal stability is reached. A calibration procedure is also performed placing a second Pt100 on top of the Si substrate and comparing the values obtained for both Pt100, the one on top of the substrate and the one in contact with the thermal plate. It was observed that uncertainties of around 1K were found for all temperatures. The X, Y and Z dimensions of the piezo-scanner were also calibrated, in this case, using reference

samples: PS-PMMA block copolymers were used for small scans ($1 \times 1 \mu\text{m}^2$), while commercial calibration gratings were used for larger scans (up to $20 \times 20 \mu\text{m}^2$).

For this study the AFM is operated in tapping mode using microfabricated silicon cantilevers with ultrasharp silicon tips with nominal radius $R < 10 \text{ nm}$. For the measurements the resonance frequencies were around 250 kHz and the scans were set at $20 \times 20 \mu\text{m}^2$ in order to image as much area of the sample as possible without compromising the image resolution, making it easier to follow the transformation dynamics. Each scan consists of 512 points per line and 2 lines per second, therefore each image takes a total of 256s to complete (slightly above 4min). Lower acquisition times were tested resulting in poor resolution images.

The obtained images are analyzed with the software *WSxM*, which makes it possible to study properties such as height, amplitude and phase difference directly from the data registered with the AFM.

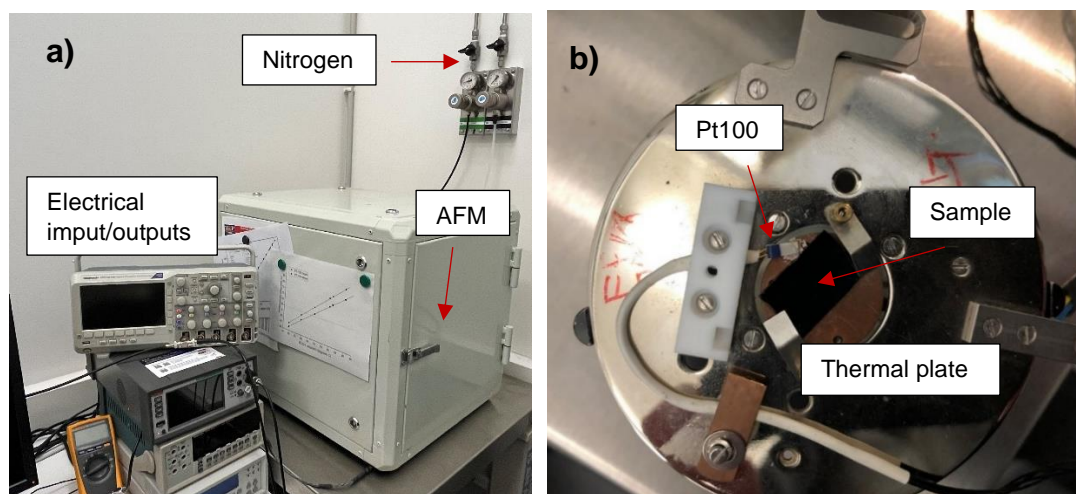


Figure 3. 17. a) Experimental set up for AFM measurements. The AFM is enclosed in a chamber vibrationally isolated and with a relative humidity below 10%, which is achieved by circulating nitrogen. b) Temperature stage, which allows the heating and monitoring of the temperature on the sample.

3.4 Materials

Two different organic molecules have been used for the development of this work: N,N'-Bis (3- methylphenyl)-N,N'-diphenylbenzine also known as TPD and Tris(4-carbazoyl-9ylphenyl)amine or TCTA used as the capping material for the TPD thin films.

Both molecules, TPD and TCTA, are organic semiconductor hole transport materials used mainly in organic electronics, being TPD a molecule widely used for OLED (Organic Light Emitting Diodes) fabrication. TPD's melting point is located around 450 K and its glass transition temperature can be found at 333 K [18]. It was acquired from Sigma-Aldrich (now known as Merck) in powder form with a purity level above 99% and used without further treatment. Regarding the TCTA molecule, it has a melting temperature that ranges between 571 and 573 K and a glass transition temperature of 424 K [19]. It was also purchased in the crystalline phase from Sigma-Aldrich with a purity higher than 97% and used without further treatment. Figure 3.18 shows a scheme of the two different compounds.

The different samples have been prepared in all cases with a deposition rate of 0.08nm/s for both TPD and TCTA. The deposition temperatures range from $0.85T_g$ to $1.02T_g$ for TPD and the TCTA layers are grown in all cases at the same temperature as the TPD layer.

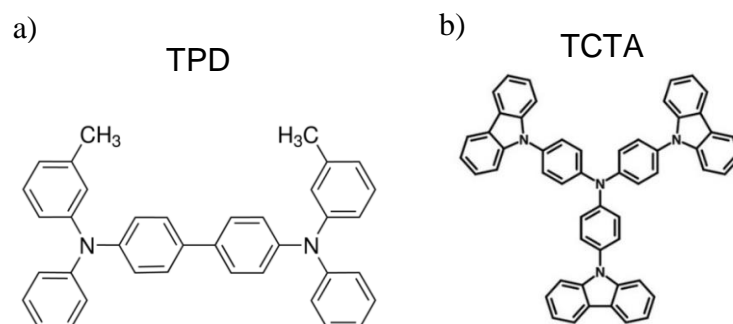


Figure 3. 18. Representation of the chemical structure of the molecules used in this work: a) TPD and b) TCTA.

References

- [1] V. Svorcik, V. Rybka, K. Efmenko, and V. Hnatowicz, *Deposition of Polystyrene Films by Vacuum Evaporation*, *J Mater Sci Lett* **16**, 1564 (1997).
- [2] J. Zhang, C. Con, and B. Cui, *Electron Beam Lithography on Irregular Surfaces Using an Evaporated Resist*, *ACS Nano* **8**, 3483 (2014).
- [3] A. N. Raegen, J. Yin, Q. Zhou, and J. A. Forrest, *Ultrastable Monodisperse Polymer Glass Formed by Physical Vapour Deposition*, *Nat Mater* **19**, 1110 (2020).
- [4] D. M. Mattox, *Chapter 1 - Introduction*, in *Handbook of Physical Vapor Deposition (PVD) Processing (Second Edition)*, edited by D. M. Mattox (William Andrew Publishing, Boston, 2010), pp. 1–24.
- [5] Y. Guo, A. Morozov, D. Schneider, J. W. Chung, C. Zhang, M. Waldmann, N. Yao, G. Fytas, C. B. Arnold, and R. D. Priestley, *Ultrastable Nanostructured Polymer Glasses*, *Nat Mater* **11**, 337 (2012).
- [6] E. A. Olson, M. Y. Efremov, M. Zhang, Z. Zhang, and L. H. Allen, *The Design and Operation of a MEMS Differential Scanning Nanocalorimeter for High-Speed Heat Capacity Measurements of Ultrathin Films*, *Journal of Microelectromechanical Systems* **12**, 355 (2003).
- [7] M. Yu. Efremov, E. A. Olson, M. Zhang, S. L. Lai, F. Schiettekatte, Z. S. Zhang, and L. H. Allen, *Thin-Film Differential Scanning Nanocalorimetry: Heat Capacity Analysis*, *Thermochim Acta* **412**, 13 (2004).
- [8] A. F. Lopeandía, L. I. Cerdó, M. T. Clavaguera-Mora, L. R. Arana, K. F. Jensen, F. J. Muñoz, and J. Rodríguez-Viejo, *Sensitive Power Compensated Scanning Calorimeter for Analysis of Phase Transformations in Small Samples*, *Review of Scientific Instruments* **76**, 065104 (2005).
- [9] J. Rodríguez-Viejo and A. F. Lopeandía, *Quasi-Adiabatic, Membrane-Based, Highly Sensitive Fast Scanning Nanocalorimetry*, in *Fast Scanning Calorimetry*, edited by C. Schick and V. Mathot (Springer International Publishing, Cham, 2016), pp. 105–149.
- [10] M. Abd-Elghany and T. M. Klapötke, *A Review on Differential Scanning Calorimetry Technique and Its Importance in the Field of Energetic Materials*, **3**, (2018).
- [11] D. W. Denlinger, E. N. Abarra, K. Allen, P. W. Rooney, M. T. Messer, S. K. Watson, and F. Hellman, *Thin Film Microcalorimeter for Heat Capacity Measurements from 1.5 to 800 K*, *Review of Scientific Instruments* **65**, 946 (1994).
- [12] S. L. Lai, G. Ramanath, L. H. Allen, and P. Infante, *Heat Capacity Measurements of Sn Nanostructures Using a Thin-Film Differential Scanning Calorimeter with 0.2 NJ Sensitivity*, *Appl Phys Lett* **70**, 43 (1997).
- [13] M. Molina Ruiz, *Nanocalorimetric Studies of Size Effects in Magnetic Oxides and Formation Kinetics in Silicides*, Universitat Autònoma de Barcelona, 2014.
- [14] A. Fernández Lopeandía, *Development of Membrane-Based Calorimeters to Measure Phase Transitions at the Nanoscale*, Universitat Autònoma de Barcelona, 2007.
- [15] Joan Ràfols-Ribé, *Organic Vapour-Deposited Stable Glasses: From Fundamental Thermal Properties to High-Performance Organic Light-Emitting Diodes.*, Universitat Autònoma de Barcelona, 2017.

- [16] National Institute of Standards and Technology (NIST), *Scanning Probe Microscopy for Advanced Materials and Processes*, <https://www.nist.gov/programs-projects/scanning-probe-microscopy-advanced-materials-and-processes>.
- [17] R. Asmatulu and W. S. Khan, *Chapter 13 - Characterization of Electrospun Nanofibers*, in *Synthesis and Applications of Electrospun Nanofibers*, edited by R. Asmatulu and W. S. Khan (Elsevier, 2019), pp. 257–281.
- [18] J. Ràfols-Ribé, A. Vila-Costa, C. Rodríguez-Tinoco, A. F. Lopeandiá, J. Rodríguez-Viejo, and M. Gonzalez-Silveira, *Kinetic Arrest of Front Transformation to Gain Access to the Bulk Glass Transition in Ultrathin Films of Vapour-Deposited Glasses*, *Physical Chemistry Chemical Physics* **20**, 29989 (2018).
- [19] *Internal Database of the Dresden Integrated Center for Applied Physics and Photonic Materials (IAPP)*.

Chapter 4

Access to bulk transformation in thin film vapor-deposited glasses

While experiments and glass theories conclude that liquid cooled glasses transform into the supercooled liquid via a cooperative relaxation process that takes place simultaneously across the volume of the sample [1,2], thin film highly stable glasses transform via the formation of an equilibrated liquid parallel front that initiates at the surface and propagates consuming the glass [3–5]. The increased density and tight molecular packing of stable glasses has been proposed as the responsible for the transformation process to start in regions of the sample where the mobility is higher, i.e. free surfaces and interfaces [6]. The front transformation mechanism is not exclusive to highly stable glasses, in fact, it has been seen that vapor-deposited glasses with lower stabilities also start the transformation into the supercooled liquid via growth fronts [7,8], which dominate the transition until the bulk mechanism is triggered. However, the lower the stability of the glass, the shorter the distance the front travels before the bulk transformation is active [5]. This characteristic distance has been identified as the crossover length. Although this type of mechanism via growth fronts has been difficult to detect in low stability glasses, the propagating fronts have been directly measured for TPD and IMC glasses of different stabilities using spectroscopic ellipsometry [8,9] and Rodríguez-Tinoco *et al.* used fast-scanning nanocalorimetry to study the front transformation in IMC glasses spanning a broad range of stabilities [7].

Thus, to access the bulk transformation in all type of glasses, it will be necessary to avoid the formation of the liquid front, not only in ultrastable glasses, but also in glasses of

lower stability. In this chapter we present, in first place, the methodology to identify the front transformation in thin film vapor-deposited glasses. We proceed by showing how it is possible to avoid the formation of this propagating front by capping the different surfaces of our samples with a material with lower mobility. Finally, we show this strategy works regardless of the stability of the glass, making it possible to study the bulk transformation in all type of vapor-deposited glasses.

4.1 Identification of the transformation mechanism

Using fast scanning nanocalorimetry, the existence of a propagating front can be inferred from the heat capacity data, C_p , using an appropriate data treatment. Figure 4.1 shows the specific heat as a function of temperature for thin film TPD glasses with different thicknesses obtained from two different routes: vapor deposited at 264K ($0.79T_g$) (Figure 4.1a) and fast cooled from the liquid phase (Figure 4.1c).

The data in Figure 4.1a shows a clear shift of the devitrification onset towards higher temperatures for thicker films. This behavior is characteristic of a front mediated transformation mechanism [10]. Specific heat data is usually obtained by dividing the heat capacity trace by the total mass of the sample (mass normalization). When measuring a transition that takes place simultaneously in the whole volume of the sample and the transformed volume is proportional to the total volume, this normalization yields curves that overlap regardless of their size, as it can be seen in Figure 4.1c for a liquid cooled glass. However, the transformed volume in a transition that takes place via a parallel front that initiates at the surface and propagates consuming the glass is proportional to the surface of the sample and not to the total volume. Therefore, normalizing by the total mass results in a shift to lower temperatures of the transition peak for thinner films as long as the samples have the same surface (as it can be seen in Figure 4.1a).

To further confirm the transformation of the glasses showed in Figure 4.1a takes place via a front mechanism, we can proceed with a normalization of the C_p data that takes into account the surface and thickness of the films. The starting point is to consider that the heat capacity, $C_p^{exp}(T)$, can be decomposed into three different terms as shown in Equation 4.1: the first term corresponds to the heat capacity contribution of the liquid, the second term to the contribution of the glass and the last one to the transformation rate,

$$C_p^{exp}(T) = m_0 \left(x_l(T)c_{sp}^l + (1 - x_l(T))c_{sp}^g + \Delta h \frac{dx_l(T)}{dT} \right) \quad (4.1)$$

where c_{sp}^g and c_{sp}^l are the specific heat of the glass and supercooled liquid, respectively [11], m_0 is the total mass of the sample, Δh refers to the excess enthalpy involved in the transformation and x_l is the volume fraction of glass that has already transformed into supercooled liquid. This last parameter is time/temperature dependent and ranges from 0 (sample in glass state) to 1 (sample completely transformed into SCL).

Assuming a situation where the sample is transforming exclusively by a transformation front that advances independently of the film thickness, we can apply the following changes:

- i. $m_0 = d_0 A \rho$, where A is the surface area, d_0 the total thickness of the sample and ρ is the density of the material (in the supercooled liquid state).
- ii. $x_l = \frac{d_l}{d_0}$, where d_l is the thickness of the glass that has already transformed into supercooled liquid.

Therefore, $C_p^{exp}(T)$ can be renormalized as follows [7]:

$$C_p^{norm}(T) = \frac{C_p^{exp}(T)}{\rho A} - c_{sp}^l d_0 = d_l(T)(c_{sp}^l - c_{sp}^g) + \Delta h \frac{d(d_l(T))}{dT} \quad (4.2)$$

With this normalization, at the right side of Equation 4.2 we have only d_l as time/temperature dependent variable. Since the evolution of the front should be independent of the thickness of the film, we should observe an overlap of all the normalized calorimetric curves. Figure 4.1b shows the heat capacity traces presented in Figure 4.1a but normalized according to Equation 4.2, i.e., by the thickness and surface of the films. Using this normalization, the onsets of the calorimetric traces of the different samples overlap into a single curve regardless of their thickness. This superposition confirms the fact that this transition indeed scales with the surface of the film and not throughout the sample's volume and, therefore, it is compatible with a transformation dominated by the evolution of parallel growth fronts.

On the other hand, for liquid cooled glasses we observe the opposite behavior. While surface normalization results in curves that present different onset temperatures (Figure 4.1d), the mass normalization of the heat capacity data produces the collapse of all curves

in a single master curve (Figure 4.1c) regardless of their thickness. This superposition of the mass normalized curves is characteristic of systems that transform homogeneously throughout the volume's sample and in which the transformed fraction per unit time is independent of the total mass (or volume), as typically found in liquid cooled glasses. Therefore, normalizing the heat capacity data by the total mass of the sample or the sample's surface (with Equation 4.2) has shown to be a useful method to distinguish homogeneous transformation processes from transformations dominated by propagating growth fronts.

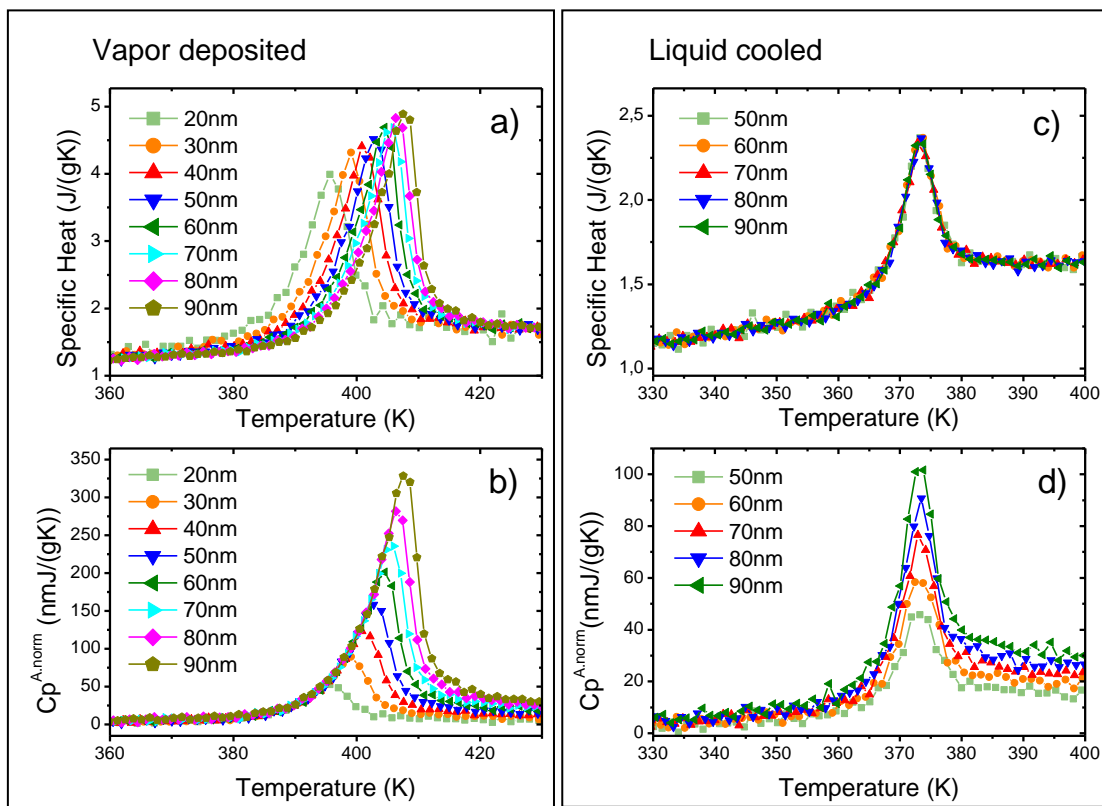


Figure 4. 1. Heat capacity curves as a function of temperature of TPD samples with thicknesses ranging from 20nm to 90nm obtained by nanocalorimetry which have been normalized by total mass (a and c) or using Equation 4.2 (b and d). Figures a and b correspond to a glass deposited at $0.79T_g$ and figures c and d correspond to a liquid cooled glass at ~ 500 K/s.

It is worth noticing that using this method, we cannot distinguish between the existence of a single front (initiated at the free surface) or the existence of two fronts (one surface-initiated and another interface-initiated) in contrast with other experimental techniques

(such SIMS [6]). Using nanocalorimetry, the existence of one or two growth fronts can be determined using capping layers as we will see in the following section.

4.2 Suppressing the front transformation

The transformation mechanism into the supercooled liquid via growth fronts in vapor-deposited glasses has been attributed to the higher molecular mobility at the free surfaces and/or interfaces of the films, in contrast with the tight molecular packing found in the material's bulk [12]. In this scenario, one might think that by removing these highly mobile regions, it should be possible to delay the transformation process by stopping the growth fronts from appearing, gaining access, in this way, to the bulk transformation mechanism in vapor-deposited glasses.

This approach was already used by Sepúlveda *et al.* [13]. They showed, by means of secondary ion mass spectroscopy (SIMS), that capping the free surface of indomethacin layers with a material that has a higher glass transition temperature (in their case α,α,β -TNB) stops the formation of the growth front. Using this strategy, they were able to increase the sample's kinetic stability by delaying the transformation into the supercooled liquid of the capped indomethacin layers.

Following an analogous reasoning, for our study we cap TPD ($T_g=333\text{K}$) thin film glasses with TCTA, a molecule with glass transition at $T_g=424\text{ K}$, that is 91K above the glass transition temperature of TPD. Since molecular mobility in glassy systems decreases drastically below T_g (see Section 1.2), at the temperature range where TPD glasses could acquire enough mobility to start transforming by propagating fronts, the TCTA layers will still be found in a deeply glassy state (around 100K below their T_g) with very limited mobility.

Two film configurations are used in order to evaluate the effect that capping has on the transformation dynamics of thin film glasses of TPD: i) TPD single layers (used mainly for comparison with the capped ones) and ii) capped TPD thin films with a layer of TCTA on both the free surface and the interface with the substrate (see Figure 4.2).

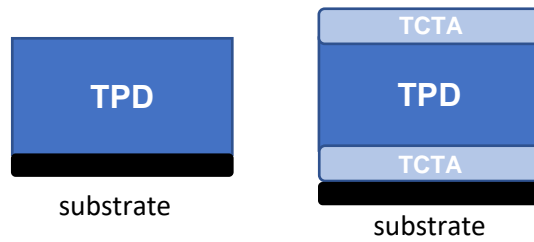


Figure 4. 2. Sketch of the two main configurations used to study the suppression of growth fronts in TPD thin films using the organic semiconductor TCTA as the capping material. TPD films range from 20 to 70 nm in thickness while TCTA layers have thicknesses ranging from 10 to 20 nm.

For both configurations, single TPD layers and capped samples, three different thicknesses of TPD (around 20, 40 and 70nm) have been deposited at a substrate temperature of 285K, temperature at which we obtain the ultrastable glass (UG) for this system ($0.85T_g$). TCTA layers have, in all cases, thicknesses that range between 10nm and 20nm and are deposited at the same temperature as the TPD.

Figure 4.3 shows the calorimetric scans corresponding to the three different thicknesses of TPD glasses in the two different configurations described in Figure 4.2. Note that in Figure 4.3, the heat capacity contribution of the TCTA glass layers is subtracted from each calorimetric curve in order to simplify the comparison between the capped and single layers of TPD. It is important to remark that only the glass contribution is subtracted to the total heat capacity curve, not the enthalpy of transformation nor the liquid contribution. That is the reason why in the calorimetric traces of samples that contain TCTA its devitrification peak is always present (as can be seen in Figure 4.4b at around 440K). The TCTA glass contribution to C_p can be directly inferred from the specific heat of the TCTA glass, c_{sp}^g , (obtained from single TCTA layers) and the mass of each of the layers, measured precisely with the QCM. A more detailed explanation of this procedure can be found elsewhere [14].

Comparing the single TPD (open symbols) and capped samples (solid symbols) in Figure 4.3, we can distinguish two different scenarios: i) TPD single layers show a shift of their devitrification onset temperature with thickness in the mass-normalized specific heat, characteristic of samples that transform via growth fronts; ii) For the capped TPD films,

however we obtain devitrification peaks that collapse regardless of the sample's thickness, showcasing the typical trace of a bulk transformation.

The capping strategy is also effective with glasses of lower stability. Figure 4.4a and 4.4b show the specific heat curves corresponding to TPD samples (single and capped layers) deposited at 250K ($0.75T_g$) and 325K ($0.98T_g$), respectively. As it can be seen, equivalent results as the ones observed for ultrastable glasses are obtained: while the non-capped TPD glasses show calorimetric traces typical of heterogeneous front transformation (Figure 4.4a and 4.4b open symbols), all the capped samples collapse into a single curve (Figure 4.4a and 4.4b filled symbols). Confirming, therefore, that we are able to avoid the formation of parallel fronts and access the bulk transformation mechanism not only in the case of the ultrastable glass but also for less stable glasses.

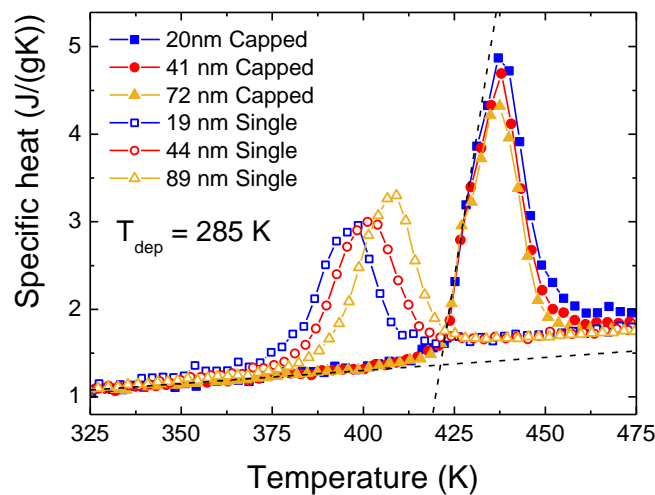


Figure 4. 3. Specific heat as a function of temperature of TPD ultrastable glasses deposited at 285K for single layers (open symbols) and capped samples (filled symbols). Different colors and symbols refer to different thicknesses as described in the legend and the dashed lines mark the onset temperature of the capped layers. The small variations in the area of the peaks for the capped samples are an artefact produced by the different TPD/TCTA mass ratios in each sample, which are not considered by the normalization.

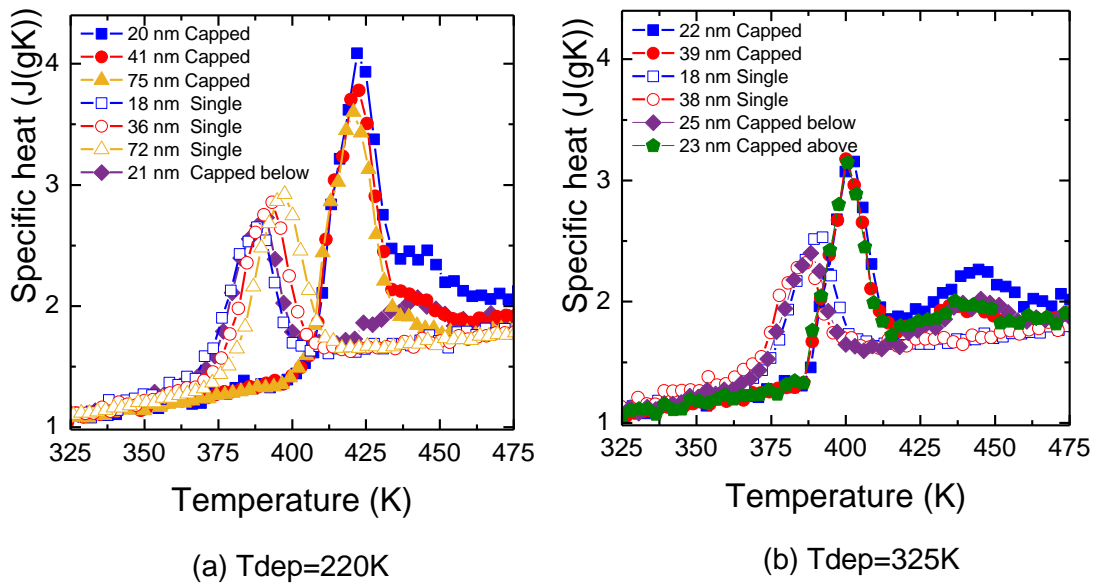


Figure 4.4. Specific heat as a function of temperature of TPD films deposited at (a) 250K ($0.75T_g$) and (b) 325K ($0.98T_g$) for single layers (open symbols) and capped films (filled symbols). The purple and green curves in (b) correspond to the calorimetric trace of bilayers of TPD and TCTA with the configuration substrate/TCTA/TPD and substrate/TPD/TCTA, respectively. The feature at high temperature (around 440K-445K) corresponds to the devitrification of the TCTA layers.

This capping strategy is also useful to identify with calorimetry if the transformation into the supercooled liquid takes place via one or two growth fronts. Capping only with a TCTA layer the interface between the TPD and the substrate, we obtain a calorimetric trace identical to the ones obtained for single TPD layers (Figure 4.4b purple curve). However, capping only the free surface and depositing the TPD directly on top of the substrate yields curves that overlap with totally capped films (Figure 4.4b green curve). This is a clear indication that in our TPD films, the devitrification process is dominated by a single surface-initiated growth front, at least when measuring with nanocalorimetry. Finally, it is worth mentioning that in order to ensure the total suppression of the growth front, we performed a study capping a 50nm TPD thin film with TCTA layers of different thicknesses. As it can be observed in Figure 4.5, for samples with TCTA layers thicker than 8nm all curves overlap, indicating that we need at least layers 8nm thick of TCTA in order to completely block the propagating fronts.

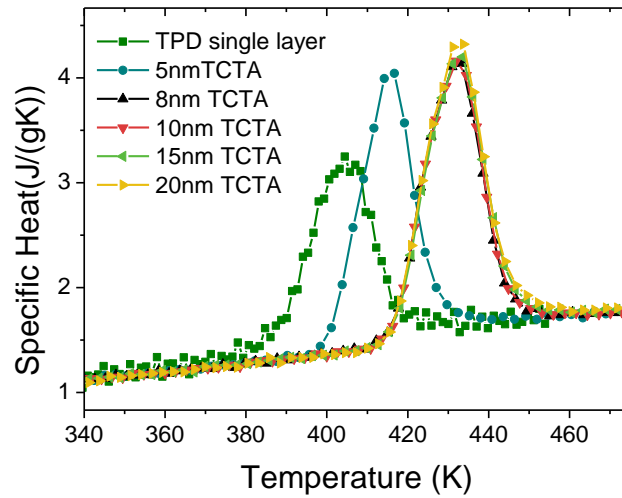


Figure 4. 5. Calorimetric trace of TPD glasses capped with TCTA layers of different thicknesses. A TPD single layer is also deposited in order to compare it with the capped ones. All samples are grown at 285K.

4.3 Summary

We have seen how the transformation of stable thin film vapor-deposited glasses into the supercooled liquid state proceeds via a parallel front that starts at the surface of the sample. This transformation mechanism can be easily inferred from the calorimetric data using an *ad-hoc* surface normalization, which considers the surface and thickness of the films instead of their total mass.

In addition, we studied a capping strategy which has shown to be a useful method to effectively suppress the formation of liquid growth fronts. In this way, we gain access to the bulk devitrification of thin film glasses, not only for ultrastable glasses but also for samples with different stabilities.

References

- [1] A. Cavagna, *Supercooled Liquids for Pedestrians*, Phys Rep **476**, 51 (2009).
- [2] V. Lubchenko and P. G. Wolynes, *Theory of Structural Glasses and Supercooled Liquids*, Annual Review of Physical Chemistry.
- [3] S. F. Swallen, K. L. Kearns, S. Satija, K. Traynor, R. J. McMahon, and M. D. Ediger, *Molecular View of the Isothermal Transformation of a Stable Glass to a Liquid*, J Chem Phys **128**, 214514 (2008).
- [4] D. M. Walters, R. Richert, and M. D. Ediger, *Thermal Stability of Vapor-Deposited Stable Glasses of an Organic Semiconductor*, J Chem Phys **142**, 134504 (2015).
- [5] J. Ràfols-Ribé, M. Gonzalez-Silveira, C. Rodríguez-Tinoco, and J. Rodríguez-Viejo, *The Role of Thermodynamic Stability in the Characteristics of the Devitrification Front of Vapour-Deposited Glasses of Toluene*, Phys. Chem. Chem. Phys **19**, 11089 (2017).
- [6] A. Sepúlveda, S. F. Swallen, L. A. Kopff, R. J. McMahon, and M. D. Ediger, *Stable Glasses of Indomethacin and α,α,β -Tris-Naphthylbenzene Transform into Ordinary Supercooled Liquids*, J Chem Phys **137**, 204508 (2012).
- [7] C. Rodríguez-Tinoco, M. Gonzalez-Silveira, J. Ràfols-Ribé, A. F. Lopeandía, and J. Rodríguez-Viejo, *Transformation Kinetics of Vapor-Deposited Thin Film Organic Glasses: The Role of Stability and Molecular Packing Anisotropy*, Physical Chemistry Chemical Physics **17**, 31195 (2015).
- [8] S. S. Dalal and M. D. Ediger, *Influence of Substrate Temperature on the Transformation Front Velocities That Determine Thermal Stability of Vapor-Deposited Glasses*, J Phys Chem B **119**, 3875 (2015).
- [9] S. S. Dalal, D. M. Walters, I. Lyubimov, J. J. de Pablo, and M. D. Ediger, *Tunable Molecular Orientation and Elevated Thermal Stability of Vapor-Deposited Organic Semiconductors*, Proceedings of the National Academy of Sciences **112**, 4227 (2015).
- [10] C. Rodríguez-Tinoco, M. Gonzalez-Silveira, J. Ràfols-Ribé, A. F. Lopeandía, M. T. Clavaguera-Mora, and J. Rodríguez-Viejo, *Evaluation of Growth Front Velocity in Ultrastable Glasses of Indomethacin over a Wide Temperature Interval*, J Phys Chem B **118**, 10795 (2014).
- [11] S. L. Shamblin, X. Tang, L. Chang, B. C. Hancock, and M. J. Pikal, *Characterization of the Time Scales of Molecular Motion in Pharmaceutically Important Glasses*, J Phys Chem B **103**, 4113 (1999).
- [12] L. Zhu, C. W. Brian, S. F. Swallen, P. T. Straus, M. D. Ediger, and L. Yu, *Surface Self-Diffusion of an Organic Glass*, Phys Rev Lett **106**, 256103 (2011).
- [13] A. Sepúlveda, S. F. Swallen, and M. D. Ediger, *Manipulating the Properties of Stable Organic Glasses Using Kinetic Facilitation*, J Chem Phys **138**, 12A517 (2013).
- [14] J. Ràfols-Ribé, A. Vila-Costa, C. Rodríguez-Tinoco, A. F. Lopeandía, J. Rodríguez-Viejo, and M. Gonzalez-Silveira, *Kinetic Arrest of Front Transformation to Gain Access to the Bulk Glass Transition in Ultrathin Films of Vapour-Deposited Glasses*, Physical Chemistry Chemical Physics **20**, 29989 (2018).

Chapter 5

Bulk glass transition in ultrastable glasses

The first and only experimental work addressing the bulk transformation of stable glasses, before our present study, used alternating current nanocalorimetry to measure the reversing heat capacity of stable indomethacin very thick films (up to $30\mu\text{m}$) as they transformed into the supercooled liquid [1]. The films were much thicker than the crossover length ($\sim 1\mu\text{m}$), so the bulk transformation mechanism dominated the transition [2–4]. In this work, it was reported that the transformation kinetics of the almost-bulk samples could reasonably be fit using the Avrami formalism [5–8] with an Avrami exponent $n\sim 4$, which was consistent with a transition into the supercooled liquid via the homogeneous nucleation and growth of three-dimensional liquid “bubbles”. This same perspective has also been discussed in several theoretical and simulation works in which it is proposed that the bulk transformation can be triggered by regions with higher mobility, which may act as nucleation sites from where the liquid grows in a similar manner as it does from the surface in non-capped films [9–13]. In this sense, Gutiérrez and Garrahan used local excitations to initiate the transition in a kinetically constrained model to recreate the bulk transformation in stable glasses [10]. Wolyness and coworkers [11], in the RFOT framework, consider the formation of entropy drops in the glass that fully relax into the liquid and then propagate the relaxation into adjacent regions. Also in more recent works, the swap methodology [14] has enabled the production of in-silico glasses with stabilities comparable to vapor deposited ultrastable

glasses [15,16]. The transition of these simulated glasses into the liquid phase has seen to take place via moving fronts (resembling a melting process) and if made thick enough, a competing transformation between bulk and front or only a bulk process is observed [13].

In the previous chapter we have seen how the emergence of liquid growth fronts in vapor-deposited glasses can be effectively suppressed experimentally by arresting the mobility of the free surface and interface with the substrate. This can be achieved by capping the sample with a higher T_g material [17]. If the front is suppressed, instead of the characteristic heterogeneous transformation via growth fronts [3,18,19], the transformation in highly stable glasses is expected to occur mainly in the bulk of the material [1,20]. The capping strategy, therefore, grants us access to the bulk transformation mechanism in thin film highly stable glasses, without the need of working with very thick films.

In this chapter, we study the bulk-like transformation into the supercooled liquid of highly stable glasses of TPD grown from the vapor at $0.85T_g$ during isothermal annealing at temperatures ranging from $T_g+14\text{K}$ to $T_g+34\text{K}$. For this study, we use mainly fast-scanning nanocalorimetry (taking advantage of the fast heating/cooling rates) to investigate the amount of glass that transforms into SCL as a function of time. The heat capacity trace signature of partially transformed glasses will help in the identification of the transformation mechanisms into the liquid phase.

5.1 Sample preparation and thermal protocol

For this study, we will mainly use samples grown in the three-layer configuration stack (TCTA-TPD-TCTA) as depicted in Figure 4.2. Both TPD films (85 nm thick) and TCTA capping layers (13 nm thick) are grown at a deposition rate of 0.08nm/s and at a deposition temperature of 285 K, temperature that corresponds to the formation of highly stable glasses in TPD ($0.85T_g$). Once this three-layer stack is grown onto the Al plate of our calorimetric chip, we isothermally anneal it for various times (from 130 min to 15 s) at temperatures ranging from $T_g+14\text{K}$ (347 K) to $T_g+34\text{K}$ (367 K). After the annealing, the sample is passively cooled at around 500 K/s down to $T = 200\text{ K}$. Next, a temperature scan is immediately performed at a heating rate of $3.5 \times 10^4\text{ K/s}$ up to a temperature well above the onset of devitrification of the stable glass. Figure 5.1 shows a schematic of the

thermal protocol followed from the deposition process until the measurement of the specific heat trace.

For comparison, we also analyze the bulk transformation of 35 μm thick TPD films deposited under similar conditions as the thinner layers, with the only difference that thick samples are not capped with TCTA films. Calorimetric measurements for thick samples are conducted on glasses annealed at $T_g+14\text{K}$ using heating/cooling rates of 10 K/min in a Perkin-Elmer DSC. These samples are grown on top of Al substrates, which are subsequently introduced in the pans for the DSC measurements (details can be found in Section 3.3.2).

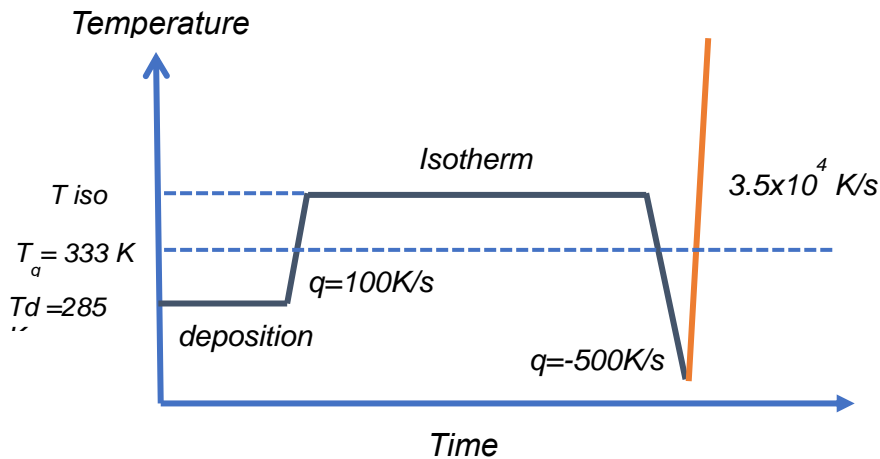


Figure 5. 1. Schematics of the temperature profile followed by the samples from the deposition stage to the final calorimetric scan. The samples are grown in the TCTA/TPD/TCTA configuration at 285 K on top of the nanocalorimeter sensing area. Right after the deposition they are heated above T_g for a certain annealing time and quenched down to base temperature (200 K). Immediately afterwards, the calorimetric scan is performed. The specific heat traces presented in the following sections correspond in all cases to this last calorimetric scan, from which information regarding the transformation of the glass into the liquid during the isotherm can be extracted.

5.2 Glass transition in capped thin film ultrastable glasses

Figure 5.2a shows the specific heat traces for capped TPD thin films after annealing them at $T_g+29\text{K}$ for times up to 65s. The black continuous curve represents the specific heat obtained during a temperature scan of the as-deposited stack. This curve presents only one large overshoot with peak temperature $T_{peak}^{SG} \approx 428\text{K}$, which corresponds to the

devitrification of the stable TPD glass (SG). The light green curve, on the other hand, corresponds to a sample fully transformed after an isotherm at $T_g+29\text{K}$ for 65s. The endothermic peak at low temperature ($T_{peak}^{FC} \approx 372\text{ K}$) is characteristic of the glass transition of a glass with very low stability and it originates from the complete devitrification of the TPD glass during the isotherm which is subsequently fast cooled from the liquid state (FC glass). The broad feature at higher temperature (around 430 K) is the glass transition of the TCTA layers which have not transformed yet during the isothermal annealing. The heat capacity traces of samples annealed at intermediate times ($0 < t < t_{trans}$) show two main features: i) the appearance of an endothermic peak at lower temperatures, which fits in temperature with the transition of a FC glass, is a clear indication that some equilibrated liquid is formed during the annealing, becoming a FC glass due to subsequent fast cooling. The area increase of this peak over isotherm time denotes that the longer the annealing time, the higher the amount of glass that has transformed into the liquid phase. ii) A continuous decrease of the area and a shift towards lower temperatures of the large endotherm associated with the devitrification of the stable glass, indicative of a loss in stability. These two features reveal that the bulk transformation of the stable glass proceeds via two parallel competing processes: on one hand, the transformation of part of the glass into the equilibrated super cooled liquid (SCL) which upon cooling forms a FC glass and, on the other hand, the partial rejuvenation or softening of the non-transformed stable glass, that is, the remaining stable glass loses stability continuously as time increases when annealed above its fictive temperature ($T_f=292\text{K}$ for these TPD thin film glasses).

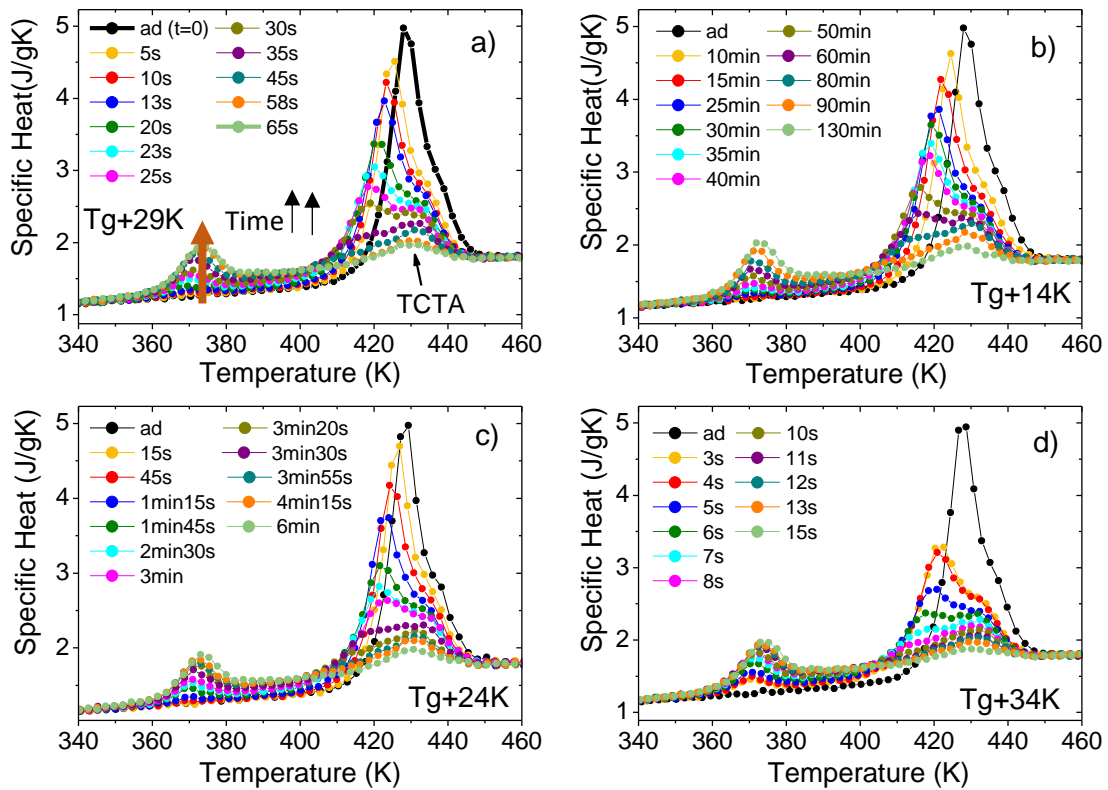


Figure 5. 2. Specific heat as a function of temperature for capped TPD thin film glasses grown at $T_{dep}=285\text{K}$ which have been submitted to isothermal treatments at a) $T_g+29\text{K}$, b) $T_g+14\text{K}$, c) $T_g+24\text{K}$ and d) $T_g+34\text{K}$ for different annealing times (see legend). Black curves correspond to the calorimetric trace of an as-deposited sample. Light green curves represent the glass transition of a capped TPD glass totally transformed into the supercooled liquid during the annealing.

Equivalent measurements were performed for identical glasses at three other annealing temperatures ($T_g+14\text{K}$, $T_g+24\text{K}$ and $T_g+34\text{K}$) with similar results. In Figure 5.2. we can observe that all the calorimetric traces present the two characteristic endothermic peaks (corresponding to the glass transitions of the fast-cooled glass and the remaining stable TPD glass), as well as a shift to lower temperatures of the second peak due to a softening of the more stable glass, regardless of the annealing temperature. The total transformation time, however, is significantly reduced as we increase the annealing temperature, ranging from around 3h for the isotherm at $T_g+14\text{K}$ to barely 15s at $T_g+34\text{K}$.

In the following sections we will analyze in more detail the processes behind the observed features.

5.2.1 Liquid formation during the isotherm

In order to study the formation of equilibrated liquid during the isotherms, we analyze the evolution of the FC peak as function of time for each annealing temperature. From this calorimetric peak, we can evaluate the fraction of glass that has transformed into the liquid phase during the previous isotherm and has become FC glass upon fast cooling using two different methods. Prior to the analysis of the heat capacity data, the heat capacity contribution of the glassy TCTA capping layers is subtracted as indicated in Section 4.2.

In the first case, the SCL transformed fraction, f , can be evaluated directly from the specific heat value at a temperature in between the FC and the stable glass endothermic peaks (around 388K for T_g+29K). We can assume that the specific heat is additive and, therefore, the specific heat values in this region, c_{sp}^{exp} , correspond to the linear sum of two contributions: the specific heat of the liquid TPD that was formed during the isotherm and has already transformed after the first calorimetric peak, c_{sp}^l , plus the specific heat of the remaining TPD stable glass, c_{sp}^g , multiplied by their respective fractions (or masses). This can be numerically written as:

$$c_{sp}^{exp}(372K < T < 428K) = c_{sp}^l f + c_{sp}^g(1 - f) \quad (5.1)$$

In a totally transformed sample $c_{sp}^{exp} = c_{sp}^l$ and therefore, $f = 1$ while, for the as-deposited glass, we will find that there is no liquid contribution, thus we obtain a transformed fraction $f = 0$. All the other curves corresponding to intermediate times will lay between these two values (see Figure 5.3), allowing us to determine the transformed fraction for each annealing time.

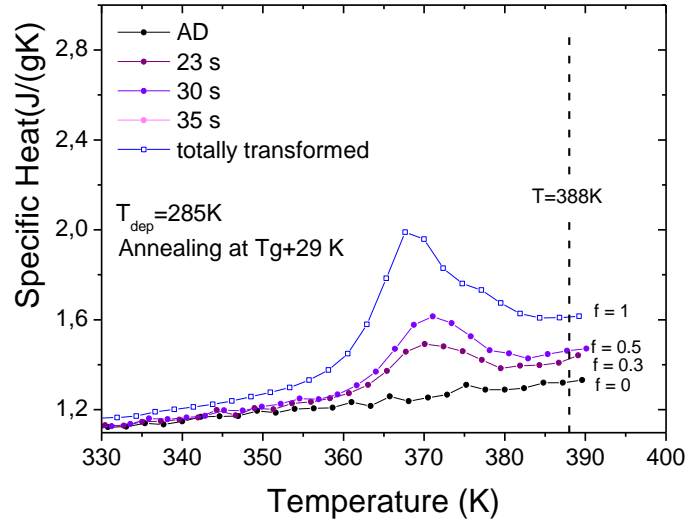


Figure 5. 3. Specific heat vs temperature obtained at a heating rate of $3,5 \times 10^4$ K/s of ultrastable capped TPD glasses after different annealing times at T_g+29 K (see legend). The transformed fraction has been extracted from the specific heat curves by assuming that the specific heat trace at around 388K is the result of the addition of the specific heat of liquid TPD plus the specific heat of the remaining TPD glass at that temperature, weighted by the corresponding fraction.

On the other hand, the SCL transformed fraction can also be determined from the heat capacity data by fitting the experimental specific heat curves, c_{sp}^{exp} , to an equation that considers the full calorimetric curve for each temperature scan. In a similar manner as in Equation 4.1, which decomposed the specific heat data of a glass transition in three terms: contribution of the liquid, contribution of the glass and transformation rate, we can define an expression that includes the three different devitrification peaks in our C_p data (Equation 5.2). This way, we obtain an equation with three different terms (contribution of the liquid, glass and transformation rate) that take into account three different phase transitions: the fast-cooled TPD glass (at low temperatures, around 375 K), the initial stable glass which has been subject to softening (between 415 K and 430 K) and the TCTA glass (at higher temperatures, around 430 K).

$$c_{sp}^{exp}(T) = c_{sp}^l (X_{FC}f + X_{SG}(1-f)) + c_{sp}^g (1 - X_{FC}f + X_{SG}(1-f)) + \Delta h_{FC}f \frac{dX_{FC}}{dT} + \Delta h_{SG}(1-f) \frac{dX_{SG}}{dT} + B \quad (5.2)$$

Where c_{sp}^l is the specific heat of the liquid TPD, c_{sp}^g is the specific heat of the glass TPD, f the SCL transformed fraction, Δh_{FC} and Δh_{SG} the excess enthalpy per unit mass of the

TPD glass transformed into liquid during the isothermal treatment (first glass transition peak in the calorimetric curves) and the yet not transformed TPD stable glass (second glass transition peak), respectively. X_{FC} and X_{SG} are Boltzmann like functions which describe the transformation from glass to liquid and range from 0 (for the glass) to 1 (for the liquid state) and depend on parameters that can be fitted from the shape and position of the peaks. Finally, B is a constant that includes the TCTA glass transition and the liquid contribution to the specific heat curves.

Considering that c_{sp}^l and c_{sp}^g are known expressions, that the FC glass is the same for the different annealing times at a certain annealing temperature (same ΔT) and that the TCTA does not change during the isotherm, the only unknown parameters in Equation 5.2 are the excess enthalpy of the stable glass, which changes due to the loss of stability with annealing time, and the transformed liquid fraction, f (parameter that we are interested in calculating). Fitting Equation 5.2 to the experimental data we can obtain these fitting parameters for each of the samples.

Figure 5.4 shows the experimental data together with one of the fittings obtained for a glass deposited at 285K ($0.85T_g$) and annealed at $T_g + 14K$ during 4200s. As it can be seen, this corresponds to a glass that transformed into the liquid phase a 54% during the isotherm. The results obtained using this method differ in average around a 4% compared with the first method explained. Therefore, since both methods yield comparable results, both of them will be used indistinctly during the development of this thesis.

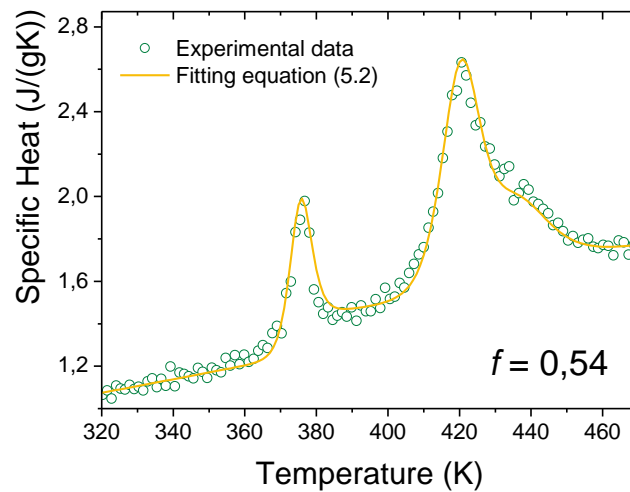


Figure 5. 4. Experimental specific heat as a function of temperature of a sample deposited at 285K and annealed at $T_g + 29K$ for 4200s during a calorimetric scan at $3 \cdot 10^4$ K/s (green open symbols) together with the fitting obtained using Equation 5.2. The fraction of SCL corresponds to 0.54 in this case.

The estimated transformed fractions, f , of the capped TPD glasses annealed at $T_g+14\text{K}$, $T_g+24\text{K}$, $T_g+29\text{K}$ and $T_g+34\text{K}$ are plotted in Figure 5.5a. The data have a sigmoidal shape as typically observed for transformations following nucleation and growth like kinetics [21]. Normalizing the data by the time required for each sample to totally transform into the supercooled liquid, t_{trans} , we find that all curves collapse into a single master curve (Figure 5.5b), indicating that these ultrastable glasses transform into the SCL following the same dynamics with a temperature dependence that scales with the inverse of the time. A thorough discussion on the dynamics of liquid formation is presented in Section 5.4.

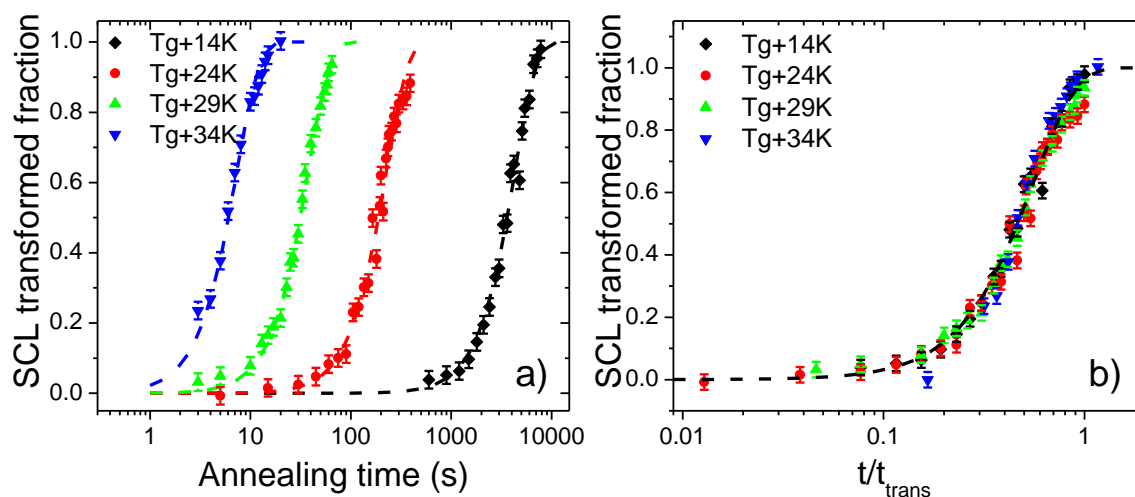


Figure 5.5. (a) Fraction of liquid in ultrastable capped TPD glasses as a function of time for four different isotherm annealing temperatures: T_g+14 , T_g+24 , T_g+29 and $T_g+34\text{K}$ where $T_g=333\text{K}$. (b) Master curve of the liquid transformed fraction obtained normalizing the annealing time by the time needed for the sample to be fully transformed into SCL. The total overlap of the curves indicates that the transformation dynamics are the same for the different annealing temperatures with a dependence on temperature that scales with the inverse of time. The dashed lines are KJMAE fittings imposing $n = 2$.

5.2.2 Softening of the stable glass

Aside from the formation of liquid during the isotherm, which we can distinguish by the appearance of a devitrification peak at low temperatures (FC glass) in the heat capacity curves, in Figure 5.2 we can also see how the glass transition peak corresponding to the remaining stable glass (feature at higher temperature) changes as a function of annealing time. In particular, a shift to lower temperatures together with a broadening and area reduction of the stable endothermic peak can be observed. This evolution is characteristic

of a softening process, where the glass progressively loses stability. Even though the area reduction is partially related to the thermodynamic stability loss, it is also related to the fact that for longer annealing times the amount of stable glass in the sample is reduced at the expense of the formation of the liquid phase (the longer annealing times, the higher the fraction of stable glass transformed into the liquid state). Yet, the temperature shift is a distinct indicator that the glass is indeed losing stability during the annealing treatment. The broadening of the peak, on the other side, indicates an increase of the dispersion of the relaxation times in the glass for longer times, suggesting that the softening process is not completely homogeneous. The evolution of the remaining stable glass during the isotherm, therefore, can be analyzed monitoring the shift of the stable devitrification peak. Figure 5.6 shows the SCL transformed fraction and the temperature shift of the T_{peak} of the stable glass (T_{peak}^{SG}) for a sample annealed at T_g+29K . A comparison between the time evolution of the two mechanisms, softening and liquid formation and growth, exposes their relative importance. The amount of formed liquid is monitored via the transformed fraction, x_l . The degree of softening is monitored via the ratio $\Delta T(t)^{soft} = \Delta T(t) / \Delta T_{trans}$, where $\Delta T(t)$ is the shift of the devitrification peak with respect to the initial position, and $\Delta T_{trans} = T_{peak}^{SG}(AD) - T_{peak}^{FC}$ is the maximum possible variation of the devitrification peak by softening. Taking $t_{ann} = 40s$ as an example, $x_l=75\%$ and $\Delta T(t)^{soft} = 27\%$, indicating that the softening is a much slower process compared with the transformation of the glass into SCL via the formation and growth of liquid regions. In other words, the untransformed stable glass is still a very stable glass up to its complete transformation into the liquid. Note that the position of the peak seems to stop evolving at around $t=35s$ (see Figure 5.6). This does not mean that the stable glass stops evolving. Actually, the peak continues broadening, but the shift is subtle and it cannot be measured properly. This softening will be further studied in Chapter 7, where the bulk transformation will be analyzed for glasses of different stabilities.

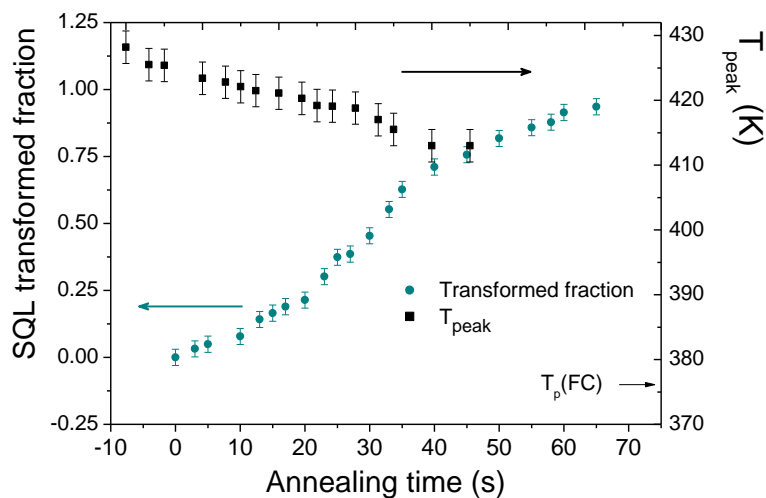


Figure 5. 6. Calculated transformed fraction (left axis, blue solid circles) and peak temperature of the stable TPD glass (right axis, black solid squares) as a function of annealing time for capped TPD samples deposited at 285K and annealed at T_g+29 K. The peak temperature after $t=35$ s seems to stop evolving and the data for longer annealing times has been removed from the plot. This apparent stop can be attributed to the broadening of the stable peak after a certain annealing time, which makes difficult properly assigning a value to T_{peak} from there onwards. More details on the study of the softening of stable glasses can be found in Chapter 7.

5.3 Glass transition in UG thick films

With the objective of comparing if the bulk transformation mechanism differs in thin films and thick samples, we grow TPD films of around $35\mu\text{m}$ thick under similar conditions as the thinner layers ($T_{dep}=285\text{K}$ and deposition rate 0.08nm/s), but without the TCTA layers at the bottom and top of the film. In this case, only annealing treatments at $T_g+14\text{K}$ were performed. The calorimetric measurements of the bulk sample are conducted using conventional DSC as indicated in Section 3.3.3 and the resulting calorimetric traces are shown in Figure 5.7.

The specific heat curves in Figure 5.7, show the same characteristics as the already seen for thin film glasses: transformation of part of the stable glass into the SCL that upon cooling forms a FC glass (lower temperature peak, $T_{peak} \cong 340\text{K}$) and the partial rejuvenation of the non-transformed stable glass, as it can be seen by the shift to lower temperatures of the high temperature glass transition peak. In this case, since the sample is not capped with TCTA, in parallel to the bulk transformation, part of the sample will also transform via growth fronts that start in the highly mobile surfaces.

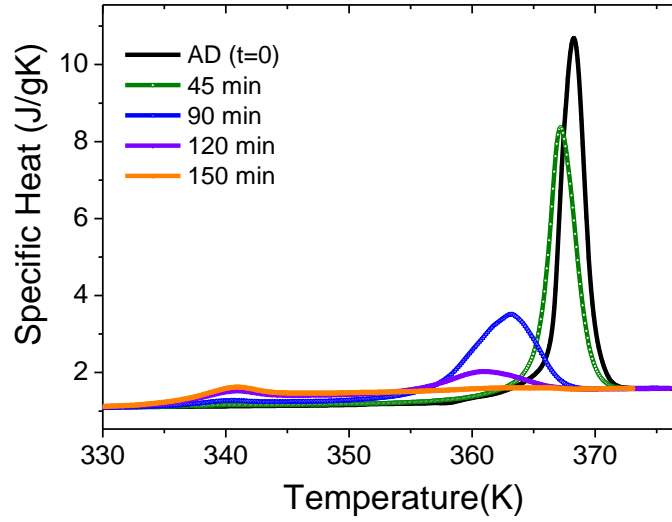


Figure 5. 7. Specific heat trace as a function of temperature during a heating ramp at 10 K/min of 35 μ m thick film glasses of TPD deposited at 285 K after isothermal treatments at T_g+14 K for different annealing times (indicated in the legend).

Since we are only interested in the transformed fraction that corresponds to the bulk process, the fraction transformed by the propagating front needs to be subtracted when calculating the bulk transformed fraction. The quantity of sample transformed by front at a certain temperature and during a certain time can be estimated from previous data of the front velocity [19]. Assuming we have a single front that moves at a constant rate, the transformed fraction due to front propagation can be calculated as:

$$x_l^{front} = \frac{v_f(T)t_{ann}}{d_0} \quad (5.3)$$

where $v_f(T)$ is the propagation velocity for TPD at the specific annealing temperature, d_0 is the total thickness of the film and t_{ann} is the corresponding annealing time. Therefore, the bulk transformed fraction can be obtained from the experimental data as indicated in Equation 5.4, expression that considers the possible overlap between liquid regions already transformed by the other mechanism.

$$f = x_l^{front}(1 - x_l^{bulk}) + x_l^{bulk} \quad (5.4)$$

In Equation 5.4, f is the total transformed fraction (front & bulk) estimated as explained in Section 5.2.1 and x_l^{bulk} is the transformed fraction that we would have if there was only bulk transformation. Substituting by the experimental values, we find that the front

transformation accounts at most to around a 5% of the total transformation fraction at the end of the transformation, taking values below this 5% for shorter annealing times. This result reaffirms the bulk character of this transition and also that the FC glass peak emerges from the formation of liquid regions in the bulk of the material and not from the front.

The estimated bulk transformed fraction as a function of annealing time of the 35 μm thick sample is shown in Figure 5.8, together with the transformed fraction of the capped thin film glass annealed at the same temperature ($T_g+14\text{K}$) for comparison. It can be observed that both curves present slightly different shapes and total transformation times. The differences between these two curves will be explained in Section 5.4, in the context of the dynamics of liquid formation.

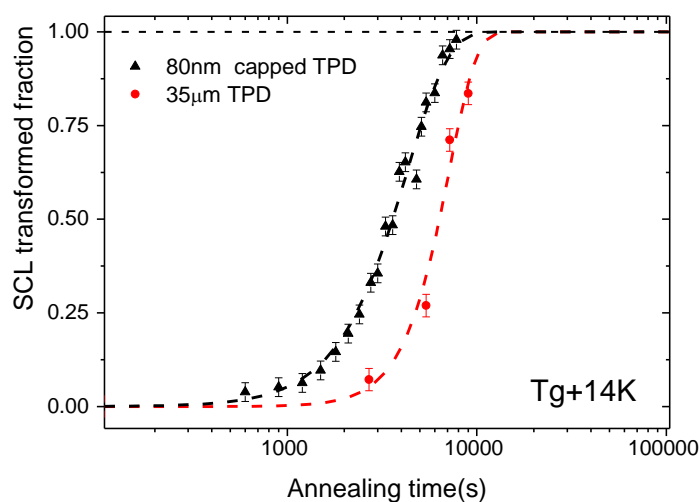


Figure 5. 8. Transformed fraction vs annealing time of a 35 μm thick sample (red solid circles) and a capped TPD glass (black solid triangles) during an isothermal annealing at $T_g+14\text{K}$. The dashed lines correspond to KJMAE fittings imposing $n=2$ for the capped film and $n=3$ for the bulk TPD sample.

5.4 Dynamics of liquid formation: KJMAE formalism

As we have seen in the previous sections, the glass transition in the bulk of vapor deposited stable glasses proceeds mainly by the transformation of the glass directly into the liquid phase. We have also seen that the transformed fraction as a function of annealing time presents a sigmoidal shape typical from nucleation and growth like kinetics. Based on these observations, as well as on previous analysis reported by other

authors [1,12], we proceed to study the evolution of the transformed fraction using the Kolmogorov-Johnson-Mehl-Avrami-Erofeev (KJMAE) formalism [5–8].

The KJMAE model (also known as Avrami model) quantifies the space occupied by a new phase during a transformation event based on statistical considerations. The Avrami equation establishes a relation between the new phase transformed fraction (liquid fraction in our case), x_l , and the extended fraction, x_{ext} , defined as the fraction from the total volume that would transform into the new phase if no space limitations and impingement between transforming regions were considered. Therefore, the extended fraction can grow up to infinity.

If nucleation is random in space but we restrict the new nucleation sites to the untransformed volume of the sample, then, the real transformed volume is only a fraction of the extended volume: $dV = dV_{ext}(1 - x_l)$ or, equivalently for SCL transformed fraction, $dx_l = dx_{ext}(1 - x_l)$. Integrating this equation yields the well-known Avrami equation:

$$x_l = 1 - \exp(-x_{ext}) \quad (5.5)$$

where the evolution of the extended fraction, x_{ext} , as function of time/temperature depends on the transformation mechanism and the dimensionality. For a sample with volume V , the extended fraction can be expressed as follows:

$$x_{ext}(t) = \frac{V_{ext}(t)}{V} = \int_0^t \frac{4}{3} \pi r(\tau, t)^3 I(\tau) d\tau \quad (5.6)$$

where I is the nucleation frequency, which has a strong dependence on temperature, and the nuclei have been assumed to have a spherical geometry. During an isothermal annealing, if the growth is 3D and the radius evolves as $r(\tau, t) = r^* + u(t - \tau) \approx u(t - \tau)$, with a critical nucleus, r^* , small compared to $u(t - \tau)$ (here t is the time, τ the time of the nucleation event and u the growth rate, which is assumed to depend only on temperature), the transformed fraction can be rewritten as:

$$x_{ext} = \frac{4\pi}{3} \int_0^t I u^3 (t - \tau)^3 d\tau \quad (5.7)$$

In the case the nucleation frequency is also constant, then:

$$x_{ext} = \frac{\pi}{3} I u^3 t^4 \quad (5.8)$$

The KJMAE equation is often written for an isothermal treatment as:

$$x_l = 1 - \exp(-x_{ext}) = 1 - \exp(-(Kt)^n) \quad (5.9)$$

where K depends strongly on the temperature and it groups all the constants resulting from the x_{ext} calculation (such as nucleation rate, I , number of pre-existing nuclei, N , in case $I = 0$ and the growth rate, u); and n , also known as the Avrami exponent, contains information on the transformation mechanism and the growth dimensions. Therefore, using the KJMAE equation for the expression obtained in Equation 5.8 we obtain $n = 4$ and $K = ((\pi/3) Iu^3)^{1/4}$.

If the growth is 2D, the nuclei are disks of radius $r = r^* + u(t - \tau) \approx u(t - \tau)$ and in an analogous procedure as the above mentioned, we obtain $n = 3$ and $K = (\pi Iu^2/3)^{1/3}$.

Further, if the nucleation frequency is set to zero because all nuclei already exist at $t = 0$ s, for a 3D growth we have $x_{ext} = \frac{V_{ext}}{V} = \frac{4\pi}{3} Nu^3 t^3$, therefore $K = \left(\frac{4\pi}{3} Nu^3\right)^{1/3}$ and $n = 3$, and calculating the extended fraction in a 2D system, we obtain $K = (\pi Nu^2)^{1/3}$ and $n = 2$.

In general, the KJMAE formalism assumes n exponents with integer values between 1 and 4, depending on the transformation characteristics of the system (see Table 5.1).

Table 5. 1. Table that groups the different values of the Avrami exponent, n , and their associated dynamics. In general, for uniform nucleation and growth, $n = D + 1$, where D is the dimensionality of space in which the new phase grows. Systems with mixed transformation mechanisms for example with pre-existing nuclei at $t=0$ but also with uniform nucleation rate at $t>0$, will present Avrami exponents in between these values. A change in the nuclei's geometry would also translate in a change of this exponent.

<i>Avrami exponent</i>	<i>Transformation characteristics</i>
$n = 1$	pre-existing nuclei and linear growth
$n = 2$	pre-existing nuclei and 2D growth or Uniform nucleation and linear growth of the new phase
$n = 3$	pre-existing nuclei and 3D growth or uniform nucleation and growth of the new phase in 2D
$n = 4$	Uniform nucleation and growth of the new phase in 3D

It is important to note that for the derivation of the Avrami equation (Equation 5.9) it is necessary to make a number of significant assumptions and simplifications which translate in many limitations when using this model: i) It considers that nucleation occurs randomly and homogeneously over the entire untransformed part of the sample, ii) it also considers that the nuclei start growing immediately after their appearance, iii) it does not contemplate systems with mixed mechanisms, such as pre-existing nuclei and simultaneous nucleation rate, and iv) it assumes the growth occurs at a constant rate in all directions during the entire transformation time. Therefore, even though it is a good tool to describe transitions that follow a nucleation and growth like kinetics, it might not be completely accurate to describe systems in which one or more of these crucial parameters undergo changes along the transformation. Nevertheless, it constitutes a useful model to study qualitatively the transformation mechanism and compare the dynamics at different temperatures.

In our study, we use the KJMAE model, Equation 5.9, mainly to infer the mechanism of the transformation, encoded in the exponent n (also gives information on dimensionality growth) and the Avrami constant K (which allows to determine jointly growth velocity and nucleation rate/number of initial nuclei).

Regarding the Avrami exponent, a convenient representation is the $\ln(-\ln(1 - x_t))$ vs. $\ln(t)$ plot. This representation relates to the expression 5.9 as follows:

$$\begin{aligned} x_t = 1 - \exp(-(Kt)^n) &\Rightarrow 1 - x_t = \exp(-(Kt)^n) \Rightarrow \ln(1 - x_t) = -(Kt)^n \Rightarrow \\ &\Rightarrow \ln(-\ln(1 - x_t)) = n \ln(t) + n \ln(K) \end{aligned} \quad (5.10)$$

Using this representation, the slope of the curves yields direct visualization of the exponent n . Figure 5.9 shows the data of the transformed fraction as a function of annealing time of the capped thin films and of the thick TPD layer (Figures 5.5 and 5.8, respectively) in a $\ln(-\ln(1 - x_t))$ vs. $\ln(t)$ plot. Note that the data in Figure 5.9 has been normalized by the time required to transform completely the sample (t_{trans}) in an identical way to the normalization performed in Figure 5.5b for the capped glasses. Fitting the data with a linear function, we obtain $n = 2.1 \pm 0.1$ for the capped thin films (open symbols) and $n = 3.4 \pm 0.1$ for the thicker sample (solid symbols). The experimental value of $n = 2.10$ found for the thin capped TPD layers is consistent with a 2D growth with zero nucleation frequency (see Table 5.1), that is, the initiation sites of the

transformation already exist at $t = 0$ s. If the nucleation frequency was constant over time, the exponent for 2D growth would be three instead of two. The bulk sample (35 μ m thick) transforms with a higher exponent, $n = 3.4$, which suggests a 3D growth also with preexisting nuclei (see Table 5.1). However, it is important to note that both exponents are slightly above 2 and 3, respectively, indicating that the growth may not be purely 2D in the case of the thin film, or that in both cases (thin and thick samples), aside from the pre-existing nuclei, there is also a certain nucleation frequency of new liquid seeds. As we will see in the following chapters the second case seems to be the most plausible scenario.

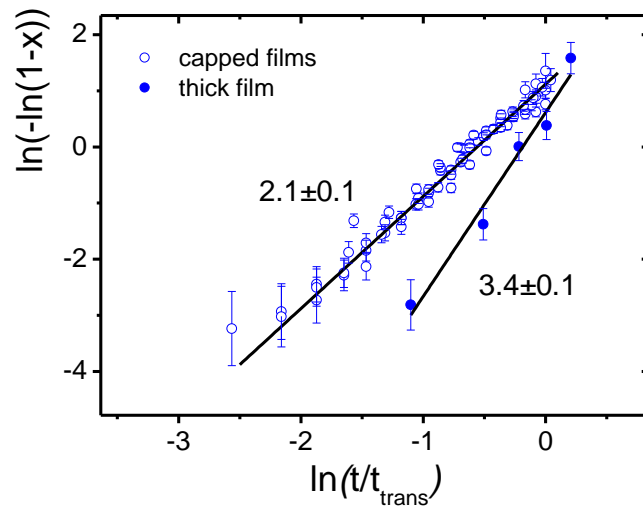


Figure 5. 9. $\ln(-\ln(1-x))$ vs logarithm of the transformation time normalized by t_{trans} for both thick (solid symbols) and capped films (open symbols). Performing a linear fit, we obtain $n = 2.1$ for the capped thin films and $n = 3.4$ for the thicker layers, which suggests a 2D and 3D growth with pre-existing nuclei, respectively. The black solid lines correspond to the linear fittings.

As a first approach, we will assume the Avrami exponents to be $n = 2$ (for the thin films, 2D growth with no nucleation rate) and $n = 3$ (for the bulk samples, 3D growth with no nucleation rate). Fitting the experimental specific heat data (in Figure 5.5a and 5.8) with the KJMAE equation (Equation 5.9) imposing $n = 2$ for the capped thin films and $n = 3$ for the thick samples, we can obtain the Avrami constant K for the different samples studied in this chapter (fitting values are shown in Table 5.2). Depending on the characteristics of the system (mainly mechanism of transformation and dimensionality), we have seen that K will present different expressions. For systems with no nucleation

rate, we found $n = 2$ and $K = (\pi Nu^2)^{1/3}$ for 2D growth, and $K = \left(\frac{4\pi}{3} Nu^3\right)^{1/3}$ with $n = 3$ for 3D systems. From these expressions we could calculate the number of pre-existing “transformation sites”, N , and infer the distance between them, $\langle d \rangle$. However, the rate at which the liquid regions grow inside the glass matrix during the isothermal annealing (u) is also an unknown parameter. As a first approximation, we can assume they propagate at the same velocity as the growth fronts in thin film glasses. Later on, in Chapter 6, we will see that this is indeed a good approximation.

The data of the growth front velocity, v_{gr} , can be taken from previously studies which measured the propagation fronts in stable TPD glasses (red circles in Figure 5.10) [2,19,22]. Although vapor-deposited glasses develop distinct anisotropic molecular orientations depending on the deposition temperature [23], in thin film TPD glasses grown at $0.85T_g$ the effect is very small so we assume the growth front velocity of the liquid patches to be nearly isotropic in our samples [24].

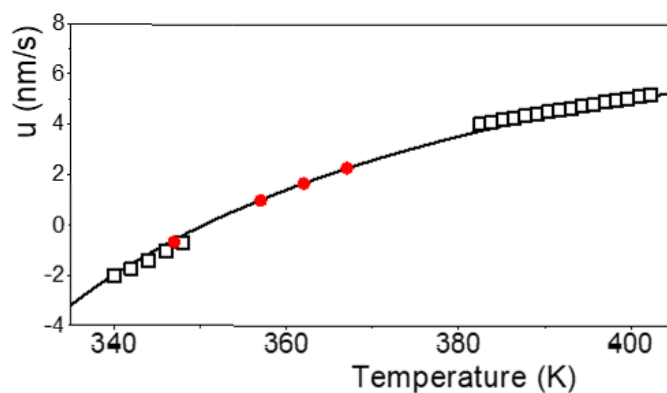


Figure 5.10. Growth front velocity as a function of temperature for TPD ultrastable glasses annealed at $T_g+14\text{K}$, $T_g+24\text{K}$, $T_g+29\text{K}$ and $T_g+34\text{K}$ (red solid circles) [19], together with the reported experimental values at higher and lower temperatures (open symbols) [2]. The black solid line is the expected front velocity calculated using the equation $\log(u) = \log(d) - 0.5[\log(t_{bulk}) + \log(\tau_\alpha)]$ as described in [2]. Figure adapted from [2].

From the previously obtained values of K and the propagation rate, we can finally infer the number of pre-existing liquid seeds and the average spatial distance between them, $\langle d \rangle$. Note that since we consider the nucleation rate to be zero for this samples, the

distance between liquid regions reminds constant on average. The results obtained can be found in Table 5.2.

The number of pre-existing nuclei, N , presents values between 1×10^{11} and 3×10^{11} nuclei/m² for the capped layers and amounts to 6×10^{16} nuclei/m³ for the bulk sample. The average spatial distance between initiation sites in the thin glassy layers, $\langle d \rangle$ (evaluated using the expression $(1/N)^{-D}$, being D equal to 2 or 3 for thin and thick films, respectively), ranges from 1.8 μm to 3.1 μm , without any clear trend with the annealing temperature. The value for the thick films, 2.5 μm , lies in the same range.

Table 5. 2. Best fitting values of the main parameters controlling the bulk transformation (number of pre-existing nuclei and distance between nucleation seeds) obtained by fitting the experimental data in Figures 5.5 and 5.8 with the KJMAE equation. Uncertainties correspond to the square sum of the instrumental and statistical error. Front velocity extracted from Figure 5.10.

	$T_{\text{annealing}}$	Front velocity (nm/s)	n	K (nuclei/s ²)	N (nuclei/m ²)	$\langle d \rangle$ (μm)
THIN FILMS	$T_g+14\text{K}$	0.22	2	$(2.3 \pm 0.1) \times 10^{-4}$	$(2.3 \pm 0.2) \times 10^{11}$	2.1 ± 0.1
	$T_g+24\text{K}$	10.0	2	$(4.4 \pm 0.2) \times 10^{-3}$	$(1.1 \pm 0.1) \times 10^{11}$	3.1 ± 0.1
	$T_g+29\text{K}$	48.2	2	$(2.7 \pm 0.1) \times 10^{-2}$	$(1.3 \pm 0.1) \times 10^{11}$	2.8 ± 0.1
	$T_g+34\text{K}$	193.8	2	0.14 ± 0.01	$(3.1 \pm 0.1) \times 10^{11}$	1.8 ± 0.1
THICK FILM	$T_g+14\text{K}$	0.22	3	$(1.4 \pm 0.1) \times 10^{-4}$	$(6.7 \pm 0.1) \times 10^{16}$	2.5 ± 0.1

The giant length scale associated with the distance between initiation sites is one of the main and more surprising results in terms of glassy physics. These observations agree, roughly, with estimations of earlier work [1], with recent simulation on stable computer-generated glasses [12,13] and compares well also with the crossover length for the front-to bulk transition in highly stable TPD glasses measured in independent experiments [2]. The transition from 2D to 3D growth between 85nm and 35 μm thick films could be a consequence of the average distance between initiation sites $\langle d \rangle \approx 2.5 \mu\text{m}$. When the thickness of the TPD layer (85nm) is much lower than $\langle d \rangle$, the nuclei reach the final vertical dimension shortly after its formation and its growth proceeds laterally in 2D over time. On the contrary, the bulk sample has a thickness much larger than $\langle d \rangle$ and the liquid patches grow simultaneously in all directions (3D growth).

We also reproduced the experimental data using a Monte Carlo approach in which the initial seeds of the transformation are randomly distributed in the sample and the regions of high mobility propagate radially as $r(t) = r^* + v_{gr}t$. Several snapshots of the simulation are reproduced in the inset of Figure 5.11. An excellent match of the experimental data (continuous red line at T_g+24K in Figure 5.11) is achieved using parameters close to those obtained by fitting with the KJMAE equation (Table 5.2). Therefore, supporting the idea of the bulk transformation starting at certain regions of the glass and growing across the sample.

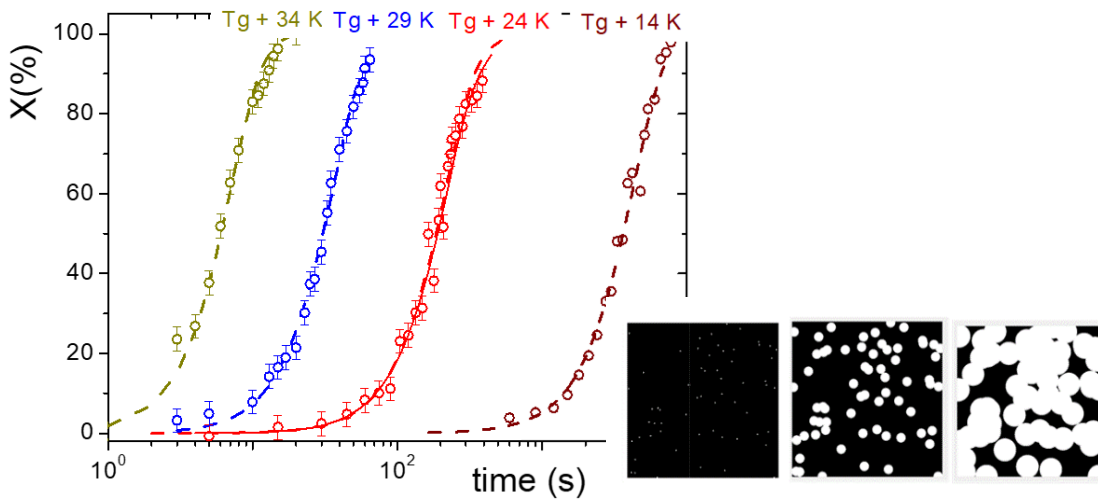


Figure 5. 11. Monte Carlo fitting of the transformed fraction of a sample grown at 285K and annealed at T_g+24K (solid red line). The set of three images on the bottom right is a representation of the growth of 2D nuclei over time where the left image corresponds to the initiation sites at $t=0s$. Dashed lines in the graph are the KJMAE fittings imposing $n=2$.

The analysis of the transformed fraction data leads to the conclusion that the glass transformation in capped ultrastable glasses takes place via the formation and growth of equilibrated liquid regions. Unfortunately, our heat capacity data does not provide any direct microscopic evidence of the origin of the initiation sites. Further experiments by small angle X-ray scattering or related techniques may be useful to identify them. At this stage, we can only speculate about its origin. We foresee two scenarios: i) the transformation of the glass into the SCL initiates at regions with lower density [25] that are randomly distributed within the sample but spatially separated by few microns (structural origin), or ii) the stable glass contains nanoscopic regions that become active at the annealing temperature and transform into liquid that grows into the glassy matrix

(dynamic origin). In this view, the material has a broad distribution of local fictive temperatures and the softening of the glass matrix along the isotherm prompts the emergence of new equilibrated regions with time. In a system with 2D growth, this view would be compatible with an Avrami exponent $n = 3$. The value $n = 2.10$, slightly above 2, obtained for our thin films could be an indication that while in this case most of the sample transforms dominated by the growth of pre-existing “transformation sites”, still some new liquid regions appear during the transition, having a mix of two different mechanisms. Further details on this topic will be analyzed in Chapters 6 and 7.

Independently of the origin of the “transformation sites” or initiation seeds, once a local region becomes highly mobile dynamic facilitation eases its propagation to neighboring regions with lower T_f , propagating the transformation until the sample is totally transformed. This scenario is supported by different theories such as RFOT [11] or dynamic facilitation theories [10].

5.5 Validity of the KJMAE model on nanocalorimetry specific heat data

As we briefly discussed in Section 5.4, the KJMAE formalism presents some limitations when analyzing systems with dynamics that can vary during the transformation process. Avrami is a mean-field model, and therefore, it provides general information on the transformation mechanism although it does not allow to easily identify and analyze information of local phenomena or local variations during the transformation, such as a non-constant nucleation rate or a change in the growth velocity. In this scenario, where we are applying a model that averages onto the whole sample, small variations in growth velocity, growth geometry, delayed nucleation rate or variable nucleation rates, among others, could lead to a misinterpretation of the transformation mechanism or to lose some insights on its dynamics. In this sense, temperature homogeneity of the sensing area of the calorimeter becomes also a critical factor, since both the deposition temperature and the annealing temperature are key parameters for the stability of the glass and the dynamics of the transformation. When annealing at such high temperatures above T_g , variations of just a few degrees can result in huge changes in the dynamics since the relaxation time has a super-Arrhenius behavior with temperature [26]. Therefore,

guaranteeing the maximum homogeneity in the temperature profile of the nanocalorimeters is of great importance. However, in real devices some inhomogeneities are bound to appear. Figure 5.12 shows the temperature profile of the sensing area of the calorimeter (shown as a histogram of the temperature distribution) during an isothermal annealing at 347K (T_g+14K), obtained from Finite Element Modeling (FEM) in steady state conditions using COMSOL Multiphysics.

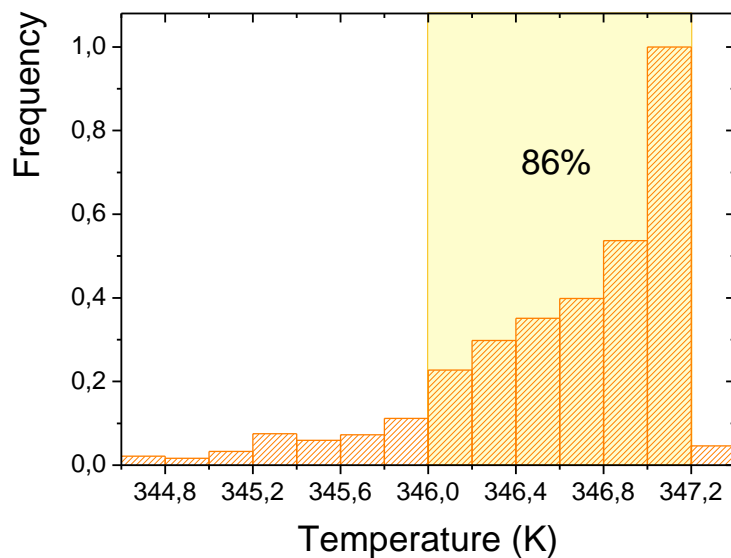


Figure 5. 12. Histogram of the temperature profile of the sensing area of the nanocalorimeter during an isothermal annealing at T_g+14K obtained from finite element modeling in steady state conditions using COMSOL Multiphysics. The shadowed region indicates that 86% of the sensing area is at a temperature between 346K and 347.2K during the isothermal annealings.

As it can be seen in Figure 5.12, even if a 200nm Aluminum thermal plate is deposited to improve the temperature profile (see Section 3.2.2.2), differences in temperature of around 3K are still expected. While most of the sensing area is at temperatures between 346K and 347K (86%), some regions are at lower temperature. These inhomogeneities in temperature can affect the measurements in two different ways: i) they could affect the stability of the glass due to changes on the deposition temperature (which would yield glasses with lower stabilities) and ii) they could affect the transformation dynamics during the isothermal annealing. Regions with lower temperature, will transform with slower transformation dynamics, delaying the total transformation process.

In order to estimate the influence of an inhomogeneous temperature profile as the one shown in Figure 5.12 during an isothermal annealing at $T_g+14\text{K}$ (347K), we calculate the transformed fraction for a specific system using the Avrami equation, $x_t = 1 - \exp(-(Kt)^n)$.

For the particular case of a sample with 2D growth and constant nucleation rate, we've seen that the Avrami parameters are $n = 3$ and $K = \pi l u^2 / 3$ (see Section 5.4), where K is temperature dependent. Due to the temperature profile, areas with different temperatures will evolve at a different pace. The total transformed fraction, x_t^{total} will be given by the sum of the transformed fraction of each of these areas at every temperature, weighted by its corresponding percentage (Figure 5.12).

Considering a nucleation rate independent of temperature and with a value consistent with the total transformation time observed for the experimental data, and a growth rate, u , described by Equation 2.1, we can calculate the parameter K for each temperature interval and therefore, obtain the corresponding transformed fraction. The total transformed fraction is shown in Figure 5.13a (solid black line) in comparison with the transformed fraction expected for a transformation of a measuring setup with no temperature inhomogeneities (dashed red line). As it can be seen, while for the first stages of the transformation both curves show a similar behavior, at long annealing times, the transformed fraction of the sample with temperature inhomogeneities, deviate from the expected behavior delaying the last stages of the transformation.

This slowing down at longer annealing times can be better appreciated in the $\ln(-\ln(1 - x_t))$ vs. $\ln(t)$ plot (Figure 5.13b). In this representation, it can be observed that for the first stages of the transformation, the Avrami exponent ($n = 3$) agrees with the expected value for a 2D growth with constant nucleation rate. However, at longer times the curve changes its tendency decreasing its slope ($n \rightarrow 2$). We can expect, therefore, that the bigger the temperature gradients on the sensing area, the flatter our transformed fraction curves will be. Thus, the exponent obtained from fitting the experimental data won't correspond exactly with what is happening in reality in our sample.

Note that this study is taking into account only the effect of the temperature due to the isothermal annealing, considering that all the glass has the same stability. However, the temperature profile is also important during the deposition process, where

inhomogeneities can result in glasses with a broad range of relaxation times. In this case, regions with lower stability would start the transformation faster, accelerating the total transformation process, that is, the transformation would start at lower annealing times and transform completely for shorter transformation times.

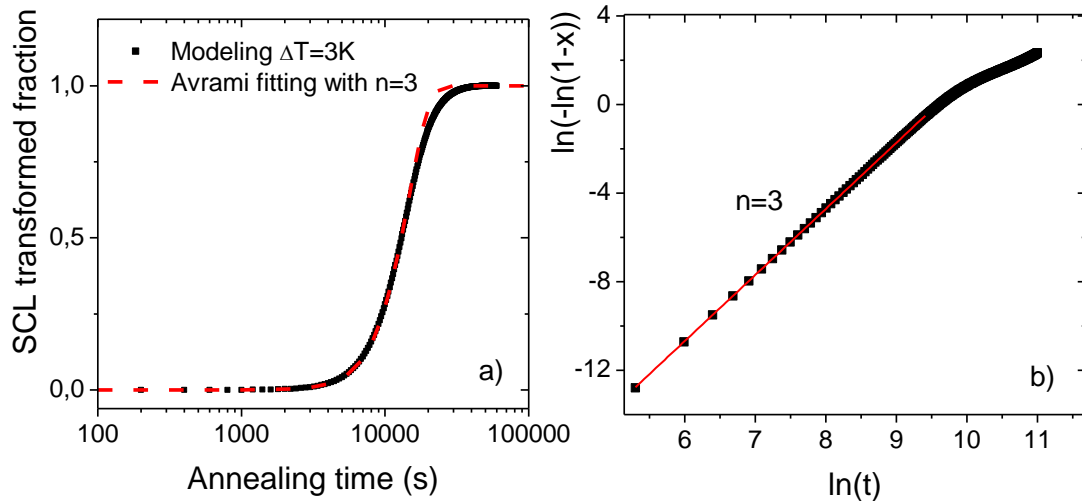


Figure 5.13. (a) Evolution of the liquid transformed fraction as a function of annealing time for a system with constant nucleation rate and 2D growth during an annealing treatment at $T_g+14\text{K}$ with a temperature profile as the one indicated in Figure 5.12 obtained with COLMSOL Multiphysics. The dashed red line indicates the expected evolution of the transformed fraction if no temperature inhomogeneities were present. (b) $\ln(-\ln(1-x_i))$ vs. $\ln(t)$ plot of the same system to highlight the Avrami exponent. While at the first stages of the transformation we obtain the expected $n=3$ characteristic of their transformation, for longer annealing times this slope decreases. The solid red line is a lineal fit with slope equal to 3.

At the same time, defects on the substrate (Al plate in our case) could also induce the transformation of the sample. In this case again, we would expect the dynamics of the transformation to be faster and start at lower annealing times or temperatures.

With the idea of highlighting the importance of the homogeneity in the sensing area of the devices (in temperature or structural defects), in Figure 5.14 we present the evolution of the transformed fraction of a ultrastable glass ($T_{dep}=285\text{ K}$) at 347 K ($T_g+14\text{K}$) for two different nanocalorimeters. As it can be seen, the same measurement in two different devices results in slightly different behavior. While the transformed fraction obtained with the Device 2 (green solid diamonds) fits better for an Avrami exponent $n = 3$ and it just deviates at longer annealing times, Device 1 yields a curve that shows an Avrami exponent closer to $n = 2$ (black solid circles). In addition, Device 1 seems to start and complete the transformation in a shorter time interval. We attribute these differences to

the presence of more nucleation sites (due to surface defects or a higher temperature gradient during the deposition process) and/or the existence of a variety of growth rates associated to areas of the calorimeter with higher/lower average temperatures, which accelerate/delay the transformation (due to gradients on the sensing area).

It is important to note that even with all these differences, the general conclusions for this study are still valid, since all the samples in this chapter were measured with the same device (Device 1). The calorimetric measurements presented in the following chapters are all performed with Device 2.

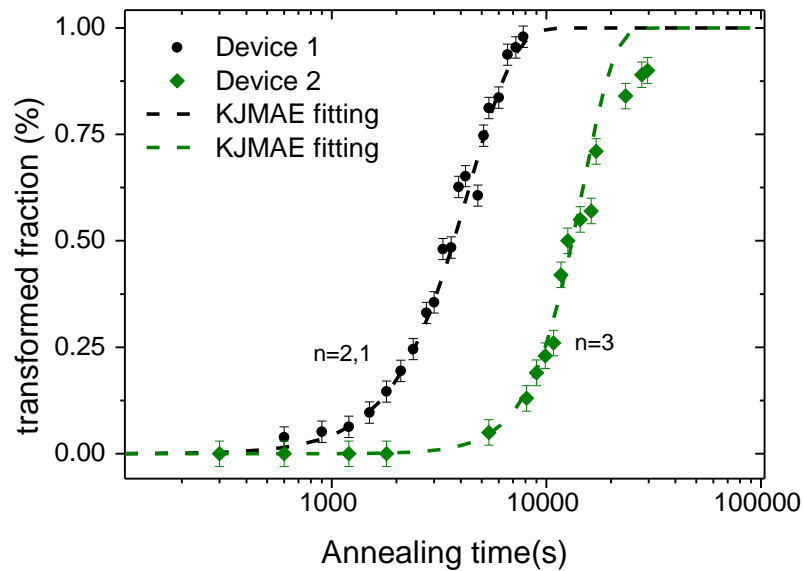


Figure 5.14. Transformed fractions as a function of annealing time of identical capped samples grown at 285K after an annealing treatment at $T_g+14\text{K}$ using Device 1 (black solid circles), used to study the samples presented in this chapter, and Device 2 (green solid diamonds), used for calorimetric measurements in the following chapters. The differences in transformation rate and total transformation time could be associated to inhomogeneities on the sensing area of the calorimeter.

5.6 Summary

In this chapter we have seen that the bulk transformation of vapor deposited ultrastable glasses into the supercooled liquid proceeds via a process dominated by the growth of liquid regions inside the glass following a nucleation and growth like kinetics. The simultaneous softening of the stable glass, although present, does not seem to play a significant role in the transformation of these highly stable glasses. Regarding the kinetics

of the transformation, the exponents associated with the evolution of the transformed fraction, $n \approx 2$ for thin films and $n \approx 3$ for bulk glasses, correlate well with the 2D or 3D nature of the transformation and indicate that the nucleation is highly heterogeneous and that it starts at pre-existing seeds already present at $t=0$ s. Even though the obtention of Avrami exponents slightly above 2 and 3, specially for the 3D sample ($n = 3.4$), hints the possibility that the transformation takes place via a mixed mechanism where nucleation rate is not strictly zero.

Surprisingly, the density of these initiation sites appears to be independent of the annealing temperature. From the pre-existing seeds, the transformation then proceeds driven by kinetic facilitation. We have assumed the growth velocity to be of the order of the one measured for the propagation fronts in thin film TPD samples [19]. Under this consideration we obtain a large separation distance between initiation sites, on the micrometer length scale, which determines the crossover length between the front and bulk transformation and compares well with measurements obtained in independent experiments [17]. The origin of this initiation sites is still not completely understood due to the lack of a direct visualization of these emergent liquid regions using calorimetric studies, however, we speculate they originate in regions of the sample where the mobility is higher (i.e., due to dynamic heterogeneities). This is consistent with different simulation works, where stable glasses are also found to transform via the emergence of equilibrated regions that grow into the surrounding glass matrix [10,27,28].

Finally, a study on the temperature heterogeneities of the sensing area of the calorimeter exposed the importance of homogeneous temperature profiles as well as low defect surfaces for the study of the fast dynamics in capped thin films. We have seen how differences in temperature of just a few degrees can change significantly the shape of the transformation, leading to misinterpretations of the overall mechanism.

References

- [1] K. L. Kearns, M. D. Ediger, H. Huth, and C. Schick, *One Micrometer Length Scale Controls Kinetic Stability of Low-Energy Glasses*, J Phys Chem Lett **1**, 388 (2010).
- [2] C. Rodríguez-Tinoco, M. Gonzalez-Silveira, J. Ràfols-Ribé, A. Vila-Costa, J. C. Martinez-Garcia, and J. Rodríguez-Viejo, *Surface-Bulk Interplay in Vapor-Deposited Glasses: Crossover Length and the Origin of Front Transformation*, Phys Rev Lett **123**, (2019).
- [3] J. Ràfols-Ribé, M. Gonzalez-Silveira, C. Rodríguez-Tinoco, and J. Rodríguez-Viejo, *The Role of Thermodynamic Stability in the Characteristics of the Devitrification Front of Vapour-Deposited Glasses of Toluene*, Phys. Chem. Chem. Phys **19**, 11089 (2017).
- [4] C. Rodriguez-Tinoco, M. Gonzalez-Silveira, M. A. Ramos, and J. Rodriguez-Viejo, *Ultrastable Glasses: New Perspectives for an Old Problem*, La Rivista Del Nuovo Cimento **45**, 325 (2022).
- [5] M. Avrami, *Kinetics of Phase Change. I General Theory*, J Chem Phys **7**, 1103 (1939).
- [6] A. N. Kolmogorov, *On the Statistical Theory of the Crystallization of Metals*, Bulletin of the Academy of Sciences of the USSR, Mathematics Series **1**, 355 (1937).
- [7] W. A. Johnson and R. Mehl, *Reaction Kinetics in Processes of Nucleation and Growth*, Trans. Am. Inst. Min. Metall. Eng. **135**, (1939).
- [8] M. Avrami, *Kinetics of Phase Change. II Transformation-Time Relations for Random Distribution of Nuclei*, J Chem Phys **8**, 212 (1940).
- [9] A. Wisitsorasak and P. G. Wolynes, *Dynamical Heterogeneity of the Glassy State*, J Phys Chem B **118**, 7835 (2014).
- [10] R. Gutiérrez and J. P. Garrahan, *Front Propagation versus Bulk Relaxation in the Annealing Dynamics of a Kinetically Constrained Model of Ultrastable Glasses*, Journal of Statistical Mechanics: Theory and Experiment **2016**, 074005 (2016).
- [11] P. G. Wolynes, *Spatiotemporal Structures in Aging and Rejuvenating Glasses*, Proc Natl Acad Sci U S A **106**, 1353 (2009).
- [12] R. L. Jack and L. Berthier, *The Melting of Stable Glasses Is Governed by Nucleation-and-Growth Dynamics*, Journal of Chemical Physics **144**, (2016).
- [13] E. Flenner, L. Berthier, P. Charbonneau, and C. J. Fullerton, *Front-Mediated Melting of Isotropic Ultrastable Glasses*, Phys Rev Lett **123**, 175501 (2019).
- [14] A. Ninarello, L. Berthier, and D. Coslovich, *Models and Algorithms for the Next Generation of Glass Transition Studies*, Phys Rev X **7**, 21039 (2017).
- [15] S. F. Swallen, K. L. Kearns, M. K. Mapes, Y. S. Kim, R. J. McMahon, M. D. Ediger, T. Wu, L. Yu, and S. Satija, *Organic Glasses with Exceptional Thermodynamic and Kinetic Stability*, Science (1979) **315**, 353 (2007).
- [16] E. Leon-Gutierrez, A. Sepúlveda, G. Garcia, M. T. Clavaguera-Mora, and J. Rodríguez-Viejo, *Stability of Thin Film Glasses of Toluene and Ethylbenzene Formed by Vapor Deposition: An in Situ Nanocalorimetric Study*, Physical Chemistry Chemical Physics **12**, 14693 (2010).

- [17] A. Sepúlveda, S. F. Swallen, and M. D. Ediger, *Manipulating the Properties of Stable Organic Glasses Using Kinetic Facilitation*, J Chem Phys **138**, 12A517 (2013).
- [18] S. F. Swallen, K. L. Kearns, S. Satija, K. Traynor, R. J. McMahon, and M. D. Ediger, *Molecular View of the Isothermal Transformation of a Stable Glass to a Liquid*, J Chem Phys **128**, 214514 (2008).
- [19] D. M. Walters, R. Richert, and M. D. Ediger, *Thermal Stability of Vapor-Deposited Stable Glasses of an Organic Semiconductor*, J Chem Phys **142**, 134504 (2015).
- [20] J. Ràfols-Ribé, A. Vila-Costa, C. Rodríguez-Tinoco, A. F. Lopeandía, J. Rodríguez-Viejo, and M. Gonzalez-Silveira, *Kinetic Arrest of Front Transformation to Gain Access to the Bulk Glass Transition in Ultrathin Films of Vapour-Deposited Glasses*, Physical Chemistry Chemical Physics **20**, 29989 (2018).
- [21] M. T. Clavaguera-Mora, N. Clavaguera, D. Crespo, and T. Pradell, *Crystallisation Kinetics and Microstructure Development in Metallic Systems*, Prog Mater Sci **47**, 559 (2002).
- [22] A. Sepúlveda, S. F. Swallen, and M. D. Ediger, *Manipulating the Properties of Stable Organic Glasses Using Kinetic Facilitation ARTICLES YOU MAY BE INTERESTED IN*, J. Chem. Phys **138**, 12 (2013).
- [23] S. S. Dalal, D. M. Walters, I. Lyubimov, J. J. de Pablo, and M. D. Ediger, *Tunable Molecular Orientation and Elevated Thermal Stability of Vapor-Deposited Organic Semiconductors*, Proceedings of the National Academy of Sciences **112**, 4227 (2015).
- [24] C. Rodríguez-Tinoco, M. Gonzalez-Silveira, J. Ràfols-Ribé, A. F. Lopeandía, and J. Rodríguez-Viejo, *Transformation Kinetics of Vapor-Deposited Thin Film Organic Glasses: The Role of Stability and Molecular Packing Anisotropy*, Physical Chemistry Chemical Physics **17**, 31195 (2015).
- [25] C. Scalliet, L. Berthier, and F. Zamponi, *Nature of Excitations and Defects in Structural Glasses*, Nat Commun **10**, 5102 (2019).
- [26] C. Rodríguez-Tinoco, J. Ràfols-Ribé, M. González-Silveira, and J. Rodríguez-Viejo, *Relaxation Dynamics of Glasses along a Wide Stability and Temperature Range*, Sci Rep **6**, 35607 (2016).
- [27] M. Lulli, C. S. Lee, H. Y. Deng, C. T. Yip, and C. H. Lam, *Spatial Heterogeneities in Structural Temperature Cause Kovacs' Expansion Gap Paradox in Aging of Glasses*, Phys Rev Lett **124**, (2020).
- [28] C. J. Fullerton and L. Berthier, *Density Controls the Kinetic Stability of Ultrastable Glasses*, EPL (Europhysics Letters) **119**, 36003 (2017).

Chapter 6

AFM study of the glass transition in capped ultrastable glasses

As we have seen in Chapters 4 and 5, nanocalorimetry is a powerful technique to characterize the glass transition in vapor-deposited glasses and study the transformation dynamics of thin films.

Using the capping strategy in thin films we were able to identify, via calorimetric measurements above T_g , the appearance of distinguishable liquid regions which grow inside the glass matrix dominating the transformation into the supercooled liquid. Information on the transformation dynamics, however, can only be inferred indirectly, using physical models such as the KJMAE formalism to try to reproduce the evolution of the transition from the measured heat capacity data. In no case, heat capacity data provides any direct evidence of the microscopic origin of the initiation sites for the liquid regions or a way to follow how these regions evolve with temperature or time.

Since direct spatial visualization of the equilibrated regions inside the glass is extremely challenging due to the subtle structural differences over very small distances, we propose a different strategy to identify them based on the local mechanical instabilities that these equilibrated liquid regions generate on a rigid ultrathin surface layer (TCTA in our case) grown on top of the glass (TPD).

Previous studies have shown that compressive stress on stiff films bonded to viscoelastic layers result in the buckling of their surface, which elastically deforms to relax the compressive stress giving rise to well-defined surface patterns [1–4]. Such surface

patterns can be induced in different ways [2,5] obtaining wrinkling motifs that can display rich surface morphologies depending on the characteristics of the system [5–7]. Among the different methods to induce wrinkling patterns, a recurrent one is capping a soft thin-film material (typically a polymer but also small-molecules organic layers) with a thinner metallic layer [4,5] or with a layer of another organic material with a higher T_g [8]. Annealing the polymer into the rubbery state promotes the formation of wrinkling across the whole surface of the cladding layer due to the appearance of compressive stress induced by the differences in the thermal expansion coefficients of the layers and the substrate. This process is called thermal wrinkling and it generally takes place across the whole surface simultaneously. Interestingly, wrinkling can also be locally induced at specific sites of the film by localized surface modifications on the substrate using focused ion beams [9] or by locally heating the sample with an external source, such as a laser [10]. In this last case, the instability is initiated with a circular laser that locally heats the polymer above its glass transition temperature promoting the appearance of wrinkling. The wrinkling pattern at the samples' surface is usually measured by means of AFM or SEM (Scanning Electron Microscopy).

In this chapter, we take advantage of the fact that our capped samples resemble considerably the systems in which thermal wrinkling can be produced (a small molecule organic layer, TPD, capped with a more rigid material, TCTA) to study the bulk-like transformation in highly stable glasses by means of AFM. For this study, the capped samples (TCTA/TPD/TCTA) are vapor deposited on top of silicon substrates, with lower thermal expansion coefficients compared with the organic layers, which will prompt the appearance of compression stress over the sample when the stack is heated above TPD's glass transition temperature. This compressive stress will induce the formation of wrinkles on the top TCTA layer as the TPD sample transforms into the supercooled liquid phase releasing the stress on the capping layer. Therefore, studying the formation of the wrinkling pattern by means of microscopic techniques we can have access to a direct visualization of the bulk transformation mechanism of this intermediate TPD layer.

6.1 Sample preparation and thermal protocol

For this study, samples of TCTA/TPD/TCTA were grown by PVD on top of Si substrates at a deposition temperature of 285 K ($0.85T_g$ for the TPD) and with thicknesses around 13nm for the TCTA layers and 63nm for the TPD interlayer. Once the samples are grown, they are moved to the AFM, where a temperature stage is assembled as detailed in the experimental methods Section 3.3.4. This temperature stage allows us to set the desired annealing temperature while measuring the sample's topography at the same time. This way, we are able to follow in real time any changes on the sample's surface during the thermal treatment. Figure 6.1. shows the thermal protocol followed by the sample: In first place, the sample is heated from room temperature up to T_g-5K (where T_g is the glass transition of the TPD) at a heating rate of 5K/min, which corresponds to the maximum heating rate we can achieve in this set up. Once the temperature is equilibrated at T_g-5K and the system is stable, we continue heating up the sample to the final annealing temperature. In this case, the annealing treatment was chosen to be at T_g+18K ($351 \pm 1K$) because the transformation time into the SCL is around 1h, a convenient time scale to follow the kinetics of the transformation in real time. It is important to consider that images are taken one by one and with no automated system and that each AFM scan of area $20 \times 20 \mu\text{m}^2$ takes around 4 minutes to be completed.

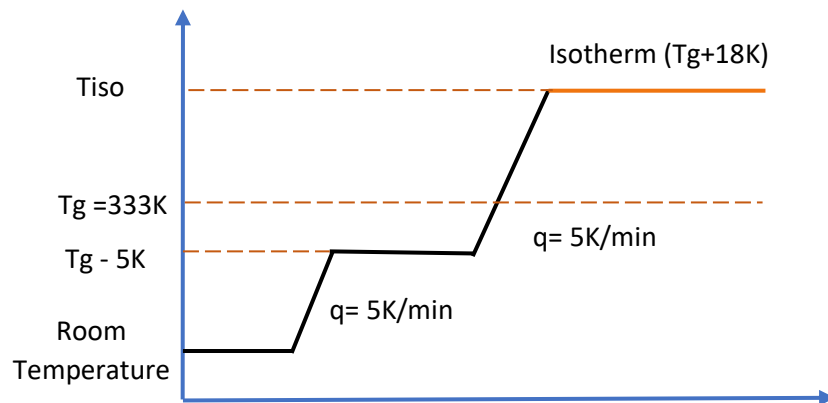


Figure 6. 1. Sketch of the thermal protocol followed by the samples during the study of the glass transition of TPD glass using AFM. The orange solid line indicates the moment that the image acquisition starts.

It is also important to remark that AFM techniques are not usually used with temperature stages due to the difficulty to thermally stabilize the cantilever. This can cause a thermal

drift as well as small changes in some measured magnitudes, such as height and distance measurements, because of thermal strain on the piezo electric elements when going up in temperature. For our measurements an uncertainty of around 10% in measured heights and distances was estimated. This uncertainty will need to be considered when analyzing the data.

6.2 AFM measurements: localized wrinkling induced by liquid formation

Figure 6.2 shows a series of *in situ* AFM images obtained at the same spatial location during the isothermal annealing at 351K (T_g+18K).

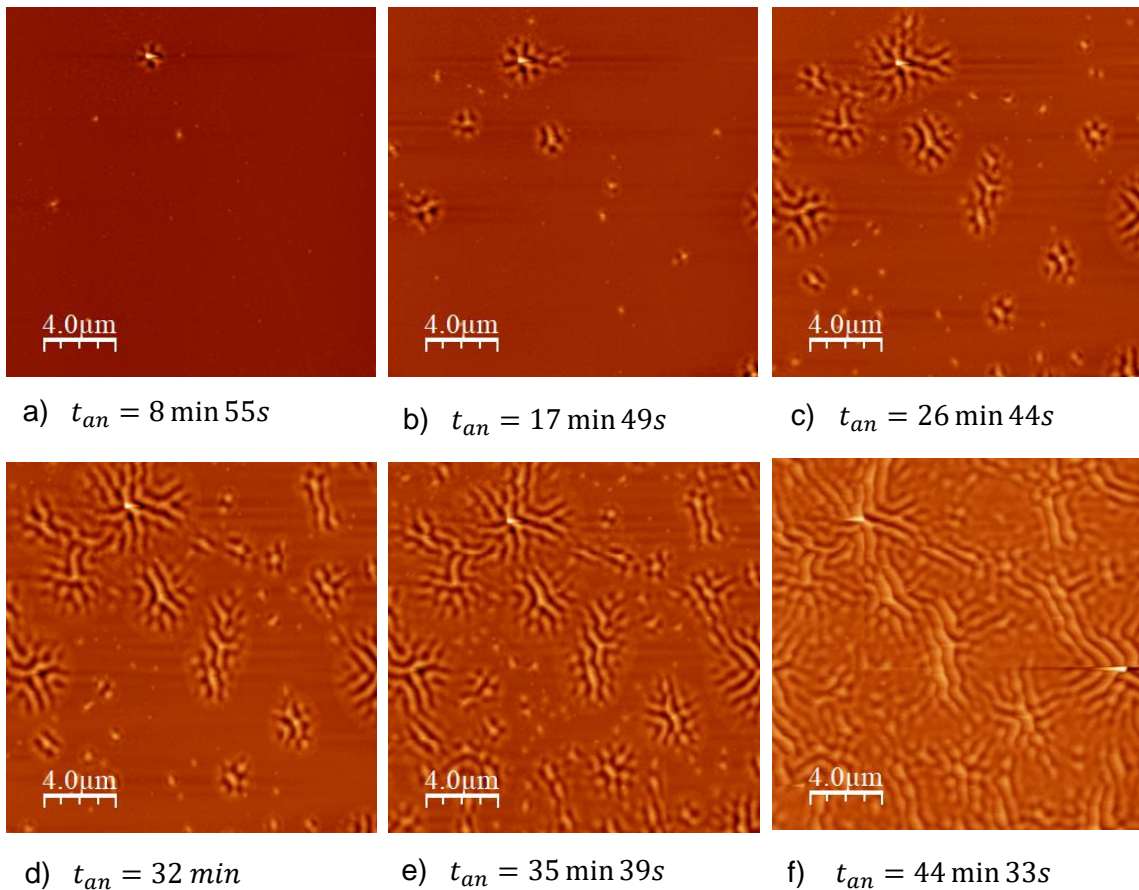


Figure 6. 2. Topography images of $20 \times 20 \mu\text{m}$ taken by AFM at different annealing times during an isothermal annealing at T_g+18K . The acquisition time for each image is around 4 min. The times indicated under each image correspond to the total annealing time at T_g+18K once the image was acquired.

The images reveal the appearance of corrugated regions in different parts of the sample that grow until they merge with each other forming a wrinkling pattern that extends throughout the whole surface of the film by the end of the isothermal annealing. The corrugation of the film can be seen to start locally, in specific regions, as a Gaussian-type protuberance with a height profile several nanometers higher than the rest of the film (see Figure 6.3a) and with aspect ratios around 100, that is a few nm high and few hundred nm wide. Upon holding the annealing temperature, this corrugation grows radially from the initial seed giving rise to a wavy pattern with a certain periodicity. Temporal evolution of the surface pattern obtained experimentally is shown in the insets of Figure 6.3.

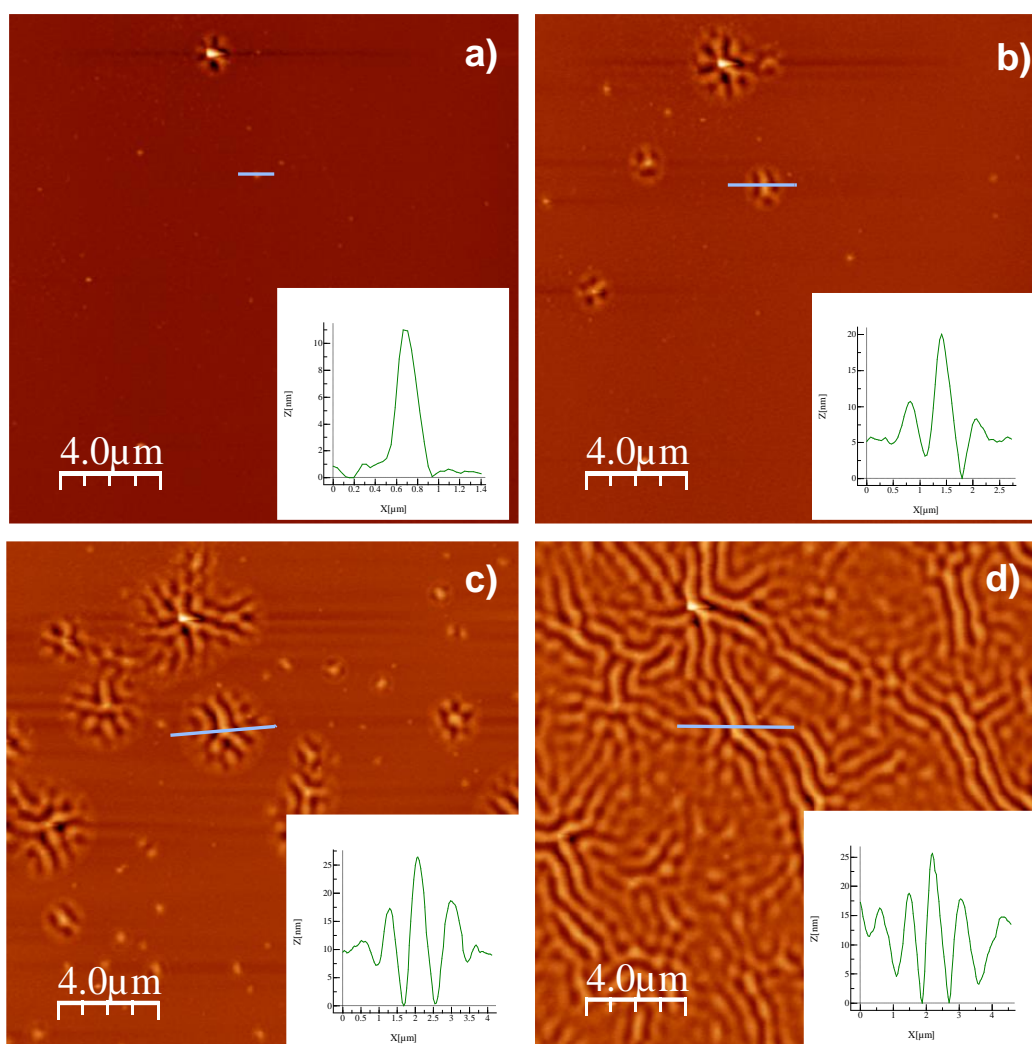


Figure 6. 3. AFM topography images ($20\mu\text{m}\times 20\mu\text{m}$) of a TCTA/TPD/TCTA sample annealed at $T_g+18\text{K}$ for different annealing times (a. 8min 55s, b. 17min 49s, c. 32min and d.44min32s). The insets show the height profile of one of the wrinkled regions and its evolution with time.

Looking at the height profile, it is interesting to note that the feature in the center of the wrinkling regions is always higher than the rest of the film. The amplitude of this central peak evolves from 2-3 nm in the initial stages of the perturbation to around 25-30nm (peak-to-valley) at the end of the wrinkling process, depending on the observed wrinkling pattern. The wrinkling pattern as well as these higher central features can also be observed via SEM images as shown in Figure 6.4, where the brighter spots correspond to these higher regions measured with AFM which constitute the initial stages of the wrinkling sites.

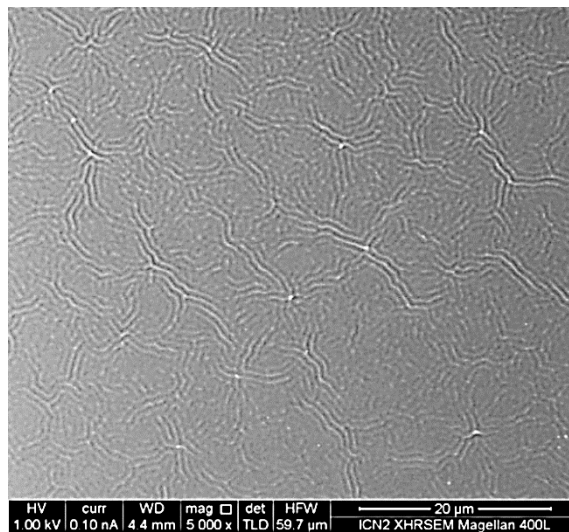


Figure 6. 4. Scanning Electron Microscopy (SEM) image of a TCTA/TPD/TCTA sample vapor deposited at 285K and annealed for 60min at T_g+18 K.

From Figures 6.3d and 6.4 we can also observe that the waves in the wrinkling pattern present a clear periodicity, which remains approximately constant over time with an average value of 815 ± 30 nm (obtained from the power spectrum analysis of the FFT image), and an amplitude that decreases from the higher initial site (center of formation) to the lower edges of the wrinkled region (see insets in Figures 6.3). The periodicity in the wrinkling patterns has shown to depend on the film thickness, prompting larger periodicities for thicker films [8]. The emergence and growth of the wrinkled regions in Figures 6.2 and 6.3 could resemble a surface crystallization process. In order to discard that this phenomenon is related with the appearance of the crystal phase, Grazing Incident X-ray Diffraction (GIXD) and Transmission Electron Microscopy (TEM) measurements were performed. Figure 6.5a shows how the X-ray diffraction spectra for the

TCTA/TPD/TCTA stack of a fully transformed sample presents no diffraction peaks, indicating the tri-layer maintains its amorphous structure. In an analogous way, the diffusive halo obtained in the TEM images (Figure 6.5c) is characteristic of scattering from an amorphous material, confirming that there is no crystal phase present in the samples.

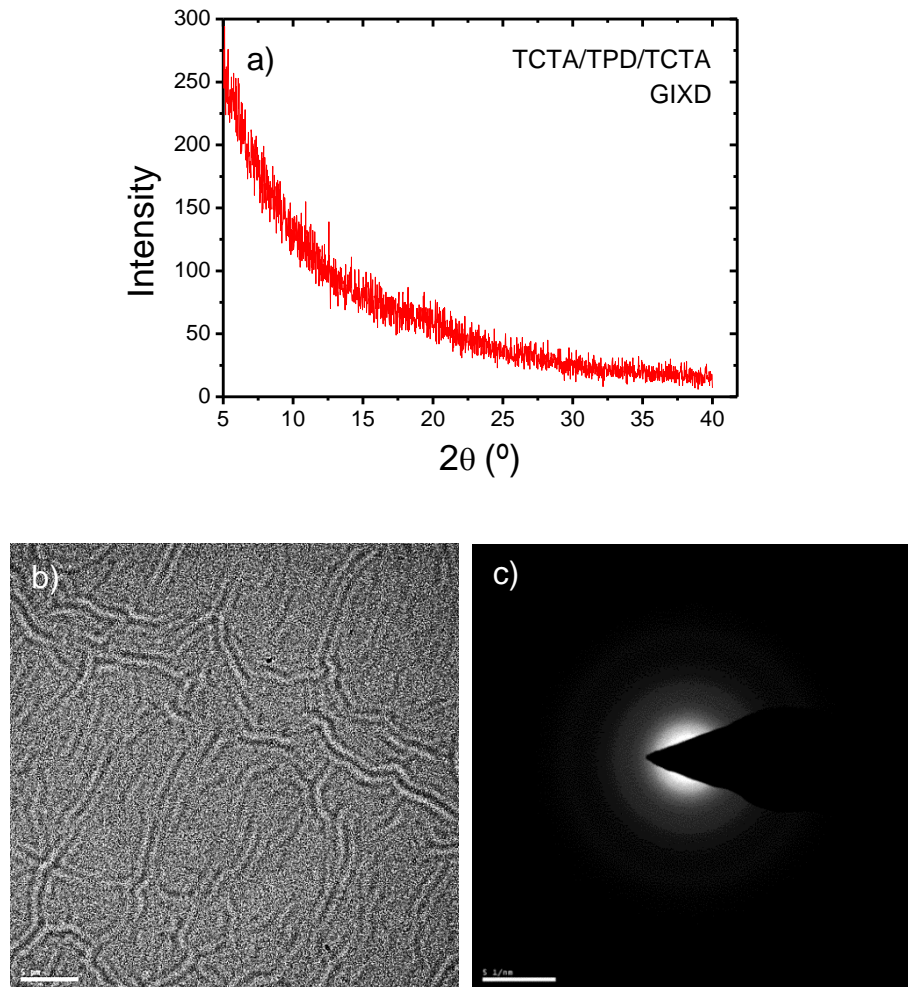
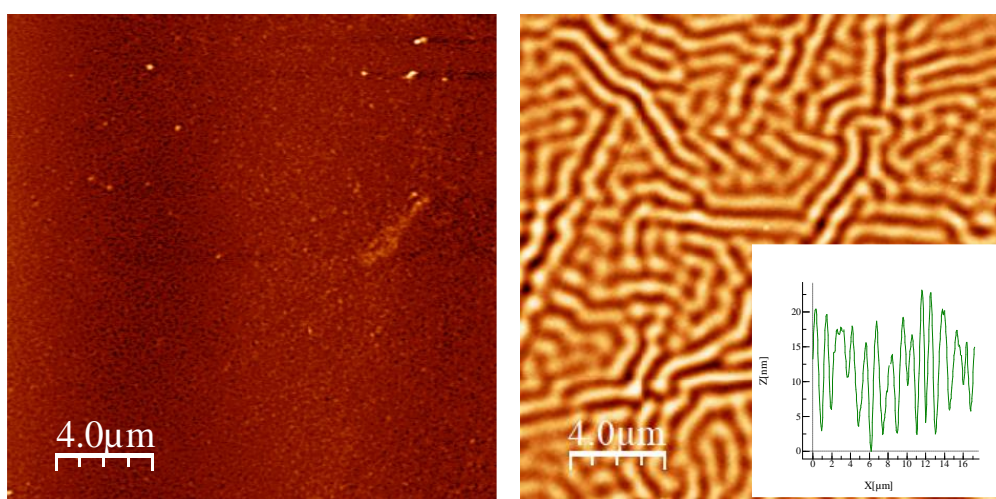


Figure 6. 5. Measurements performed to discard the presence of crystals in the samples under study by a) grazing incidence X-ray diffraction and b) & c) TEM measurements of a fully transformed TCTA/TPD/TCTA (13nm/63nm/13nm) sample. Image b) corresponds to the area of the sample we are measuring during the TEM study and c) corresponds to the diffraction pattern of the area depicted in b). The absence of diffraction peaks and the diffusive halo in this image indicate that there are no crystals in the studied samples.

It is also interesting to note that capping both sides of the middle TPD layer is required to observe localized patterns. TPD samples grown directly on Si substrates and capped

only on top by TCTA show wrinkling patterns that appear simultaneously in the whole sample and are present already from the beginning of the isothermal annealing (right upon reaching $T_g+18\text{K}$), as it can be observed in Figure 6.6. This is due to the different mechanism for the transformation of the TPD layer into the SCL, which in this case corresponds to a liquid front that starts at the TPD/Si interface and propagates from the Si interface towards the TPD/TCTA interface. This behavior is the one usually observed for thermal wrinkling in metal/polymer bilayers, where the polymer softens simultaneously in the whole sample [4,11].

Looking at the height profile in the inset of Figure 6.6b, one can see that the pattern is more homogeneous than the ones obtained with totally capped films and no regions with higher peaks are observed, indicating that the formation of the wrinkles has not started in localized sites but simultaneously on the whole surface of the film.



a) Room temperature ($\sim 300\text{K}$)

b) $T_g+18\text{K}$ ($351\pm 1\text{K}$)

Figure 6. 6. a) Si/TPD/TCTA sample at room temperature observed via AFM and b) wrinkling pattern observed by AFM after an isothermal annealing at $T_g+18\text{K}$ of a TPD sample capped by TCTA only on the free surface. The wrinkling pattern can be observed already from the first stages of annealing process in the whole surface, in contrast with the local wrinkling structures observed for totally capped glasses.

The changes in wrinkling patterns and transformation kinetics between totally capped and partially capped samples, together with the fact that the TCTA single layers show no topography changes at high temperatures, allow us to say with confidence that the appearance of surface wrinkles is related to the formation and growth of localized liquid regions in the intermediate TPD layer. Moreover, preliminary studies using finite element

model approaches [12] agree in that the initiation of local wrinkling is consistent with the appearance of liquid regions inside the glass. Thus, the images of Figure 6.2 can be considered a spatio-temporal mapping of the evolution of the structural relaxation of the TPD glass above T_g and, consequently, studying the corrugated regions we get direct access to the bulk transformation of highly stable thin film glasses.

6.3 Transformation kinetics from thermal wrinkling patterns

Analyzing Figure 6.2 we can observe that the transformation starts at localized regions that grow propagating across the whole film, in agreement with the transformation mechanism inferred by nanocalorimetry experiments in Chapter 5. Interestingly, the AFM images also show the appearance of new initiation sites or seeds as time evolves. Although we have not inferred a non-zero nucleation rate from the calorimetric studies presented in Chapter 5, these observations are compatible with previous experiments and theories, in which it was suggested that the bulk melting in highly stable glasses proceeds via a nucleation and growth type process (of the liquid regions inside the glass) with giant length scales between the initiation liquid sites [13–16].

The most noticeable feature in Figure 6.2 is the direct visualization of the large length scales (of around 2-4 μm) between initial seeds, which are in agreement with the values obtained using nanocalorimetry (see table 5.2) and also with previous estimations, where the giant length scales were inferred from the crossover length between front propagation and bulk melting [17,18]. We assume the formation of the liquid regions initiate at spatial locations with the highest mobility, that is, regions that upon annealing rapidly reach the equilibrium state. Whether these initial sites originate from an intrinsic distribution of relaxation times in the glass or due to the presence of defects in the sample is still an unresolved question that needs to be further addressed. The appearance of new protuberances or initial seeds as time progresses, indicates that the formation of new equilibrated regions is a time-dependent process and that we cannot consider the transformation to originate exclusively from a constant/fix number of nuclei, N , as was assumed in Section 5.4 when analyzing the evolution of the liquid fraction for ultrastable glasses.

A possible interpretation for the continuous appearance of newly equilibrated regions with annealing time is based on the continuous softening of the glass matrix during the thermal annealing process. As discussed in Chapter 5, the stable glass goes through a partial softening that changes slightly the stability of the remaining stable glass, as we've seen by the shift to lower temperatures of the endothermic peak corresponding to the remaining glass in the calorimetric studies. In this scenario, we can consider, initially, regions of fast mobility in the glass, spatially separated by large distances, which evolve towards the equilibrated liquid. Once these regions are equilibrated, they free adjacent regions of the glass that also become mobile by a kinetic facilitation mechanism [19]. After a certain time, regions of slower mobility also rejuvenate (due to the softening process) and reach equilibrium at longer times, appearing as newly equilibrated regions in the AFM measurements.

Although this is a plausible interpretation to explain the appearance of new equilibrated regions based on joint observations between AFM and nanocalorimetry measurements, other interpretations should also be considered. For instance, some theoretical views attribute the appearance of liquid regions to different origins. In the RFOT framework, for example, the equilibrated regions are a result of thermal fluctuations in certain regions of the glass [20]. The appearance or not of equilibrated regions, in this case, is a statistical probability and it is not explained strictly as a result of a softening process of the glass matrix. Further work needs to be performed to better understand the mechanism behind the emergence of these equilibrated regions.

6.3.1 Nucleation rate and growth velocity calculation

From the AFM images it is possible to extract an approximate value for the nucleation rate (understanding nuclei as newly equilibrated regions) and the growth velocity of the liquid regions. Each AFM image contains 512 scanning lines (considering trace and retrace movements) and each of these images takes 4 minutes and 16 seconds to be acquired. As a result, the time step between the first scanning line and the last one is non negligible and, therefore, assigning an average time to each image would imply having a significant uncertainty in the time variable when studying the transformation dynamics. In order to achieve a more precise estimation of the annealing time, each image has been divided into 16 sections (or cells) of $1.25 \mu\text{m} \times 20 \mu\text{m}$ with an elapsed time of 16 seconds

between them (see Figure 6.7). The time for each section can, therefore, be assigned knowing the initial and final time of each individual scan.

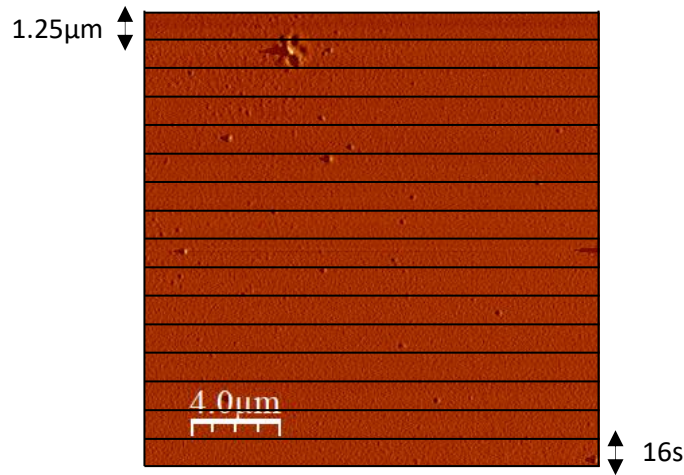


Figure 6. 7. Scheme of the time steps defined for each AFM image in order to account for better resolution of the time variable in the study of the transformation dynamics. The AFM images are divided in 16 sections of $1.25 \times 20 \mu\text{m}^2$ with a time interval of 16s each. The annealing time associated to each section is calculated as the mean value of the corresponding section's interval time.

To obtain an approximate value for the nucleation rate, we have identified and counted the number of newly formed equilibrated regions present in each of the 16 sections for the different AFM images. Note that for high transformed fractions new nuclei can't be properly distinguished due to impingement between wrinkled regions, therefore the maximum annealing time considered is around 50 min when most of the sample is transformed but the new equilibrated regions can still be properly identified.

On the other hand, to obtain the growth velocity of the liquid regions we selected several nuclei (a total of 11 for this study) and their size has been monitored over time until they started merging with each other, making it impossible to follow the growth any further. For both measurements we used the *WSxM* software which helped us to distinguish these nuclei from the rest of the film, especially during the first stages of the transformation, using topographic profile measurements. Figure 6.8 shows the number of nuclei per unit area in each of the 16 sections (Figure 6.8a) and the evolution of the diameter of the selected nuclei (Figure 6.8b) as a function of time.

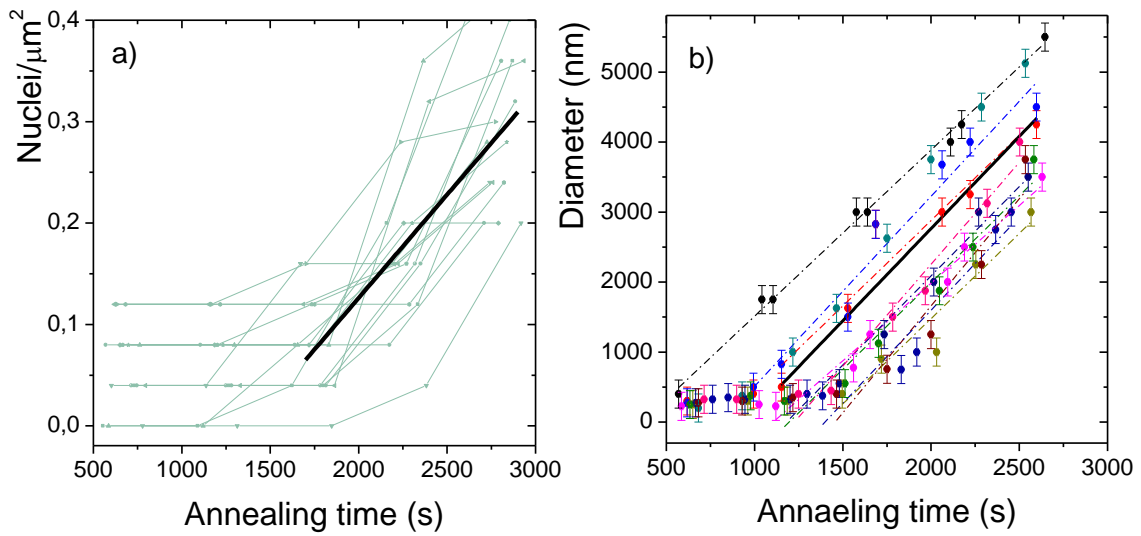


Figure 6. 8. a) Evolution of the number of nuclei per unit area as function of time for each of the 16 regions in which we divided every AFM image (see Figure 6.7). The solid green lines are a guide to the eye. b) Evolution of the diameter of the 11 selected nuclei as a function of time (each with a different color). The temporal uncertainty, $\sigma_t = \pm 8s$, is smaller than the symbol. Dashed lines correspond to a linear fit for each of the studied nuclei. Solid thick lines in both graphs correspond to the total averaged data for the corresponding graph.

Figure 6.8a shows how in the first stages of the transformation there is a small number of liquid regions or nuclei (around 6×10^{10} nuclei/ m^2 separated an average distance of $4.1 \mu\text{m}$) which remains initially constant. After a certain transient period, however, the number of nuclei per unit area starts increasing with annealing time. Averaging the data of Figure 6.8a in the range where the nucleation increases linearly, we obtain a value for the nucleation rate of $(2.3 \pm 1.5) \times 10^8$ nuclei/ (m^2s) .

The latency in the nucleation rate can be attributed to different origins. While it is consistent with the microscopic view of regions with different mobility inside the glass that start reaching equilibrium at different times due to the softening process during the isothermal annealing, the existence of defects on the substrate surface could also play a crucial role in the appearance of the small number of “pre-existing nuclei” during the first stages of the transformation. In this case, the first nuclei wouldn’t be related to a region of the glass with very low stability (high mobility) but to the existence of imperfections on the substrate surface, prompting the appearance of equilibrated liquid regions at times shorter than the ones needed for the glass to relaxed enough as to reach equilibrium. Although further studies need to be performed in order to understand this latency, recent

measurements seem to suggest that surface defects are of great importance when it comes to transformation dynamics [12].

We have also studied the time evolution of the size of the liquid regions as a function of time. In Figure 6.8b we analyze the growth of 11 different nuclei at low surface coverage to avoid any effect of overlapped stress. Averaging the values found for the different nuclei, a propagation speed of (1.4 ± 0.6) nm/s at T_g+18 K is obtained. This value is consistent with the growth front velocity of TPD single layers at the same temperature, $v_{gr} = (1.22 \pm 0.3)$ nm/s, evaluated independently from extrapolation of high T data (further detail on this calculation can be found in Chapter 7). Therefore, the wrinkling patterns propagate at a speed very similar to the liquid front underneath, indicating that the hypothesis we made in Chapter 5 (comparable velocities between the growth rate of the liquid regions inside capped glasses and the velocity of the propagating fronts in TPD layers) was reasonably accurate. The good agreement between both velocities can be considered another indicator that points towards the presence of liquid regions in the TPD layer as the cause of the origin of the wrinkling pattern.

Although the wrinkling pattern seems to grow radially on average, we cannot infer if local mobility spreads isotropically or through other geometries, such as following fractal dynamics. Actually, in the first stages of the transformation the corrugated areas seem to grow radially from the initiation sites, however for high transformation fractions it looks like the dynamics evolve forming branches that unify adjacent initiation sites.

The bulk transformation mechanism in ultrastable glasses, therefore, seems rather complex, mixing the existence of already pre-existing initiation sites with the emergence of new ones. In addition, these initiation sites, although propagating at similar velocities, do not start growing at the same time, presenting some of them a transient time before starting to grow, and others, propagating right away after their emergence. All these characteristics indicate that the analysis of the bulk dynamics of highly stable glasses using the KJMAE formalism, as we did for the calorimetric data in Chapter 5, is overly simplistic (transformation of the sample exclusively by growth of pre-existing nuclei or by the emergence of new regions that appear at constant frequency, constant growth rate and in a radial geometry). Thus, although the use of this type of models constitutes an interesting tool to study the transformation dynamics from calorimetric data, we cannot

rely on them for providing an accurate analysis of the phenomena involved in the transition.

6.4 Summary

In this chapter we've seen by means of AFM how localized thermal wrinkling is induced at the surface of capped TPD glasses when heated above its glass transition temperature. The observed wrinkling pattern is compatible with the emergence and growth of mobile regions in the TPD middle layer, which have been related with the appearance of equilibrated liquid patches inside the glass.

The main advantage of microscopy techniques such as AFM is that they allow a direct visualization of the changes happening in the sample in real time, making it a useful tool to obtain valuable information about the transformation process, difficult to infer otherwise. For instance, AFM measurements are behind the direct observation of the appearance of newly equilibrated regions with annealing time, while also allowing the observation of already existing initiation sites in the first stages of the transformation. Such complex behavior is not possible to infer only by means of nanocalorimetry and mean-field models such as the KJMAE formalism. By AFM measurements it was also possible to directly infer the growth velocity of these equilibrated regions, which correlates well with the growth front velocity of TPD at the corresponding annealing temperature. The good agreement between this propagation rate and the growth front velocity also supports the idea that the wrinkling pattern is directly related to the liquid formed in the TPD layer.

Maybe one of the most striking observations using AFM is the direct visualization of the large length scales between initial equilibrated liquid seeds (of the order of a few microns), which up to now were only inferred from indirect measurements, such as the estimations obtained from the crossover length between front propagation and bulk melting [17] or from the study of the evolution of the transformed fraction in capped TPD glasses using the Avrami model (see Section 5.4).

Although atomic force microscopy has shown to be a very useful technique to get insights on the transformation, it also presents some limitations, such as low time resolution (around 4 minutes are needed for each image), low heating and cooling rates (maximum

heating rate is 5K/min) and the difficulty to thermally stabilize the system in order to obtain good images and reduce the uncertainties in measured parameters, such as the height or lateral position, due to thermal strain. Since all these limitations hinder the systematic study of the transformation, this technique has been used exclusively as a complementary tool for the development of this work.

References

- [1] R. Huang, *Kinetic Wrinkling of an Elastic Film on a Viscoelastic Substrate*, *J Mech Phys Solids* **53**, 63 (2005).
- [2] N. Bowden, S. Brittain, A. G. Evans, J. W. Hutchinson, and G. M. Whitesides, *Spontaneous Formation of Ordered Structures in Thin Films of Metals Supported on an Elastomeric Polymer*, *Nature* **393**, 146 (1998).
- [3] N. Sridhar, D. J. Srolovitz, and Z. Suo, *Kinetics of Buckling of a Compressed Film on a Viscous Substrate*, *Appl Phys Lett* **78**, 2482 (2001).
- [4] P. J. Yoo and H. H. Lee, *Evolution of a Stress-Driven Pattern in Thin Bilayer Films: Spinodal Wrinkling*, *Phys Rev Lett* **91**, 154502 (2003).
- [5] J. Y. Chung, A. J. Nolte, and C. M. Stafford, *Surface Wrinkling: A Versatile Platform for Measuring Thin-Film Properties*, *Advanced Materials* **23**, 349 (2011).
- [6] E. Cerda and L. Mahadevan, *Geometry and Physics of Wrinkling*, *Phys Rev Lett* **90**, 74302 (2003).
- [7] J. Yin, Z. Cao, C. Li, I. Sheinman, and X. Chen, *Stress-Driven Buckling Patterns in Spheroidal Core/Shell Structures*, *Proceedings of the National Academy of Sciences* **105**, 19132 (2008).
- [8] N. M. Hoinka, C. Ostwald, and T. Fuhrmann-Lieker, *Two-Dimensional Wrinkle Resonators for Random Lasing in Organic Glasses*, *Sci Rep* **10**, 2434 (2020).
- [9] M.-W. Moon, S. H. Lee, J.-Y. Sun, K. H. Oh, A. Vaziri, and J. W. Hutchinson, *Wrinkled Hard Skins on Polymers Created by Focused Ion Beam*, *Proceedings of the National Academy of Sciences* **104**, 1130 (2007).
- [10] K. Mondal, Y. Liu, T. Shay, J. Genzer, and M. D. Dickey, *Application of a Laser Cutter to Pattern Wrinkles on Polymer Films*, *ACS Appl Polym Mater* **2**, 1848 (2020).
- [11] A. Das, A. Banerji, and R. Mukherjee, *Programming Feature Size in the Thermal Wrinkling of Metal Polymer Bilayer by Modulating Substrate Viscoelasticity*, *ACS Appl Mater Interfaces* **9**, 23255 (2017).
- [12] J. Alcalá, T. Bar, J. Fraxedas, M. Gonzalez-Silveira, J. A. Plaza, C. Rodriguez-Tinoco, J. Rodríguez-Viejo, M. Ruiz, A. Vila-Costa (in alphabetical order)., *Microscopic View of the Relaxation of an Ultrastable Glass*, (Submitted).
- [13] S. F. Swallen, K. L. Kearns, M. K. Mapes, Y. S. Kim, R. J. McMahon, M. D. Ediger, T. Wu, L. Yu, and S. Satija, *Organic Glasses with Exceptional Thermodynamic and Kinetic Stability*, *Science* (1979) **315**, 353 (2007).
- [14] M. D. Ediger, *Perspective: Highly Stable Vapor-Deposited Glasses*, *Journal of Chemical Physics* **147**, (2017).
- [15] C. Rodriguez-Tinoco, M. Gonzalez-Silveira, M. A. Ramos, and J. Rodriguez-Viejo, *Ultrastable Glasses: New Perspectives for an Old Problem*, *La Rivista Del Nuovo Cimento* **45**, 325 (2022).
- [16] R. L. Jack and L. Berthier, *The Melting of Stable Glasses Is Governed by Nucleation-and-Growth Dynamics*, *Journal of Chemical Physics* **144**, (2016).

- [17] K. L. Kearns, M. D. Ediger, H. Huth, and C. Schick, *One Micrometer Length Scale Controls Kinetic Stability of Low-Energy Glasses*, J Phys Chem Lett **1**, 388 (2010).
- [18] C. Rodríguez-Tinoco, M. Gonzalez-Silveira, J. Ràfols-Ribé, A. Vila-Costa, J. C. Martinez-Garcia, and J. Rodríguez-Viejo, *Surface-Bulk Interplay in Vapor-Deposited Glasses: Crossover Length and the Origin of Front Transformation*, Phys Rev Lett **123**, (2019).
- [19] A. S. Keys, J. P. Garrahan, and D. Chandler, *Calorimetric Glass Transition Explained by Hierarchical Dynamic Facilitation*, Proceedings of the National Academy of Sciences **110**, 4482 (2013).
- [20] P. G. Wolynes, *Spatiotemporal Structures in Aging and Rejuvenating Glasses*, Proc Natl Acad Sci U S A **106**, 1353 (2009).

Chapter 7

Effect of glass stability on the bulk transformation dynamics

As we already advanced in the introduction chapter, one of the advantages of physical vapor deposition is the possibility of tailoring the stability of the glass by modifying the deposition conditions, that is by changing the deposition temperature and the deposition rate we are able to obtain glasses with a wide range of stabilities. We can, therefore, take advantage of this versatility to study the bulk transformation in glasses of different stabilities following a similar strategy as the one followed with ultrastable glasses (see Chapter 5), but modifying the deposition conditions to alter the stability of the original glass.

The glass transition in non-capped thin film glasses of different stabilities has been already studied extensively by different authors [1–5]. In general, vapor-deposited glasses transit into the liquid phase via propagating fronts, which initiate at the surface/interface with the substrate and then propagate inside the bulk of the material at a constant rate. The propagation rate depends strongly on the glass stability [3,6,7]. The more stable the glass, the slower the velocity of the front. However, the overall temperature dependence of the front velocity has shown to be independent of the stability of the samples [3,6].

The propagating fronts dominate the transformation up to a certain thickness where the bulk transformation is eventually activated, becoming the fastest transformation mechanism (thus, dominating the transition to the liquid phase) [6,8,9]. Several studies have reported the strong dependency of this thickness (or crossover length) with the deposition temperature [6,8]. More stable glasses achieve thicker crossover lengths, while

for less stable glasses the bulk transformation mechanism starts at lower temperatures/times, dominating the transformation before the front has travelled a long distance [10,11]. In order to study the bulk in non-capped thin films, therefore, samples thicker than the crossover length need to be prepared. Still, if one wants to completely avoid the apparition of the surface/interface propagation fronts, the capping strategy is the more effective method [12,13] (see Chapter 4).

In this chapter, we use fast scanning nanocalorimetry to study the bulk transformation dynamics in thin film glasses of different stabilities when annealed at temperatures well above T_g . We take advantage of the suppression of the surface/interface propagating front by capping the TPD thin films with TCTA to access the bulk transformation in glasses vapor deposited at five different temperatures ranging from 285K to 325K (that is $0.85T_g$ to $0.98T_g$). Analogously to the study in Chapter 5, where we presented the analysis of the bulk transformation in ultrastable glasses, in this chapter we study the dynamics of the bulk glass transition by means of nanocalorimetry, analyzing mainly the evolution as function of time of the equilibrated liquid that forms in the samples after an isothermal annealing at T_g+14 K during different annealing times. We will also pay attention to the changes in the glass matrix during the annealing, which is more prompted to softening due to a lower initial stability.

7.1 Preparation of the samples and thermal protocol

For this study, 63nm thick TPD films have been vapor deposited at five different temperatures and capped with 13nm thick TCTA layers on both sides of the sample ensuring the suppression of the front and the access to the bulk transformation mechanism in glasses with different stabilities. The glasses have been grown at a deposition rate of 0.08nm/s and at the deposition temperatures 285K, 305K, 310K, 315K and 325K (i.e., ranging from $0.85T_g$ to $0.98T_g$ for the TPD film). Both TPD and TCTA are deposited at the same temperature to avoid changes in the TPD glass during the deposition process.

After the samples are deposited, they are heated up to T_g+14 K in order to study the devitrification of the film following a similar thermal protocol as the one used for the ultrastable capped films in Chapter 5 (see Section 5.1). Briefly, the samples (TCTA/TPD/TCTA) are grown at the set deposition temperature, followed by a fast up

jump (around 100 K/s) to $T_{ann}=347$ K, 14K above the nominal T_g (333 K) of the conventional glass, for times ranging between 1s and 8h, depending on the stability of the glass. After the isotherm, the film is passively cooled at ~ 500 K/s down to 200 K and right after a fast scan at 3.5×10^4 K/s is performed in order to record the calorimetric trace in the glass transition region, therefore, the calorimetric traces reflect the state of the glass after partial transformation at T_{ann} and an immediate fast cooling down to 200 K.

7.2 Calorimetric measurements

The heat capacity traces obtained for the capped TPD glasses after isothermal annealings at 347K (T_g+14 K) for different times can be seen in Figure 7.1. All curves, regardless of the stability of the initial glass, show similar features as the ones found for capped ultrastable glasses in Chapter 5, namely, the apparition of a low temperature glass transition peak, at around 375K (Fast Cooled glass, FC), that increases in area with longer annealing times, and a shift to lower temperatures of the glass transition calorimetric peak corresponding to the initial stable glass (transition peak at high temperature, between 402K and 432K). These features are a signature of a transition into the supercooled liquid that proceeds via two parallel processes: i) the formation of equilibrated liquid regions inside the glass which grow consuming the more stable glass and, ii) the partial softening of the initial (more stable) glass, that loses stability as the annealing treatment proceeds. The feature at higher temperatures (around 440K) corresponds to the glass transition of the TCTA layers which remain unchanged during the isothermal treatments. The contribution of the heat capacity of glassy TCTA has already been subtracted in the curves presented in Figure 7.1 (see Section 4.2 for details). Therefore, the calorimetric curves only show the contribution to heat capacity of TPD, at least until the glass transition of the TCTA films.

As already discussed in Chapter 5, the transition peak at lower temperatures in Figure 7.1 ($T_{peak}^{FC} = 375$ K), corresponds to the regions of the sample that have transformed into the liquid phase during the isothermal treatment and then vitrified again upon fast cooling (forming the FC glass). Since the FC glass is obtained identically for all the samples, by passively cooling at 500 K/s from the same annealing temperature (T_g+14 K), the endothermic peak remains at a constant position, at a temperature around 375K. This is

not the case for the as-deposited glasses, whose onset of devitrification depends strongly on the deposition temperature and shifts to significantly lower temperatures for low stability glasses ($T_{peak}^{SG} = 433\text{K}$ for glasses deposited at $0.85T_g$ vs. $T_{peak}^{SG} = 402\text{K}$ for glasses grown at $0.98T_g$) as it can be seen in Figure 7.1a. As a consequence, the distance between the endothermic peaks of the as deposited and the fast-cooled glasses is highly reduced for the low stability samples, starting at $\Delta T = 53\text{K}$ (where $\Delta T = T_{peak}^{SG} - T_{peak}^{FC}$) for ultrastable glasses and decreasing to barely $\Delta T = 25\text{K}$ for glasses deposited at 325K . The distance between the two peaks decreases even more when the peak corresponding to the glass transition of the stable glass starts shifting to lower temperatures. This reduction of the temperature interval between both peaks results in the overlap of the as deposited and fast cooled devitrification curves for glasses with low stabilities, hindering the study of the transformation dynamics. In order to avoid the overlap and increase the separation between devitrification peaks, an interesting strategy would be cooling down the transformed liquid phase at a faster pace, this way the FC glass would shift to even lower temperatures, increasing the separation between peaks. However, faster cooling rates are not accessible with our experimental set up.

In addition to the overlap of the endothermic peaks, the drastic decrease of the total transformation times as the deposition temperature is increased (going from 8h for the ultrastable glass to 25s for the glass deposited at 325K) constitutes another factor that hampers the study of the bulk transition in glasses with low stabilities. In this sense, with our experimental set up, annealing treatments shorter than 1s cannot be measured accurately, thus limiting the study of low stability glasses during the first stages of the transformation.

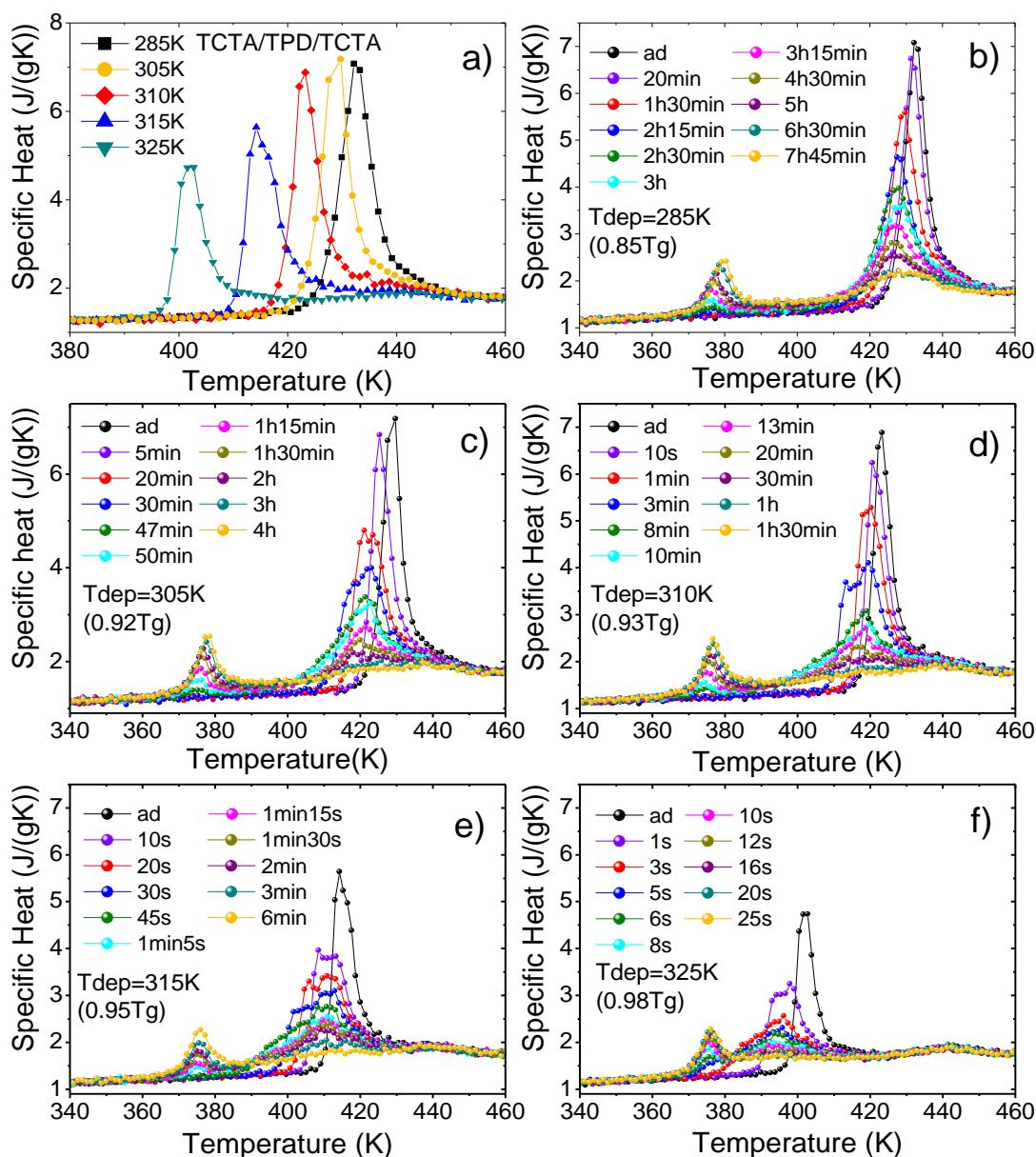


Figure 7. 1. a) Calorimetric traces obtained during a heating ramp at 3.5×10^4 K/s of as deposited capped TPD glasses (TCTA (13nm)/TPD (63nm)/TCTA (13nm)) obtained at different deposition temperatures (indicated in legend). The highest stability is found for the glass deposited at 285K (0.85T_g) while the less stable is the one grown at 325K as expected [2,14]. b-f) Specific heat curves obtained during heating ramps at 3.5×10^4 K/s of the same glasses shown in a) after thermal treatments at $T_g + 14K$ during different intervals of time. The deposition temperature and the annealing times are indicated in the corresponding legends. “ad” stands for “as deposited” and refers to a glass that has not been previously annealed.

7.3 Formation and growth of the liquid regions

From the calorimetric curves shown in Figure 7.1, it is possible to extract the fraction of equilibrated liquid phase formed during the isothermal annealing by analyzing the evolution of the FC glass calorimetric peak as described in Section 5.2.1.

Figure 7.2 shows the liquid fraction of TPD present in the glass matrix as a function of annealing time for the different stability glasses shown in Figure 7.1. A rapid look to Figure 7.2a allows us to see that all the transformed fractions follow the same sigmoidal like behavior independently of the glass stability. In fact, normalizing the data by t_{trans} (time required to transform the whole sample), results in the overlap of all the curves into a single master curve (Figure 7.2b), indicating that the transformation mechanism is the same for all the samples. It is important to highlight the importance of this observation since it implies that even though the transformation rate changes (the transformation takes place significantly faster for less stable samples), the physics behind the transformation mechanism is the same regardless of the stability of the glass.

We have already seen that the KJMAE model can constitute a useful tool for studying the transformation dynamics in capped glasses. By fitting the transformed liquid fraction as function of annealing time with the Avrami equation (Equation 5.9) we can get insights on the transformation mechanism through the Avrami exponent n and the Avrami constant K . It is important to note, however, that the Avrami model can only be used as a tool to infer, always in an approximate way, the main parameters of the transformation. We need to be aware that the KJMAE formalism presents important limitations in the sense that the process described by this model, when using an integer Avrami exponent, is highly simplistic (considering either constant nucleation rate or fixed number of initial nuclei, constant growth velocity, etc.) as we already remarked in Chapter 5. For example, the Avrami model does not consider the softening of the glass matrix, which can have an effect on the growth rate [3,6,15] of the liquid regions specially for glasses with low stabilities, or takes into account a non-constant nucleation rate (which has been observed by the initial transient time in the AFM study). Therefore, although it can be a useful model to get a first insight view on the transformation mechanism, the absolute values should be taken merely as an approximation.

Representing the data of the overlapped curves in Figure 7.2b in a $\ln(-\ln(1-x_l))$ vs. $\ln(t/t_{trans})$ plot (see Figure 7.2c), we are able to graphically highlight the value of the average Avrami exponent, n , for the different samples as already detailed in Section 5.4. As it can be seen in Figure 7.2c two different tendencies can be clearly identified. For transformed fractions up to 50-60%, the data can be fitted with an exponent $n = 2.8 \pm 0.1$, while for higher transformed fractions the value of n seems to decrease. A possible explanation for this change in tendency is the temperature profile in our nanocalorimeters. As already highlighted in Chapter 5 (see Section 5.5), temperature inhomogeneities on the sensing area of the nanocalorimeter of just 3K can result in considerable delays of the total sample transformation. That translates in a flattening of the curve at longer times, since colder regions remain “frozen” for longer times.

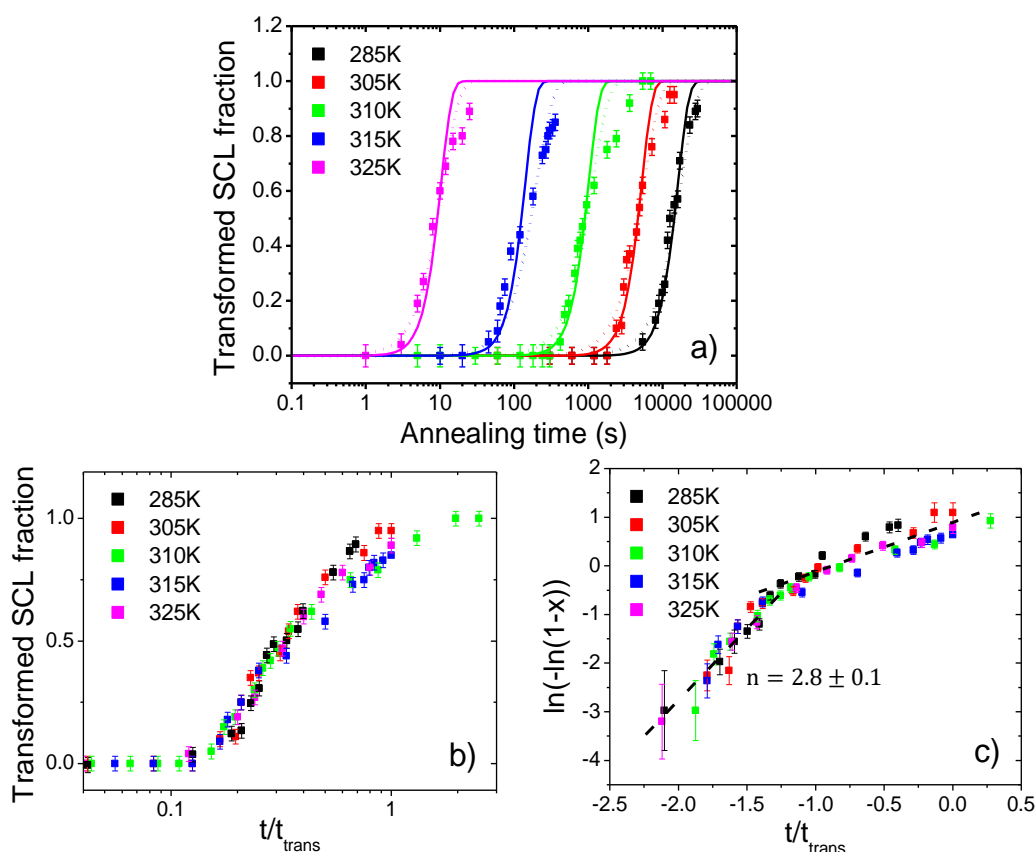


Figure 7. 2. a) Liquid fraction as a function of annealing time of glasses vapor deposited at five different temperatures, ranging from $0.85T_g$ (285K) to $0.98T_g$ (325K), at the annealing temperature of T_g+14K . Dashed and continuous lines correspond to KJMAE fittings imposing $n = 2$ and $n = 3$, respectively. b) Transformed liquid fraction of the glasses in a) normalized by t_{trans} . The overlap of the curves indicates that independently of the stability the physics behind the transformation mechanism are the same. c) $\ln(-\ln(1-x_l))$ vs $\ln(t/t_{trans})$ plot which helps to highlight the average Avrami exponent. Up to 60% of the transformation we obtain $n = 2.8$ while for higher transformation times the transformation rate seems to slowdown and the slope starts decreasing. The same trend can be observed in panel a).

An experimental value of $n = 2.8 \pm 0.1$ is consistent with a 2D growth with a certain nucleation frequency, in line with what it has been observed with AFM measurements. However, from the AFM images we could also infer the existence of transformation regions present in the sample since the first stages of the transformation at $t=0$ s (pre-existing nuclei), indicating that the emergence and growth of the liquid regions can take place via an intermediate mechanism. Therefore, it cannot be accurately described neither with $n = 2$ (2D growth from pre-existing sites, null nucleation rate) nor $n = 3$ (2D growth with uniform nucleation rate, no pre-existing sites). However, we can still use the KJMAE model to obtain a rough estimation of the number of initial transformation sites or nucleation frequency, as well as to compare the distance between liquid seeds in glasses with different stabilities. With that in mind the experimental data in Figure 7.2a is individually fitted with the KJMAE equation imposing $n = 2$ (dashed line) and $n = 3$ (continuous line). It is important to remark that since we know the later part of the transformation might be conditioned to a gradient in temperature or other unknown factors, to study the transformation dynamics, we just considered for the fittings the data corresponding to liquid fractions up to a 60% of the transformation. The best fitting parameter, K (which contains information on the main variables of the transformation such as nucleation rate, growth velocity and initial nucleation sites), can be found in Table 7.1 and Table 7.2 for $n = 2$ and $n = 3$, respectively. To extract further information about the nucleation sites from the fittings, it is necessary to introduce in the model the growth rate of the liquid regions (see Section 5.4 for more detail). As we have seen from the AFM measurements, in the case of the ultrastable glass, it is a quite reasonable approximation to consider that the liquid regions grow at the same rate than the liquid front that propagates from the surface/interface in non-capped films. However, the front velocity depends on the stability of the glass [5,15], so it will be necessary to determine the front velocity at the annealing temperature (T_g+14 K) for each of the stabilities under study. In the next section the procedure to obtain this information is detailed.

7.3.1 Evaluation of front velocity for glasses with different stabilities

In order to determine the front velocity in TPD glasses of different stabilities at T_g+14 K (347K), 90nm thick TPD films are grown at different deposition temperatures, ranging from 285K ($0.85T_g$) to 325K ($0.98T_g$), and right after they are heated up and held at 347K

($T_g+14\text{K}$) during different times (between 1s and 15min depending on the stability of the glass), following a thermal protocol analogous to the one described in Section 7.1. Figure 7.3 shows the resulting calorimetric traces. After the annealing treatment, the samples exhibit two clear heat capacity overshoots with different onset temperatures, the endothermic peak at higher temperature (between 398K and 410K) corresponds to the as deposited glass, while the peak at lower temperature ($T_{peak}^{FC}=375\text{K}$) corresponds to the part of the sample that has transformed into the supercooled liquid phase by propagating fronts during the isotherm and then vitrified again upon fast cooling after finishing the thermal treatment. Since the liquid front is the same in all cases, we obtain the same fast cooled glass transition peak regardless of the stability of the as-deposited glass.

From Figure 7.3 it can be seen that the less stable the glass, the faster the transformation into the supercooled liquid phase, in agreement with previous observations [3,6]. As it was already discussed in Chapter 4, these glasses transform via a single front that starts at the free surface of the sample and sweeps across the glass transforming the whole film, as long as the bulk transformation is not triggered. The propagation front velocity can be calculated from the experimental heat capacity curves by two different methods. In first place, we can obtain the front velocity at high temperatures from the up-scan of the as-deposited glass by solving the differential Equation 4.2 for $d_l(T)$. The derivative term in Equation 4.2 ($\Delta h \frac{d(d_l(T))}{dT}$) is, precisely, the transformation rate. Thus, the growth front velocity can be obtained directly from this transformation rate as [15]:

$$v_{gr}(T) = \beta(T) \frac{d(d_l)}{dT} = \beta(T) d_0 \frac{dx_l}{dT} \quad (7.1)$$

where $\beta(T)$ is the time dependent heating rate evaluated at each temperature, d_0 is the total thickness of the film and x_l is the fraction of the sample that has already transformed into the liquid phase. It is important to note that this calculation is only applicable to samples that transform exclusively by propagating fronts. Once the bulk transformation is triggered, this expression cannot be used to obtain accurate velocity values anymore.

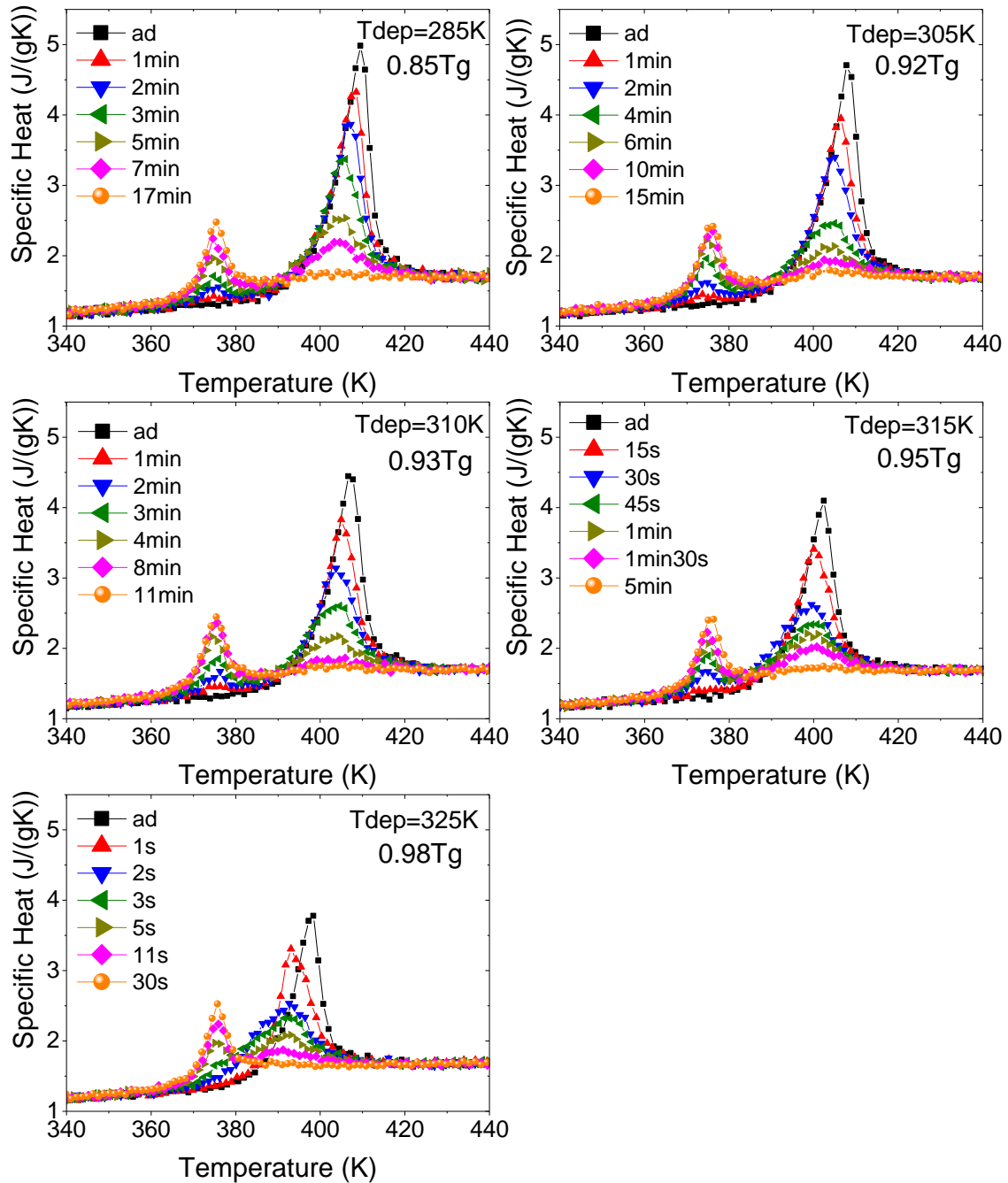


Figure 7.3. Specific heat curves of an up-scan at 3.5×10^4 K/s of 90nm thick TPD glass deposited at different temperatures (indicated in the figure) after thermal annealing at $T_g + 14K$ for different times (indicated in the legend). “ad” stands for “as deposited” and refers to a glass that has not been previously annealed.

As we have already seen in Section 4.1, one way to identify the front-like transformation mechanism is by applying and *ad-hoc* normalization to the heat capacity data of samples with different thicknesses. The superposition of the normalized curves indicates that all of them are transforming via a propagating front that is identical for all of them. The

growth front velocity, therefore, is taken from the temperature range where all the curves collapse (see Figure 7.4a). When solving Equation 4.2 to obtain the transformed liquid fraction, x_l , and the transformation rate, dx_l/dT , the only parameter that needs to be imposed to resolve this equation is the total excess enthalpy (Δh), which can be estimated imposing that the total transformed liquid fraction goes from 0, at the glass region, to 1, when the sample is completely transformed into the supercooled liquid phase. More details on this procedure can be found elsewhere [3,15].

Figure 7.4b (high temperature data set) shows the growth front velocity obtained at different deposition temperatures as a function of the alpha-relaxation time of the liquid, τ_α . The temperature dependence of τ_α is well-described by the VFT equation (Equation 1.2) with fitting parameters $\log(\tau_0/s) = -19.2$, $D = 13.5$, and $T_0 = 258.9K$ [5]. As it can be seen, the front velocity changes considerably with deposition temperature, being slower for the most stable samples (black solid squares, $T_{dep} = 285K$) and faster for the less stable ones (purple solid hexagons, $T_{dep} = 325K$). In addition, in this high temperature region, the velocities show the same trend with respect to the temperature (as it can be seen by the parallel straight lines with a common slope of $\gamma = 0.89 \pm 0.01$) independently of their stability, as it has been previously measured for other systems [3,6].

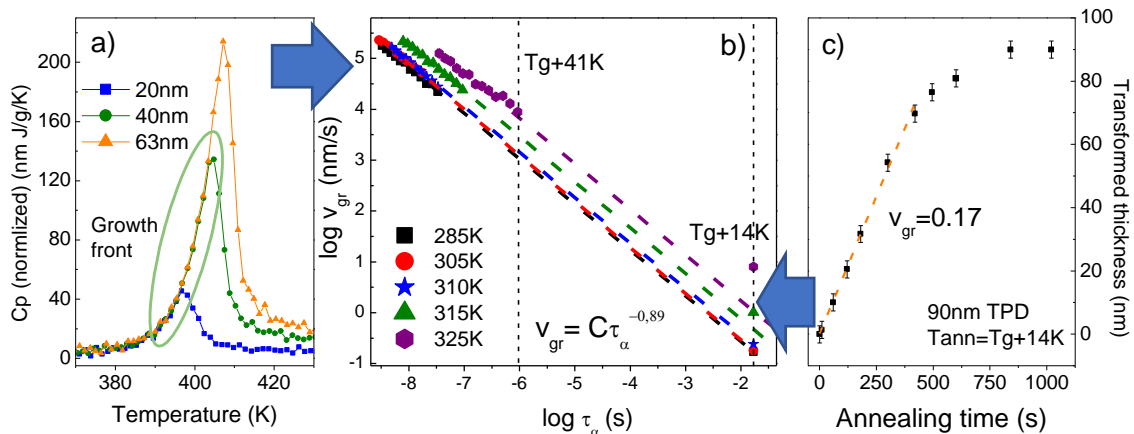


Figure 7. 4. a) Calorimetric traces normalized according to Equation 4.2 of TPD thin film glasses of three different thicknesses (20nm, 40nm and 63nm) vapor deposited at 285K ($0.85T_g$) and heated at 3.5×10^4 K/s. The light green circle highlights the interval of the heat capacity curves that overlap, indicating that the glasses are transforming via identical fronts regardless of the thickness of the sample. b) Front velocity as a function of the α -relaxation time of glasses with different stabilities for a wide range of temperatures. Temperature and τ_α are related by an VFT equation with fitting parameters $\log(\tau_0/s) = -19.2$, $D = 13.5$,

and $T_0 = 258.9K$ [5]. The high temperature data (low τ_α) is obtained using nanocalorimetry (panel (a)), while the low temperature data (high τ_α) is obtained from isothermal annealings at T_g+14K (panel (c)). The vertical black dashed lines indicate the temperature corresponding to two different τ_α (one at high temperature and the other at low temperature). c) Thickness of the thin film TPD glass that has transformed into SCL during an isothermal annealing at T_g+14K as a function of annealing time. The velocity can be obtained from the slope during the first stages of the transformation. The red dashed line shows the best fit and the resulting growth front velocity.

Due to the high heating rates used in nanocalorimetry, the growth front velocities obtained using this first method are in a very high temperature range, starting at T_g+41K for the glasses deposited at 325K, as we can see in Figure 7.4b. Although it is possible to extrapolate the high temperature data to lower temperatures following the relation $v_{gr} = C\tau_\alpha^{-\gamma}$ [6,15], we can also measure the front velocity at T_g+14K (347K) by measuring the amount of liquid formed during the annealing treatment at that temperature and transforming these values into thickness of the liquid front, assuming the front propagation is the only active mechanism. Figure 7.4c shows the thickness of the liquid front as a function of time for a sample grown at 285K ($0.85T_g$) when annealed at T_g+14K . The slope of this curve is the growth front velocity, which in the case of the ultrastable glass ($T_{dep}=285K$) is $v_{gr} = 0.17 \pm 0.01 m/s$ at $T_g+14 K$.

Representing in Figure 7.4b the front velocity values obtained at T_g+14K for the different stability glasses (low temperature data set), we can observe that while the most stable glasses (deposited at 285K, 305K and 310K) follow the same trend with τ_α as the high temperature data, the growth rate for the samples deposited at 315K and 325K is significantly faster than expected. This can be explained by the low stability of these glasses in which the bulk mechanism is triggered before the whole sample can transform via the propagating front, as it can be seen in Figure 7.5 where we have plotted the evolution of the transformed fraction at T_g+14K for capped and non-capped films. As it can be observed, the bulk and front mechanisms are almost overlapped in the last stages of the transformation for the less stable glasses. The transformation is, therefore, accelerated and the value obtained is not representative of the real velocity of the growth front. In this case, the propagation rate at low temperature can be obtained by extrapolating the data from high temperature down to T_g+14K . Table 7.1 shows the growth front velocity obtained for glasses deposited between $0.85T_g$ and $0.98T_g$.

Table 7. 1. Growth front velocity for TPD glasses vapor deposited at five different temperatures. The velocity values for the samples deposited between 285K and 310K were obtained from the liquid transformed fraction during the isotherm while, for the less stable glasses (deposited at 315K and 325K) the velocity is calculated from the extrapolation of high temperature data. Uncertainties correspond to the square sum of the instrumental and statistical error for 285K, 305K and 310K samples. In the case of the samples deposited at 315K and 325K the uncertainty is estimated from the standard error in the extrapolation to lower temperatures of the high temperature data.

T_{dep} (K)	285	305	310	315	325
v_{gr} (nm/s)	0.17 ± 0.07	0.18 ± 0.04	0.24 ± 0.04	0.47 ± 0.05	0.93 ± 0.12

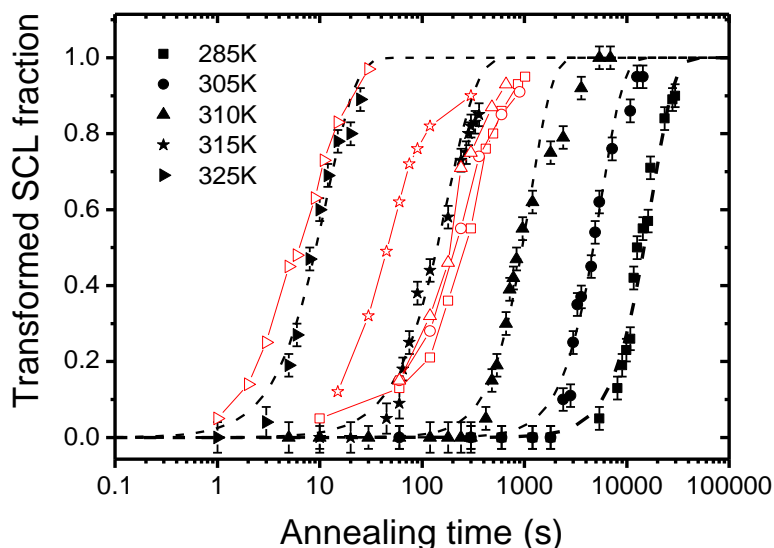


Figure 7. 5. Transformed liquid fraction as a function of time for TPD single layers (red open symbols) and capped TPD samples (black solid symbols) deposited at different temperatures after an annealing treatment at T_g+14K . Each type of symbol represents a different deposition temperature (indicated in the legend). The dashed lines are a guide to the eye. As it can be observed, for the most stable samples (285K-315K) thin films transform completely via the propagating front before the bulk mechanism is triggered. On the other hand, for samples deposited at 315K and 325K, the bulk transformation mechanism activates earlier while the front is propagating (a 20% of the sample has transformed via the bulk mechanism when the single layers have transformed into the supercooled liquid around a 60% and 30%, respectively).

7.3.2 Liquid nuclei formation dynamics

As shown in Figure 7.2a, the transformed fraction as a function of annealing time for capped glasses has been fitted with the Avrami equation imposing $n = 2$ and $n = 3$. For fittings with $n = 2$, the model assumes that the sample starts transforming in certain pre-existing equilibrated regions, which grow transforming the whole sample. This growth is two dimensional and no new nuclei appear during the transformation. The number of pre-

existing sites, N , can be calculated from the fitting parameter K as $N = K/\pi v_{gr}^2$ (as detailed in Section 5.4), where v_{gr} is the growth front velocity of the liquid at T_g+14K (see Table 7.1) and we are assuming circular geometry of the nuclei.

As it can be seen in Table 7.2, assuming the transformation takes place only via the growth of the pre-existing nuclei, the number of this pre-existing sites, N , would increase sharply as stability is decreased, showing values that differ 5 orders of magnitude between the glasses deposited in its most stable phase ($T_{dep}=285K$) and the ones grown at 325K. The sharp increase in initiation sites translates in an important reduction of the average spatial distance between them, $\langle d \rangle$, which ranges from around 5 μm for the glasses deposited at 285K to barely around 18nm for the ones grown at 325K. It is expected that growing samples substantially thicker than this average distance will result in films that show 3D growth. Further studies in this regard should be performed in order to see if indeed there is a crossover between 2D and 3D growth depending on the thickness of the films.

Note that the number of pre-existing transformation sites, N , is a function of $\propto K/v_{gr}^2$, where both the Avrami constant K and the growth velocity increase significantly when decreasing the stability of the glass. Therefore, one could expect these values to escalate in a similar way resulting in the number of initial equilibrated regions to remain constant or even decrease for low stability glasses. However, as it can be seen in Table 7.2 that is not the case, obtaining a significant larger number of liquid seeds in glasses with lower stabilities. This is compatible with simulation works [16,17] where it was reported that glasses with lower stabilities present a higher number of defects or mobile regions than those equilibrated at lower temperatures (therefore more stable).

Table 7. 2. Best fitting parameter K , number of pre-existing nuclei, N , and average distance between nucleation seeds, $\langle d \rangle$, for five different glasses vapor deposited between $0.85T_g$ and $0.98T_g$, obtained by individually fitting the experimental data in Figure 7.2a with the KJMAE equation (Equation 5.9) imposing $n=2$. Uncertainties correspond to the square sum of the instrumental and statistical error. Front velocity used for the calculations can be found in Table 7.1.

T_{dep}	n	K	N (Nuclei/m ²)	$\langle d \rangle$ (m)
285K	2	$(3.1 \pm 0.2) \times 10^{-9}$	$(3.5 \pm 0.4) \times 10^{10}$	$(5.4 \pm 0.3) \times 10^{-6}$
305K	2	$(3.0 \pm 0.2) \times 10^{-8}$	$(2.9 \pm 0.4) \times 10^{11}$	$(1.8 \pm 0.1) \times 10^{-6}$
310K	2	$(7.5 \pm 0.6) \times 10^{-7}$	$(4.2 \pm 0.5) \times 10^{12}$	$(4.9 \pm 0.3) \times 10^{-7}$
315K	2	$(2.4 \pm 0.3) \times 10^{-5}$	$(3.5 \pm 0.4) \times 10^{13}$	$(1.7 \pm 0.1) \times 10^{-7}$
325K	2	$(8.1 \pm 0.8) \times 10^{-3}$	$(3.0 \pm 0.2) \times 10^{15}$	$(1.8 \pm 0.1) \times 10^{-8}$

On the other hand, fitting the data in Figure 7.2a with the Avrami equation imposing $n = 3$, we are still assuming a two-dimensional growth, but in this case no pre-existing nucleation sites are considered and instead a constant nucleation rate that starts at $t=0$ s is the responsible of the transformation. That is, the transition is driven by the appearance (at a constant rate) of newly equilibrated regions, which grow propagating their mobility to adjacent areas of the sample. This perspective takes into account the nucleation rate observed in AFM measurements, where new liquid regions appeared as a function of annealing time. However, in the AFM images initial sites were also spotted, therefore it is important to remark the qualitative character of this calculation using the KJMAE model. By fitting the data with this model, we are obtaining only approximated values.

The nucleation rate, I , can be calculated from the fitting parameter K as $I = 3K/\pi v_{gr}^2$ as explained in Chapter 5 (see Section 5.4), where we are again considering circular nuclei. As it can be seen in Table 7.3 the nucleation rate increases fast when decreasing the stability of the glass, obtaining differences up to 8 orders of magnitude between the ultrastable glasses and the ones deposited at 325 K. This increase in nucleation rate translates in a higher number of equilibrated regions in the less stable glasses in the first stages of the transformation, following the same behavior as the one obtained for N when imposing $n = 2$.

In this case, the average distance between equilibrated liquid regions will decrease as a function of annealing time (since $I > 0$). To obtain a rough estimation of this average distance between liquid seeds at the first stages of the transformation, we have evaluated the number of nuclei when the transformed fraction reaches a 10% as $N_{x_l \sim 10\%} = I * t_{x_l \sim 10\%}$ (where $t_{x_l \sim 10\%}$ is the time when $x_l = 0.1$. Values detailed in Table 7.3). The calculation yields an average distance between liquid sites that ranges from around $4\mu\text{m}$ for the ultrastable glass to 16nm for the less stable glasses, distances that match well with the ones found for the $n = 2$ fitting. In an analogous way, if we analyze the distance between nuclei for the late stages of the transformation (90% transformed and above) the values obtained range from $2\mu\text{m}$ to around 6nm , indicating that, even at long annealing times, the distance separating the equilibrated regions is still huge in the case of ultrastable glasses, while for low stability glasses this distances are only of a few nanometers, in the order of the size expected for the cooperative rearranging regions [18].

Table 7. 3. Best fitting parameter, K , nucleation rate, I , and average distance between nucleation seeds at 10% of the transformation, $\langle d \rangle_{x_l \sim 10\%}$, of five different glasses vapor deposited between $0.85T_g$ and $0.98T_g$ obtained from fitting individually the experimental data in Figure 7.2a with the KJMAE equation (Equation 5.9) imposing $n=3$. Uncertainties correspond to the square sum of the instrumental and statistical error. Front velocity used for the calculations can be found in Table 7.1.

T_{dep}	n	K	I (Nuclei/m ² s)	$t_{x_l \sim 10\%}$ (s)	$N_{x_l \sim 10\%}$ (Nuclei/m ²)	$\langle d \rangle_{x_l \sim 10\%}$ (m)
285K	3	(2.3 ± 0.2) $\times 10^{-13}$	(7.8 ± 2.8) $\times 10^6$	7680	(6.0 ± 0.3) $\times 10^{10}$	$(4.1 \pm 0.1) \times 10^{-6}$
305K	3	(6.8 ± 0.7) $\times 10^{-12}$	(2.0 ± 0.7) $\times 10^8$	2404	(4.9 ± 0.2) $\times 10^{11}$	(1.4 ± 0.1) $\times 10^{-6}$
310K	3	(9.5 ± 1) $\times 10^{-10}$	$1.6 \pm 0.4)$ $\times 10^{10}$	464	(7.4 ± 0.4) $\times 10^{12}$	(3.7 ± 0.1) $\times 10^{-7}$
315K	3	(1.2 ± 0.3) $\times 10^{-7}$	(5 ± 1.3) $\times 10^{11}$	61	(3.0 ± 0.2) $\times 10^{13}$	(1.8 ± 0.1) $\times 10^{-7}$
325K	3	(8.9 ± 2) $\times 10^{-4}$	(9.8 ± 1.8) $\times 10^{14}$	4	(3.9 ± 0.2) $\times 10^{15}$	(1.6 ± 0.1) $\times 10^{-8}$

From the AFM measurements in Chapter 6, we know that the bulk transformation in thin films is rather complex, combining the presence of pre-existing liquid sites as well as a non-null nucleation rate, at least for highly stable glasses. However, the fact that in nanocalorimetric studies glasses with different stabilities have shown to follow the same dynamics (as it is observed by the overlap of all the transformed fraction curves in Figure 7.2b) allows us to assume that the bulk transformation in capped thin films takes place in the same way regardless of the stability of the glass. The Avrami exponent $n = 2.8$ obtained using the Avrami model also seems to agree with that interpretation (2D growth and positive nucleation rate). In addition, previous works also seem to point in the same direction, reporting that 3D systems with no defects transform into the liquid phase following nucleation and growth like kinetics with Avrami exponents $n = 4$ (i.e. 3D growth with uniform nucleation rate) [19,20]. These results seem to contrast with the transformation dynamics inferred for ultrastable samples in Chapter 5. In that case, we obtained an Avrami exponent $n = 2.1$ (for thin films) indicating the transformation was taking place following 2D growth from pre-existing nuclei with no nucleation rate. These differences may be explained by the presence of a bigger number of defects in the surface of the calorimeter used for the experiments in Chapter 5. The presence of more defects would translate into a higher number of initial nucleation seeds, N , which would completely transform the sample at a faster rate than the time needed for new liquid regions to be equilibrated. Therefore, showcasing a transformation with null nucleation rate, i.e., $n = 2$.

In order to better understand how the transformation takes place, whether or not there is always a mix of pre-existing liquid sites and a non-null nucleation rate, it would be interesting to perform AFM measurements of samples with different stabilities. Not only we would get a direct visualization of the new equilibrated regions, but also of their propagation rate. In the case of ultrastable glasses, we have seen that the propagation velocity obtained by means of AFM matches well the front velocity reported for thin films. For this study, therefore, we assumed the front velocity to be the same as the growth rate of the liquid regions inside the glass. However, the glass matrix goes through a progressive softening (further details in the following section) which may cause a change in the growth velocity as the remaining glass matrix loses stability. In this sense, AFM measurements would be of great help to test if significant changes in velocity growth are present due to the softening.

7.4 Softening of the glass matrix

We have seen that the transformation of capped thin films takes place via two competing processes: the emergence and growth of liquid regions and the softening of the remaining initial stable glass where, by softening, we mean the cooperative and progressive rearranging of the glass towards, in this case, the metastable supercooled liquid configuration. In the specific heat traces from Figure 7.1, this second process can be identified by the shift to lower temperatures of the peak corresponding to the glass transition of the not yet transformed TPD glass (T_{peak}^{SG} between 395 K and 433 K). In Figure 7.6 we reproduce the evolution of this peak as function of annealing time for the sample deposited at 285 K.

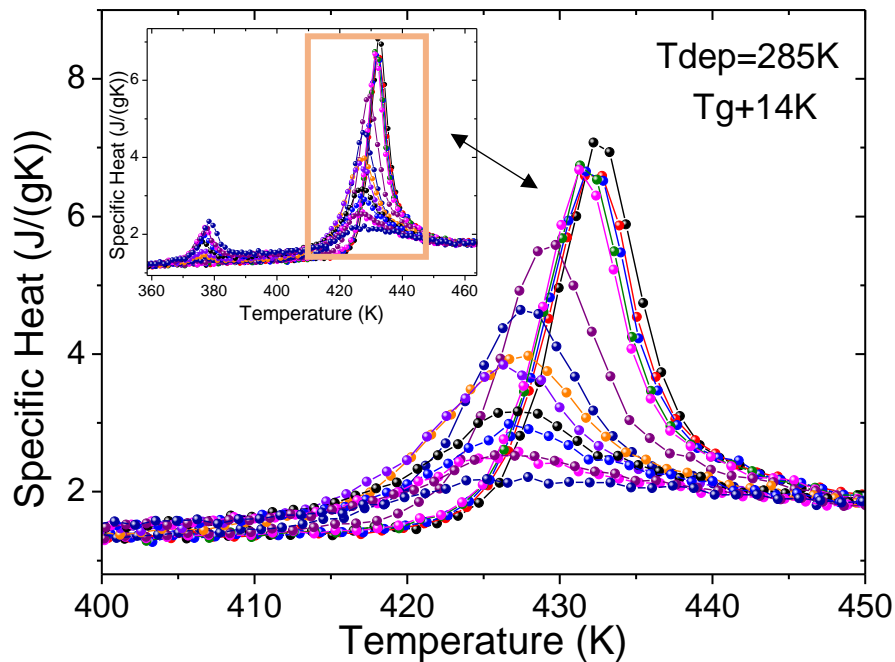


Figure 7. 6. Specific heat curves obtained during heating ramps at 3.5×10^4 K/s of capped TPD samples deposited at 285K ($0.85T_g$) after isothermal treatments at T_g+14 K during different intervals of time. The shift towards lower temperatures of the remaining stable glass indicates that the glass is losing stability with annealing time.

The shift to lower temperatures together with the reduction of the area under the peak observed in Figure 7.6 are clear indicators that the glass matrix is losing stability during the annealing process. Typically, the main parameters used to discuss stability in glasses are the limiting fictive temperature, T_f , related to the thermodynamic stability of the glasses, and the onset devitrification temperature, T_{on} , related to its kinetic stability (see

Section 1.5). However, in this case due to the complexity of the system: two different TPD glasses (stable and fast-cooled) and two TCTA layers, T_f and T_{on} are difficult to evaluate for the remaining TPD stable glass for the whole thermal treatment. Subtracting the TCTA layers and the TPD fast-cooled glass from the heat capacity data has proven to yield values of the fictive temperature and onset temperature with high uncertainties, especially for low stability samples, where there is an overlap of the two glass transition peaks for longer annealing times. Therefore, T_f and T_{on} are not suitable parameters to determine the stability in capped samples. However, we can work with an alternative, although not that reliable, indicator of the stability of the glass: T_{peak} (position of the devitrification peak's maximum). Figure 7.7 shows the dependence with deposition temperature of T_{on} , T_f and T_{peak} of the as-deposited glasses. The trend is very similar for the three temperatures, so we can use the position of the peak, T_{peak} , as an indicator of the stability of the glass.

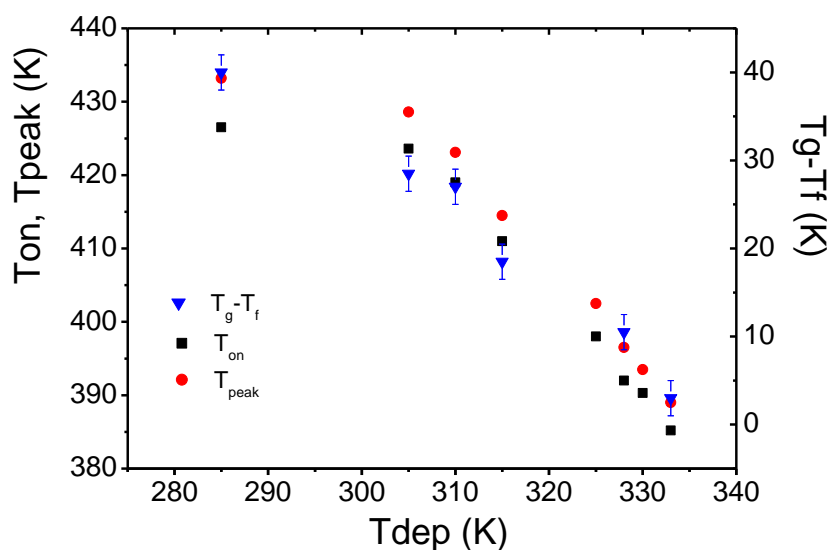


Figure 7. 7. Correlation between T_f , T_{on} and T_{peak} as a function of deposition temperature. These three parameters are indicators of glass stability. Since T_f , T_{on} and T_{peak} follow a similar trend with deposition temperature and the simplest one to determine in the calorimetric traces is T_{peak} , this temperature is chosen as the indicator of stability for our study. T_{on} and T_{peak} 's uncertainties are smaller than the symbol.

Figure 7.8a shows the evolution of T_{peak} as a function of annealing time for glasses with different stabilities. The graph is normalized by the peak position of the FC glass, T_{peak}^{FC} ,

which corresponds to the final position at which the peak would evolve to if the glass had transformed completely into the equilibrium supercooled liquid state by the softening process, without the emergence and growth of liquid regions. Looking at Figure 7.8a we notice that the evolution of the glass seems to be suddenly interrupted before reaching the final position (i.e. $T_{peak} = T_{peak}^{FC}$). However, the evolution is not stopping. Instead of a clear shift of the peak position, there is a broadening of the peak, with the low temperature side expanding towards a less stable glass (see Figure 7.8b). So the softening proceeds, but the peak position is not a useful indicator from that moment forwards.

Due to the presence of dynamical heterogeneities in the glass, with regions characterized by different relaxation times, the softening is expected to take place following a stretched exponential [21]. Fitting the data in Figure 7.8a with the Kohlrausch-Williams-Watts function (KWW), $f(t) = Ae^{-(t/\tau)^\beta}$ (dashed lines in Figure 7.8a), we obtain β exponents with values that range between $\beta = 0.7 - 0.8$, with no clear tendency depending on the deposition temperature. Note that the value obtained for the ultrastable sample (deposited at 285K), $\beta = 0.84$, is the one that presents a bigger deviation compared with the ones measured for the other stabilities. However, this deviation may be explained because of the slow evolution of this highly stable glass, which allows us to measure only a small range of T_{peak} before the glass is consumed by the equilibrated liquid regions, leading to a bigger uncertainty in the fitting parameters. We can consider, therefore, that all the samples relax in a similar manner with a stretching exponent given by the average value $\beta = 0.73 \pm 0.1$, which also yields good fittings for the experimental data (see Figure 7.8a dotted lines).

The stretched exponential function with a $\beta < 1$ is indicative that the glass matrix is indeed going through a relaxation process characterized by a cooperative rearrangement of the molecules with a broad range of time scales. Note that the values obtained for the exponent β are close to 1 (between 0.7-0.8), indicating a low dispersion in relaxation times of the vapor-deposited glasses regardless of the stability of the glass. These results agree with previous works in vapor deposited stable glasses of methyl-m-toluete where deviations of around 25% in the spatial distribution of the transformation times are reported inside the glass [22].

It is important to highlight that, to our knowledge, this is one of the first times the softening mechanism has been measured for stable glasses. Stable glasses transform into the supercooled liquid (when heated) mainly via propagating fronts that start at the free surfaces/interfaces in case of thin films non-capped glasses, and via the formation and growth of equilibrated liquid regions inside the glass matrix for capped samples. Although the softening in the glasses studied in this chapter is clearly not the main transformation mechanism, it is interesting to see that vapor deposited stable glasses follow a similar softening behavior as the already observed for conventional glasses, with the only difference being in their time scales.

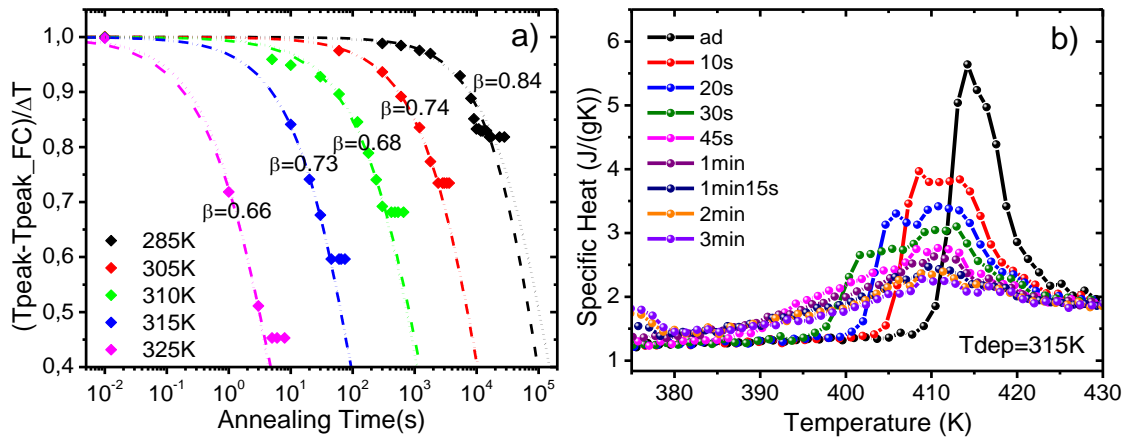


Figure 7. 8. a) Evolution of as a function of annealing time of the glass transition peak of the TPD stable glass remaining after isothermal treatments at $T_g + 14K$ in glasses of different stabilities. Dashed lines correspond to a fitting using the KWW expression with free parameters. Dotted lines correspond to KWW fittings imposing $\beta = 0.73$. b) Specific heat curves of TPD capped glasses deposited at 315K after isothermal annealings at $T_g + 14K$ during different intervals of time. The fraction of glass that does not transform into the supercooled liquid during the annealing goes through a softening process that can be observed by a shift in the onset temperature of devitrification. For long annealing times this shift seems to stop (T_{peak} starts to be constant), but the peak continues evolving broadening towards the low temperature region.

Comparing the real transformation time, t_{trans} (that is considering together the emergence and growth of liquid regions and the softening process) with the time that would require to transform a 90% of the sample only by softening, $t_{kkw90\%}$ (estimated from the KWW fittings as the time required to reach $(T_{peak} - T_{peak}^{FC})/\Delta T = 0.1$), we find that these two values become systematically closer the lower the stability of the glass. As it can be seen in Figure 7.9, the ratio $t_{kkw90\%}/t_{trans}$ decreases from 10 to 2.5 as we lower

the glass stability, indicating that a possible transition from a mix mechanism (emergence of liquid regions & softening) to a single mechanism (softening) might happen at lower stabilities. That means going from a transformation with clear phase separation between the liquid regions and the remaining glass to a pure cooperative relaxation with no presence of a well distinguishable liquid phase, as typically observed for liquid cooled glasses. Further details on this matter will be studied in the upcoming chapter.

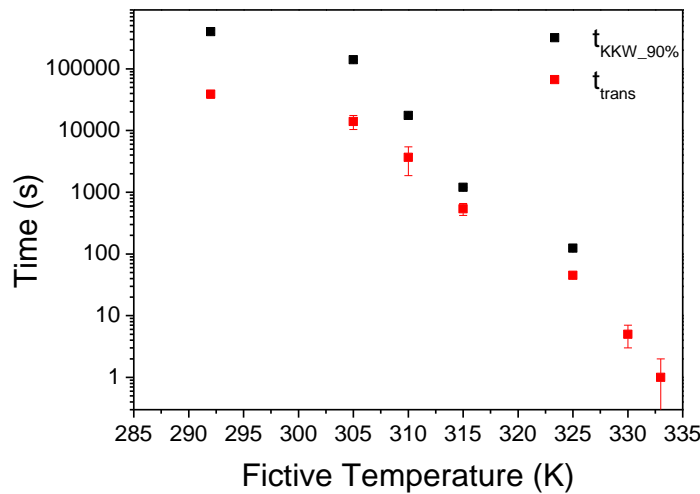


Figure 7.9. Transformation time, t_{trans} and time required to transform the 90% of the sample exclusively by softening, $\tau_{kkw90\%}$, as a function of the fictive temperature of the TPD layer. $T_f = T_{dep}$ for all samples except for the ultrastable glasses with $T_f=292K$. The lower the stability of the glass (higher fictive temperatures), the closer the values of these two relaxation/transformation times, indicating a change in the dominating process transforming the glass. For the glasses with lower stabilities ($T_{dep} = 330K$ and $T_{dep} = 333K$) the calculation of τ_{kkw} is extremely challenging due to the fast transformation rates and the difficulty in separating the two different transformation processes which almost overlap. Uncertainties correspond to the square sum of the instrumental and statistical error. The data that do not show uncertainties in the figure is because they are smaller than the symbol in the graph.

7.5 Summary

In this chapter we have seen how the bulk transformation in capped thin film glasses takes place mainly via a mechanism that shows a clear phase separation between the liquid and the remaining untransformed glass independently of the stability of the samples, even for glasses vapor deposited close to T_g . In particular, capped thin films transform into the supercooled liquid when heated well above T_g via two competing processes: the

formation of equilibrated liquid regions inside the glass that grow by means of kinetic facilitation and the progressive softening of the untransformed glass matrix.

As already observed in Chapter 5 for ultrastable glasses, the process that dominates the transition into the liquid phase is the formation and growth of the liquid regions, which can be studied by following the evolution of the fast-cooled glass transition endothermic peak in the calorimetric measurements. Using the KJMAE model to fit the transformed fraction data we found an Avrami exponent $n = 2.8 \pm 0.1$ which is consistent with a 2D growth of the liquid regions with a non-null nucleation rate. Although in this model $n = 3$ can also describe a transition in 3D with no nucleation rate, the direct visualization of new equilibrated regions in AFM measurements (see Chapter 6) together with the big length scales (in the order of microns for the most stable glasses) between nucleation sites compared with the thickness of our samples (63nm), allows us to assume confidently that the samples are transforming via a two-dimensional growth with a certain nucleation rate.

As we have already discussed along Chapters 5 and 6, the transformation is more complex than what is contemplated by the KJMAE formalism therefore, the values obtained for variables such as the initial number of nucleation sites or the nucleation rate must be considered only as a rough estimation of the real values. Considering this, we have found large differences in the average distance between initiation sites as a function of glass stability. We have found that while highly stable glasses present remarkable large dynamic length scales (2-5 μ m), in low stability glasses this distance is highly reduced to around 20nm.

Interestingly, although the dominating process in the glass transition of capped thin films is the formation and growth of the liquid phase, the progressive softening of the glass shows to gain importance the lower the stability of the glass. Thus, while the softening is almost negligible for ultrastable glasses (as we can see by the higher t_{trans}/τ_{KWW} ratio), it seems that it starts to play a more important role for glasses deposited at 325K (where the t_{trans}/τ_{KWW} ratio is 80% smaller than in the ultrastable glass case), hinting the possibility to have a crossover from a mixed mechanism (formation of liquid & progressive softening) to a single one (consisting of only progressive softening) for even less stable glasses, like it is usually observed in liquid cooled glasses.

References

- [1] S. S. Dalal, D. M. Walters, I. Lyubimov, J. J. de Pablo, and M. D. Ediger, *Tunable Molecular Orientation and Elevated Thermal Stability of Vapor-Deposited Organic Semiconductors*, Proceedings of the National Academy of Sciences **112**, 4227 (2015).
- [2] S. S. Dalal, Z. Fakhraai, and M. D. Ediger, *High-Throughput Ellipsometric Characterization of Vapor-Deposited Indomethacin Glasses*, J Phys Chem B **117**, 15415 (2013).
- [3] C. Rodríguez-Tinoco, M. Gonzalez-Silveira, J. Ràfols-Ribé, A. F. Lopeandía, and J. Rodríguez-Viejo, *Transformation Kinetics of Vapor-Deposited Thin Film Organic Glasses: The Role of Stability and Molecular Packing Anisotropy*, Physical Chemistry Chemical Physics **17**, 31195 (2015).
- [4] C. Rodriguez-Tinoco, M. Gonzalez-Silveira, M. A. Ramos, and J. Rodriguez-Viejo, *Ultrastable Glasses: New Perspectives for an Old Problem*, La Rivista Del Nuovo Cimento **45**, 325 (2022).
- [5] D. M. Walters, R. Richert, and M. D. Ediger, *Thermal Stability of Vapor-Deposited Stable Glasses of an Organic Semiconductor*, J Chem Phys **142**, 134504 (2015).
- [6] J. Rà Fols-Ribé, M. Gonzalez-Silveira, C. Rodrí Guez-Tinoco, and J. Rodrí Guez-Viejo, *The Role of Thermodynamic Stability in the Characteristics of the Devitrification Front of Vapour-Deposited Glasses of Toluene*, Phys. Chem. Chem. Phys **19**, 11089 (2017).
- [7] S. S. Dalal and M. D. Ediger, *Influence of Substrate Temperature on the Transformation Front Velocities That Determine Thermal Stability of Vapor-Deposited Glasses*, J Phys Chem B **119**, 3875 (2015).
- [8] C. Rodríguez-Tinoco, M. Gonzalez-Silveira, J. Ràfols-Ribé, A. Vila-Costa, J. C. Martinez-Garcia, and J. Rodríguez-Viejo, *Surface-Bulk Interplay in Vapor-Deposited Glasses: Crossover Length and the Origin of Front Transformation*, Phys Rev Lett **123**, (2019).
- [9] E. Flenner, L. Berthier, P. Charbonneau, and C. J. Fullerton, *Front-Mediated Melting of Isotropic Ultrastable Glasses*, Phys Rev Lett **123**, 175501 (2019).
- [10] E. Leon-Gutierrez, A. Sepúlveda, G. Garcia, M. T. Clavaguera-Mora, and J. Rodríguez-Viejo, *Stability of Thin Film Glasses of Toluene and Ethylbenzene Formed by Vapor Deposition: An in Situ Nanocalorimetric Study*, Physical Chemistry Chemical Physics **12**, 14693 (2010).
- [11] E. Leon-Gutierrez, A. Sepúlveda, G. Garcia, M. T. Clavaguera-Mora, and J. Rodríguez-Viejo, *Correction: Stability of Thin Film Glasses of Toluene and Ethylbenzene Formed by Vapor Deposition: An in Situ Nanocalorimetric Study*, Physical Chemistry Chemical Physics **18**, 8244 (2016).
- [12] A. Sepúlveda, S. F. Swallen, and M. D. Ediger, *Manipulating the Properties of Stable Organic Glasses Using Kinetic Facilitation*, J Chem Phys **138**, 12A517 (2013).
- [13] J. Ràfols-Ribé, A. Vila-Costa, C. Rodríguez-Tinoco, A. F. Lopeandía, J. Rodríguez-Viejo, and M. Gonzalez-Silveira, *Kinetic Arrest of Front Transformation to Gain Access to the Bulk Glass Transition in Ultrathin Films of Vapour-Deposited Glasses*, Physical Chemistry Chemical Physics **20**, 29989 (2018).
- [14] M. D. Ediger, *Perspective: Highly Stable Vapor-Deposited Glasses*, Journal of Chemical Physics **147**, (2017).

- [15] C. Rodríguez-Tinoco, M. Gonzalez-Silveira, J. Ràfols-Ribé, A. F. Lopeandía, M. T. Clavaguera-Mora, and J. Rodríguez-Viejo, *Evaluation of Growth Front Velocity in Ultrastable Glasses of Indomethacin over a Wide Temperature Interval*, J Phys Chem B **118**, 10795 (2014).
- [16] C. Scalliet, L. Berthier, and F. Zamponi, *Nature of Excitations and Defects in Structural Glasses*, Nat Commun **10**, 5102 (2019).
- [17] C. Scalliet, B. Guiselin and L. Berthier, *Thirty Milliseconds in the Life of a Supercooled Liquid*, ArXiv Preprint (2022).
- [18] M. D. Ediger, *Spatially Heterogeneous Dynamics in Supercooled Liquids*, Annu Rev Phys Chem **51**, 99 (2000).
- [19] K. L. Kearns, M. D. Ediger, H. Huth, and C. Schick, *One Micrometer Length Scale Controls Kinetic Stability of Low-Energy Glasses*, J Phys Chem Lett **1**, 388 (2010).
- [20] C. J. Fullerton and L. Berthier, *Density Controls the Kinetic Stability of Ultrastable Glasses*, EPL (Europhysics Letters) **119**, 36003 (2017).
- [21] P. G. Debenedetti and F. H. Stillinger, *Supercooled Liquids and the Glass Transition*, Nature **410**, 259 (2001).
- [22] M. Tyllinski, A. Sepúlveda, D. M. Walters, Y. Z. Chua, C. Schick, and M. D. Ediger, *Vapor-Deposited Glasses of Methyl-m-Toluate: How Uniform Is Stable Glass Transformation?*, J Chem Phys **143**, 244509 (2015).

Chapter 8

Crossover between softening and emergence of liquid regions

The bulk transformation mechanism in capped vapor-deposited glasses subjected to isothermal treatments above T_g has shown to take place via two competing processes: a partial softening of the glass matrix, via a cooperative relaxation mechanism, and the emergence and growth of equilibrated liquid regions inside the glass. As it was presented in Chapter 7, these two mechanisms have been observed regardless of the stability of the glass. However, while for highly stable glasses the transformation is clearly dominated by the growth of the equilibrated liquid regions and there is an almost negligible softening of the glass matrix, for glasses equilibrated at higher temperatures (therefore with lower stability) the softening process is far more significant.

In many theoretical [1,2] and simulation [3–7] approaches, the transition from glass to liquid at temperatures far above their fictive temperature (T_f) is found to happen via the emergence of liquid regions inside the glass. This is explained by the existence of spatial heterogeneous dynamics, that is, regions of the glass with different mobility. In all these approaches, regardless of the thermodynamic or kinetic origin of the appearance of the regions with enhanced mobility, the requirement to observe them is always a big contrast in mobility between the glass and the equilibrium liquid at that temperature.

For ultrastable glasses, the ratio between the average relaxation time of the glass and that of an equilibrated liquid region at temperatures close to T_g , τ_{glass}/τ_α , is expected to be very large (several orders of magnitude [8–10]). It has been previously shown that τ_{glass} is equivalent to t_{trans} and it can be understood as the time required to completely

transform the glass into the liquid state at a given temperature [9,11]. It is important to note that at T_f , $\tau_{glass}/\tau_\alpha \approx 1$. When an ultrastable glass is heated far above its fictive temperature, due to the large difference between the relaxation time of the glass and that of the liquid, according to all theoretical approaches, the emergence and growth of the liquid regions will be much faster than the relaxation of the glass and, therefore, it will dominate the transition of these highly stable glasses into the liquid. This is indeed what we have observed for ultrastable capped TPD glasses in Chapters 5 and 6, where the transformation was clearly dominated by the emergence of the equilibrated liquid regions inside the glass.

Following a similar reasoning, a glass with sufficiently low stability, i.e one cooled from the liquid at standard rates, could also experience the bulk transition into the equilibrated supercooled liquid by forming localized liquid regions at spots with short relaxation times provided there is sufficient mobility contrast with the adjacent regions [2,5]. The measurement strategy would be to shift the transition to temperatures much higher than its limiting fictive temperature, so the contrast in mobility between the liquid regions and the adjacent glass could be high enough for the formation and propagation of these liquid regions to be faster than the intrinsic relaxation of the surrounding glass. This assumption was already verified for surface front transformation, where experiments by Sadtchenko *et al.* [12] and Rodriguez-Tinoco *et al.* [10] showed that, at sufficient high heating rates and, hence, by shifting sufficiently the devitrification temperature of the glass, a liquid-cooled glass would also transform via front propagation.

In this chapter, we will study the glass transition in both vapor-deposited and liquid-cooled glasses to test the emergence of liquid regions during the transition depending on the stability of the glass and on the isothermal treatment above T_f . We aim to see if, in fact, given enough contrast in mobility between the glass and the equilibrated liquid, glasses can rejuvenate via the formation and growth of liquid regions independently of the stability and/or the route by which the glass is obtained.

8.1 Sample preparation and thermal protocol

For this study, we prepare capped TPD thin film glasses, with thicknesses of 63nm, from the vapor-phase at two different deposition temperatures: $T_{dep}=285\text{K}$ ($0.85T_g$), for the ultrastable glass ($T_f=292\text{K}$), and $T_{dep}=330\text{K}$ ($0.99T_g$), as a glass grown in equilibrium with the supercooled liquid and, therefore, with fictive temperature $T_f=330\text{K}$. The as deposited glass, grown in equilibrium with the supercooled liquid at this T_{dep} , is comparable to a glass obtained by cooling the liquid at a cooling rate around 1 K/min. We cap both sides of the TPD glasses with TCTA (13nm thick layers) to inhibit the formation of a liquid front at the surface/interfaces. On the other hand, we also obtain a liquid-cooled glass by depositing the TPD in the liquid state at $T_{dep}=338\text{K}$ (i.e. 5K above T_g) on top of a 13nm thick TCTA layer, we then cool it down to room temperature and finally, we anneal the resulting glass at $T_{ann}=319\text{K}$ ($T_g-14\text{K}$) for 96h until it is completely equilibrated at that temperature ($T_f=319\text{K}$). We cap it afterwards with TCTA again to avoid the front from appearing during thermal treatment. The reason behind the aging of this liquid cooled glass at $T_{ann}=319\text{K}$ is to ensure the glasses obtained by this method have enough stability as to distinguish the glassy phase (not transformed during the thermal annealing) from the possible fast cooled (FC) glass that appears when fast cooling the regions of the sample that have transform into the liquid phase. Otherwise, the endothermic peaks of the original liquid cooled glass and the FC glass would overlap due to the close stability between them. In addition, glasses with very low stabilities transform in very short time scales, preventing us from following the transition. Aging the glass also allows for the obtention of a glass with transformation times high enough to be experimentally monitored.

After deposition, the glasses are taken at fast-heating rate up to a certain temperature above the T_f of that specific glass and held there for different annealing times. During this annealing treatment, the glasses partially rejuvenate. We then cool down the sample to 200K at approximately -500 K/s and perform a subsequent fast heating ($\beta \approx 3.5 \times 10^4$ K/s) scan, following a protocol analogous to the one explained in Section 5.1. The heat capacity traces of the final fast up scan are, therefore, representative of the thermal history of the glass and, as seen before, will present two glass transition signatures if liquid regions have formed during the annealing: one at lower temperature, for the very low

stability glass (related to the newly formed liquid regions), and one at higher temperature, corresponding to the untransformed (or partially relaxed) glass.

8.2 Crossover between equilibrated liquid formation and cooperative relaxation

Figure 8.1 shows the specific heat curves for a low stability TPD glass deposited at $T_{dep}=330$ K ($T_f=330$ K) after isothermal treatments at 341 K (T_g+8 K) and 347 K (T_g+14 K) for different times. The transformation of this glass shows remarkable differences depending on the annealing temperature. Annealing at $T_{ann}=341$ K results in a shift of the glass transition peak towards lower temperature as time increases, indicating a progressive relaxation of the glass towards the equilibrium liquid at that specific annealing temperature. On the contrary, at $T_{ann}=347$ K we see both the relaxation of the as-deposited glass, by the shift of the original peak to lower temperatures, and the formation of distinct liquid regions in the glass that are manifested by the emergence of the second peak at lower temperature, identified by a green arrow in Figure 8.1a. This is a remarkable result. The same glass can experience different transformation mechanisms during the glass transition depending on the temperature at which the transformation takes place. Remarkably, even though both temperatures differ only by 6K, the contrast in mobility between liquid and glass is apparently different enough at these two temperatures to show distinct outputs when the transformation is partially fulfilled.

We propose that the appearance of equilibrated regions can be rationalized from the ratio between the relaxation time of the glass and the alpha relaxation time of the liquid (τ_{glass}/τ_α) at the temperature of the isothermal treatment. If this ratio is large, the nucleation and growth of liquid drops dominates the transition since on average the relaxation of the glass is slower than the rate at which the liquid emerges and consumes the sample. Contrary, small ratios are an indication that cooperative dynamics across the sample is fast enough to be the main active mechanism during the transition. To further analyze this assumption and provide a numeric estimation, we represent in Figure 8.1b the experimental transformation times of the glass deposited at $T_{dep}=0.99T_g$ as a function of temperature (green circles).

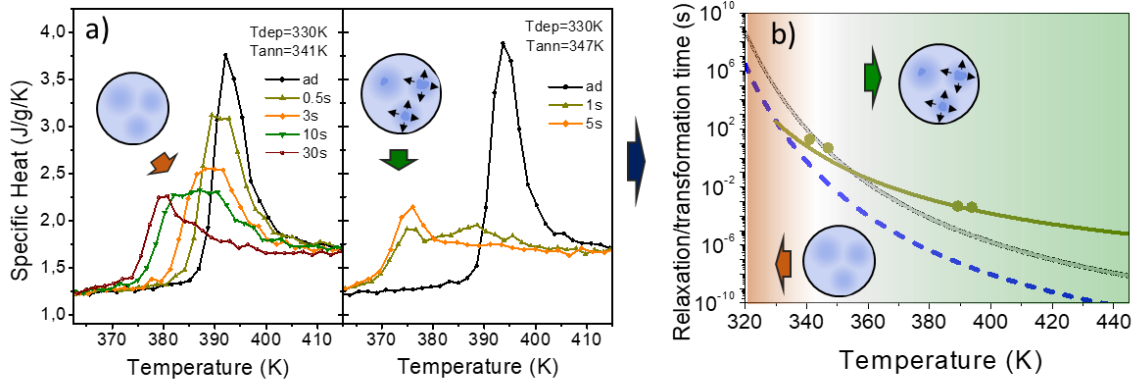


Figure 8. 1. a) Specific heat traces obtained at a scanning rate of 3.5×10^4 K/s after different annealing treatments of samples deposited at $0.99T_g$ (330K). The annealing temperatures and times are indicated in the legend. The endothermic peak that appears at lower temperatures is an indication of the formation of liquid patches in the glass during the annealing treatment. b) curves corresponding to the alpha relaxation time of the liquid (dash-blue) [13], the relaxation time of the glass (green), which depends on the limiting fictive temperature of the glass ($T_f=330$ K) and has been calculated according to Rodriguez-Tinoco *et al.* [9], and the line corresponding to the crossover relaxation time calculated as $\tau_{glass} = (180 \pm 60)\tau_\alpha$ (grey). Green dots correspond to experimental transformation time, calculated from the calorimetric curves as indicated in the main text. Uncertainties both in time and temperature fall inside the size of the dots. Regarding the background we find in orange the temperature regions for which a cooperative relaxation mechanism is expected for the glass transition. In green, the temperature region where we expect to find the nucleation and growth of liquid regions during the glass transition. The cartoons represent the two transformation mechanisms.

In order to calculate the experimental relaxation/transformation time of the glass at different temperatures we use the following methods. In the case of temperatures at which our glass transforms completely in laboratory timescales (from a few seconds to several hours), transformation times are directly obtained from the annealing times, considering the transformation time as the time at which the transformation is completed and there is no matrix glass remaining (no presence of the second calorimetric peak). Using this method, we obtain the two green circles at lower temperatures in Figure 8.1b. However, this method presents various limitations, for instance we can just measure transformation times at temperatures relatively close to T_g since for higher temperatures the transformation is too fast to be followed. To access the high temperature range, we can take advantage of fast scanning nanocalorimetry and its ultrafast heating rates that shift the glass transition to higher temperatures. In this case, the relaxation/transformation time of the glass can be inferred from the devitrification peak of the glass during a calorimetric scan and the heating rate achieved using two different approaches [9]:

- 1) The relaxation time at the devitrification onset temperature, T_{on} , can be inferred using the known relation $\tau_1\beta_1 = \tau_2\beta_2$ [12,14], which allows us to establish a relationship between the relaxation time of the glass and the heating rate of the experiment. As a reference, we use a value for the relaxation time of the glass of $\tau_1 = 100s$ for a heating rate of 10 K/min [15,16].
- 2) The transformation time of each glass at the maximum of the transformation peak can be estimated using the expression: $t_{trans}(T_{max}) = \Delta T/\beta_m$, where ΔT is the width of the transformation peak and β_m the mid value of the heating rate during the transformation.

Figure 8.2 shows the main parameters to calculate the relaxation/transformation time using the two approaches abovementioned.

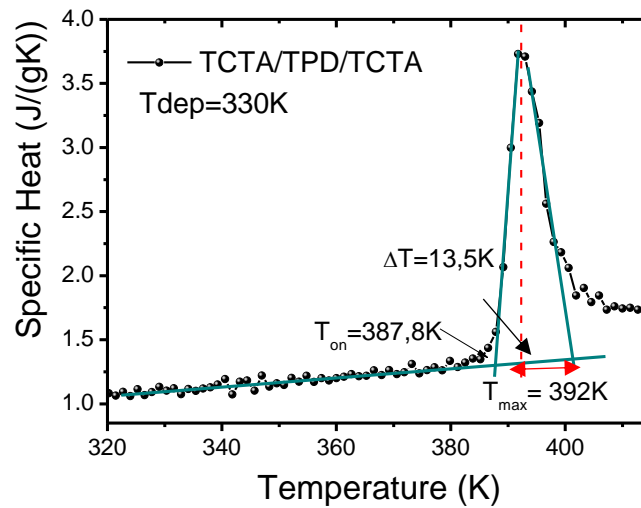


Figure 8. 2. Calculation of relaxation/transformation times from heat capacity data. In the first approach we use the expression $\tau_1\beta_1 = \tau_2\beta_2$ to obtain the relaxation time of the glass from the heating rate at the onset temperature and we obtain $\tau_2=2\times 10^{-4}$ s at $T=387,8$ K. Using the second approach, the transformation time is obtained from the width of the transformation peak and the heating rate and it is assigned to the temperature corresponding to the maximum of the transformation peak. The calculation yields $t_{trans}=3.8\times 10^{-4}$ s at $T=392$ K.

In graph 8.1b we have also plotted the alpha relaxation time of the liquid (dashed blue line) (extracted from [13]) and the relaxation/transformation time of the glass (green line) as a function of temperature calculated from [9]:

$$\tau_g = \tau_{g0} \exp\left(\frac{\xi(T_f)T_0}{(T-T_0)}\right) \quad (8.1)$$

This equation is a generalization of the well-known Vogel-Fucher-Tamman (VFT) equation [17] aimed at describing the dynamics of supercooled liquids and glasses with different thermal stability. In this equation all the parameters have an analogous meaning as in the VFT equation, where τ_{g0} is the limiting value of τ_g at an infinite temperature and T_0 is the diverging temperature. In this case, however, D (see Equation 1.2) has been substituted by a linear function of the limiting fictive temperature of the glass, $\xi(T'_f) = AT'_f + B$. In a supercooled liquid, the fictive temperature $T_f = T$ at all temperatures from the definition of T_f and one can recover the original VFT expression for the relaxation time of the liquid. More information on the validity of this equation can be found elsewhere [9]. We remark that the relaxation/transformation curve is not a fit and it is calculated considering exclusively the relaxation time of the liquid and the limiting fictive temperature of the glass.

In the particular case of the glass deposited at 330K, we see a change of mechanism in a very small range of temperatures, barely 6K in a temperature interval between 341K and 347K, so we assume that the crossover temperature between the two regimes, gradual cooperative softening (orange colored in the background of Figure 8.1b) and formation of distinctive liquid regions (green colored in Figure 8.1b), should be at a temperature between these two. For the annealing at $T_{ann}=341\text{K}$, $\tau_{glass}/\tau_\alpha \approx 60$, while at $T_{ann}=347\text{K}$, $\tau_{glass}/\tau_\alpha \approx 300$. As a rough estimation, we take the average between these two values as the crossover ratio. Figure 8.1b shows as a grey line this crossover relaxation time, $\tau_{glass,crossover} = (180 \pm 60)\tau_\alpha$. We use this value as a predictor to identify the temperature required to observe the formation of isolated liquid regions during the glass transition for a specific glass irrespective of its initial state. The transformation time at 341K falls to the left of the crossover line, while the one at 347K is at the right side, following what we see in the calorimetric traces, that for each temperature we have different transformation mechanisms.

The temperature of the crossover is somewhat ill-defined because of the difficulty to establish in this region a clear difference between both mechanisms in the heat capacity traces and therefore we represent it by a broad white-graded area (see Figure 8.1b). The drawings (together with the background color) in Figure 8.1b clearly illustrate the impact of the ratio τ_{glass}/τ_α on the transformation, and schematically represent the transformation at both sides, showing regions of liquid drops at the right (darker blue)

within a glassy matrix (softer blue), while in the left region the transformation is spatially less resolved.

A similar behavior has been observed in a glass cooled from the liquid. Figure 8.3a shows the specific heat traces of a glass deposited 5K above T_g (338K), cooled down and aged at 319K for 96h. This treatment led to full equilibration of the glass at this temperature, i.e. $T_f=319K$, before performing isothermal treatments at 347K (T_g+14K) and at $T_g - 5K$ (328K). Since both annealing treatments are above the glass' fictive temperature, in both cases the glass is expected to evolve towards the supercooled liquid, which means towards faster relaxation times [18]. As it can be seen in the calorimetric traces, during the annealing at 347K, distinguishable liquid regions are formed during the transition into the supercooled liquid. On the contrary, when the annealing is performed at 328K, there is a continuous shift of the glass transition overshoot, with no distinguishable fast-cooled glassy regions, and the transition takes place exclusively via a cooperative relaxation process (gradual softening).

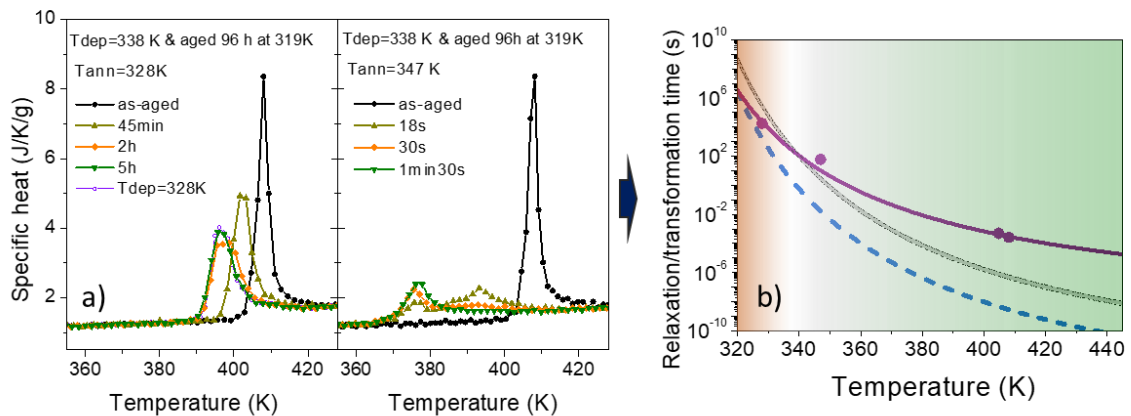


Figure 8. 3. a) Specific heat traces obtained at $3 \times 10^4 K/s$ after different annealing treatments of samples deposited at $1.05T_g$, fast cooled and aged at 319K for 4 days. The annealing temperatures and times are indicated in the legend. Left panel: The overlap between the curve corresponding to a sample deposited at 328K and the one annealed for 5h at 328 K indicates that after this time, the glass has fully transformed and reached equilibrium. b) curves corresponding to the alpha relaxation time of the liquid (dash-blue) [13], the relaxation time of the glass (purple) [9], and the line corresponding to the crossover relaxation time calculated as $\tau_{glass,crossover} = (180 \pm 60)\tau_\alpha$ (grey). Purple circles correspond to transformation time data obtained from the calorimetric curves using the approaches explained in the main text.

In Figure 8.3b, we represent the relaxation times of the liquid and the glass (for a glass with $T_f=319K$), the transformation times obtained from the calorimetric curves and the

crossover relaxation time as in Figure 8.1b. The transformation times at 328K (cooperative dynamics on the whole sample) and 347K (localized heterogeneous dynamics & facilitation) fall respectively at left and right of the crossover line ($\tau_{glass,crossover} = (180 \pm 60)\tau_\alpha$), consistent with the transition mechanism observed during the annealing treatments (Figure 8.3a) and providing solidity to the assumption that this crossover curve is independent of the characteristics of the glass. Looking at Figure 8.3b we can observe that according to our estimation, for this particular glass, since its stability is high ($T_f=319K$), the annealing temperatures required to exclusively see the cooperative relaxation would be below 338K (intersection between crossover relaxation time and relaxation time of the glass). In fact, the higher the stability of the glass, the lower the crossover temperature. This is even clearer in the case of the ultrastable glass. Figure 8.4a shows the calorimetric traces for a sample vapor deposited at $T_{dep}=285K$ ($0.85T_g$), temperature at which the glass attains the maximum kinetic and thermodynamic stability [19,20], after annealing at 347K (T_g+14K) for different times. At this annealing temperature, the ratio $\tau_{glass}/\tau_\alpha \approx 2 \times 10^6$ and the transformation is clearly dominated by the formation and expansion of liquid patches in the glass. Looking at a similar scheme than in Figures 8.1b and 8.3b, one can see in the inset of Figure 8.4b that we would need to perform annealing treatments at $T < 300K$ (33K below T_g) with unreachable transformation times above $10^{27}s$ to transform the glass by cooperative gradual softening when considering the VFT extrapolation of the τ_α .

The crossover line between these two mechanisms can be rationalized by considering the intrinsic dynamical heterogeneity of the supercooled liquid state. Even though the characteristic time of the relaxation of a liquid is monitored via a single value of structural relaxation for each temperature, the true relaxation proceeds via non-stretched exponential decay of dynamic correlations in spontaneous density fluctuations. The relaxation dynamics of the SCL is typically obtained by dielectric spectroscopy, where this relaxation is manifested as a peak in the complex part of the permittivity of the sample (dielectric loss). While the maximum of this peak is regarded as the (main) relaxation time of the system (τ_α), its width is strongly influenced by the dynamical heterogeneities in the SCL. As a consequence, even after a time τ_α , parts of the SCL are still not relaxed, corresponding to the low frequency side of the dielectric loss, which for most glass-formers, but in particular for TPD, spreads along two orders of magnitude above the

maximum of the peak (alpha relaxation value) [21]. Interestingly, this value is consistent with the observation of the crossover time of $(180 \pm 60)\tau_\alpha$.

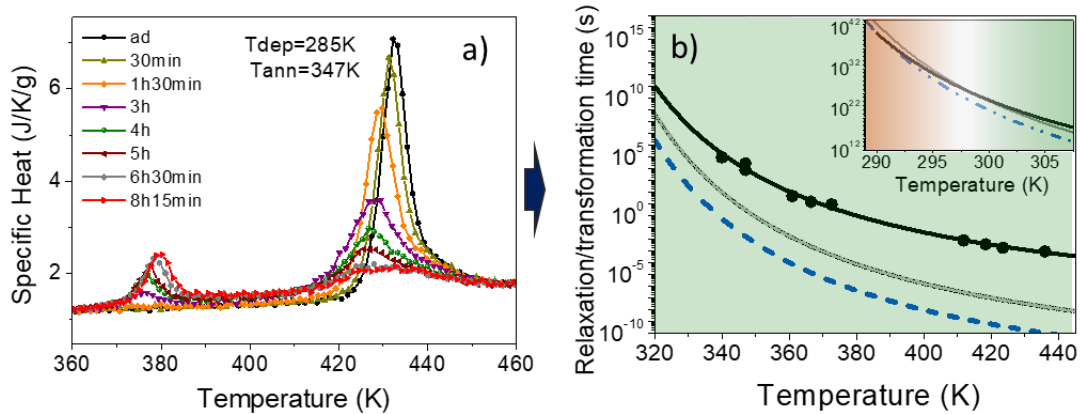


Figure 8. 4. a) Specific heat traces obtained at 3.5×10^4 after different annealing treatments of samples deposited at $0.85T_g$ (285 K) and annealed at 347 K. The annealing times are indicated in the legend. b) curves corresponding to the alpha relaxation time of the liquid (dash-blue) [13], the relaxation time of the glass (black) [9], and the line corresponding to the crossover relaxation time calculated as $\tau_{glass} = (180 \pm 60)\tau_\alpha$ (grey). Black dots correspond to experimental transformation time, extracted from Rodríguez-Tinoco *et al.* [10]. Transformation time at 347 K is obtained from the data of the a) panel. The inset shows the same curves but in a lower temperature range, so the crossover point can be depicted.

Under this view, we could interpret that if the relaxation time of the glass is inside the distribution of relaxation times of the liquid, the whole system relaxes as a SCL would do, i.e. via a cooperative relaxation mechanism with no distinguishable liquid clusters. In other words, the glass will present a cooperative relaxation mechanism at a certain temperature as long as the glass relaxation time is comparable with the values of the relaxation time of the liquid, taking into account that in the liquid we have a dispersion of relaxation times. Thus, seeing or not this mechanism will depend strongly on the stability of the glass and the measuring temperature. We speculate the two regions (green and orange) highlighted in Figures 8.1b, 8.3b, and 8.4b could also be rationalized from a length scale perspective. That is, distinguishable liquid regions could be identified only if the average distance between them is much larger than the correlation length of dynamic heterogeneities [22].

The relaxation time of the glass at the crossover temperature may have been the major handicap for observing experimentally these liquid regions during the glass transition. The lower the stability of the glass, the higher the crossover temperature and, therefore,

the faster the transformation time of the glass. In the case of the glass deposited at $0.99T_g$ for instance, the crossover occurs for transformation times of the order of a few seconds. For a conventional glass cooled at -10K/min with $\tau_\alpha \approx 100\text{s}$ at T_g , nucleation and growth-like behavior would be identified only at temperatures above 359K , with transformation times around several milliseconds. Since conventional calorimetry is unable to work in these short time scales, most of the experiments up to now were limited to temperatures near T_g (at the left side of the crossover) and therefore, only the cooperative relaxation mechanism had been observed in glasses so far. Now with the general availability of fast scanning calorimetry short time scales are within reach and it would be interesting to carry out measurements far from equilibrium to test the occurrence of similar behavior in other glassy systems.

8.3 Summary

In this chapter we have seen that glasses transform into the super cooled liquid via two different mechanisms depending on their stability and the temperature of the measurement. This work provides conclusive experimental evidence to test theories of the glass transition and is compatible with models that include heterogeneous dynamics and dynamic facilitation and predict the formation of distinct liquid regions when there exists a large contrast between the mobility of the equilibrated liquid and the glass. We have also shown that the ratio of τ_{glass}/τ_α at a given temperature appears to be a good indicator to predict the mechanism of the transformation. Importantly, the existence of the two regimes identified in this work is independent of the experimental procedure or protocol to produce the glass but their exploration may require the use of ultrafast experimental techniques to identify the liquid regions.

References

- [1] V. Lubchenko, *Theory of the Structural Glass Transition: A Pedagogical Review*, Adv Phys **64**, 283 (2015).
- [2] P. G. Wolynes, *Spatiotemporal Structures in Aging and Rejuvenating Glasses*, Proc Natl Acad Sci U S A **106**, 1353 (2009).
- [3] I. Douglass and P. Harrowell, *Can a Stable Glass Be Superheated Modelling the Kinetic Stability of Coated Glassy Films*, Journal of Chemical Physics **138**, (2013).
- [4] R. Gutiérrez and J. P. Garrahan, *Front Propagation versus Bulk Relaxation in the Annealing Dynamics of a Kinetically Constrained Model of Ultrastable Glasses*, Journal of Statistical Mechanics: Theory and Experiment **2016**, 074005 (2016).
- [5] M. Lulli, C. S. Lee, H. Y. Deng, C. T. Yip, and C. H. Lam, *Spatial Heterogeneities in Structural Temperature Cause Kovacs' Expansion Gap Paradox in Aging of Glasses*, Phys Rev Lett **124**, (2020).
- [6] R. L. Jack and L. Berthier, *The Melting of Stable Glasses Is Governed by Nucleation-and-Growth Dynamics*, Journal of Chemical Physics **144**, (2016).
- [7] C. J. Fullerton and L. Berthier, *Density Controls the Kinetic Stability of Ultrastable Glasses*, EPL (Europhysics Letters) **119**, 36003 (2017).
- [8] M. D. Ediger, *Perspective: Highly Stable Vapor-Deposited Glasses*, Journal of Chemical Physics **147**, (2017).
- [9] C. Rodríguez-Tinoco, J. Ràfols-Ribé, M. González-Silveira, and J. Rodríguez-Viejo, *Relaxation Dynamics of Glasses along a Wide Stability and Temperature Range*, Sci Rep **6**, 35607 (2016).
- [10] C. Rodríguez-Tinoco, M. Gonzalez-Silveira, J. Ràfols-Ribé, A. Vila-Costa, J. C. Martinez-Garcia, and J. Rodríguez-Viejo, *Surface-Bulk Interplay in Vapor-Deposited Glasses: Crossover Length and the Origin of Front Transformation*, Phys Rev Lett **123**, (2019).
- [11] A. Sepúlveda, M. Tylinski, A. Guiseppi-Elie, R. Richert, and M. D. Ediger, *Role of Fragility in the Formation of Highly Stable Organic Glasses*, Phys Rev Lett **113**, 45901 (2014).
- [12] U. S. Cubeta and V. Sadtchenko, *Glass Softening Kinetics in the Limit of High Heating Rates*, J Chem Phys **150**, 094508 (2019).
- [13] D. M. Walters, R. Richert, and M. D. Ediger, *Thermal Stability of Vapor-Deposited Stable Glasses of an Organic Semiconductor*, J Chem Phys **142**, 134504 (2015).
- [14] M. Chonde, M. Brindza, and V. Sadtchenko, *Glass Transition in Pure and Doped Amorphous Solid Water: An Ultrafast Microcalorimetry Study*, J Chem Phys **125**, 094501 (2006).
- [15] A. Cavagna, *Supercooled Liquids for Pedestrians*, Phys Rep **476**, 51 (2009).
- [16] Z. Wojnarowska, K. Adrjanowicz, P. Wlodarczyk, E. Kaminska, K. Kaminski, K. Grzybowska, R. Wrzalik, M. Paluch, and K. L. Ngai, *Broadband Dielectric Relaxation Study at Ambient and Elevated Pressure of Molecular Dynamics of Pharmaceutical: Indomethacin*, J Phys Chem B **113**, 12536 (2009).

- [17] C. A. Angell, *Entropy and Fragility in Supercooling Liquids*, J Res Natl Inst Stand Technol **102**, 171 (1997).
- [18] J. Zhao, S. L. Simon, and G. B. McKenna, *Using 20-Million-Year-Old Amber to Test the Super-Arrhenius Behaviour of Glass-Forming Systems*, Nat Commun **4**, 1783 (2013).
- [19] J. Ràfols-Ribé, A. Vila-Costa, C. Rodríguez-Tinoco, A. F. Lopeandiá, J. Rodríguez-Viejo, and M. Gonzalez-Silveira, *Kinetic Arrest of Front Transformation to Gain Access to the Bulk Glass Transition in Ultrathin Films of Vapour-Deposited Glasses*, Physical Chemistry Chemical Physics **20**, 29989 (2018).
- [20] S. S. Dalal, D. M. Walters, I. Lyubimov, J. J. de Pablo, and M. D. Ediger, *Tunable Molecular Orientation and Elevated Thermal Stability of Vapor-Deposited Organic Semiconductors*, Proceedings of the National Academy of Sciences **112**, 4227 (2015).
- [21] C. Rodríguez-Tinoco, M. Rams-Baron, J. Rodríguez-Viejo, and M. Paluch, *Emergence of a Substrate-Temperature-Dependent Dielectric Process in a Prototypical Vapor Deposited Hole-Transport Glass*, Sci Rep **8**, 1380 (2018).
- [22] M. D. Ediger, *Spatially Heterogeneous Dynamics in Supercooled Liquids*, Annu Rev Phys Chem **51**, 99 (2000).

Chapter 9

Summary

Glasses are ubiquitous systems in our daily life, being present in very diverse applications from simple tableware appliances to leading technology devices, and yet their nature is not fully understood. In particular, both the transition from the metastable equilibrium state (liquid) to the out-of-equilibrium state (glass) and the reverse process, i.e., the transition from glass to liquid, are some of the most intriguing phenomena in the field of solids physics up to this day. In this work, we focus on the latter, and we explore the rich phenomenology behind the transition back to equilibrium of a previously arrested state. The main objective of this work was to deepen our knowledge on the bulk transformation mechanism by which thin film glasses transit into the equilibrium supercooled liquid phase after an up jump in temperature. Since in thin film glasses (especially those with higher stabilities) the surface effects induce the transformation, precluding the study of the intrinsic bulk transformation of the glass, we focused our study in capped vapor-deposited glasses, making use of the capping strategy to gain access to the bulk transition of the material.

In the last years, vapor deposition has emerged as a powerful strategy to produce glasses of unprecedented stability. Moreover, the possibility to tune the deposition conditions allows to tailor glasses with a wide range of stabilities, as well as different layer configurations, very useful for optoelectronic applications for example. Making it also the ideal tool to prepare capped glasses. In this work, we use physical vapor deposition to grow capped TPD films at a wide range of deposition temperatures (from $0.85T_g$ to $1.02T_g$) and at slow deposition rates, 0.08nm/s, allowing the study of the bulk transformation in glasses with a wide range of stabilities. As capping material, TCTA has

been used on the free surface and the interface with the substrate, ensuring the suppression of the propagating fronts.

The main technique used to characterize the samples studied in this work is quasi-adiabatic fast-scanning nanocalorimetry. This technique has proven to be extremely useful to evaluate different aspects of the mechanisms behind the glass transition thanks, mostly, to the high heating rates employed during heating scans. The high heating rates shift the devitrification of the glass to temperatures much higher than the ones reached using other conventional techniques (such as conventional DSC), allowing us to study aspects of the transformation that can only be observed if high enough mobility contrast between the different dynamical regions in the glass can be granted. In addition, the sensitivity of the technique allows measuring very low masses, that is the energy involved in the glass transition of glasses with thicknesses in the order of only a few nanometers, i.e. masses of around 1-2 ng.

Blocking the surface mobility of thin film glasses has shown to play a critical role in the way vapor-deposited glasses transform into the liquid phase when heated well above their limiting fictive temperature. While non-capped thin film stable glasses are characterized for transforming into the liquid phase via propagating fronts that start at the free surface/interface with the substrate and penetrate into the glass at a constant rate, capped glasses have shown to follow a bulk like transformation that takes place in the whole volume of the sample.

In this work, we have seen that, when eliminating the surface influence on the glass transformation, the bulk transformation takes place via two competing processes when annealed at a constant temperature well above the fictive temperature of the glass: i) the emergence and growth of equilibrated liquid regions inside the glass that grow by means of kinetic facilitation and ii) the progressive softening of the remaining untransformed glass.

The emergence and growth of the liquid regions has been mainly inferred from the calorimetric trace of the devitrification process after thermal annealing the samples for different amounts of time. This allows to distinguish and monitor the formation of liquid regions inside the glass from the appearance of a second devitrification peak at lower temperatures that increases in area with annealing time. Studying the evolution of the

transformed liquid fraction as a function of time with the KJMAE model we are able infer in an approximate way the dynamics of the transformation.

Using this model, we observed that thin film ultrastable glasses transform into the liquid phase following a nucleation and growth like kinetics with 2D growth of the equilibrated regions. The total number of these liquid regions has shown to vary along the transition, starting from a small number of pre-existing sites and then increasing as more areas of the glass achieve equilibrium, having a certain non-null nucleation rate. Although the origin of the pre-existing liquid sites is still not completely understood, we attribute it to the existence of regions with more mobility due to defects on the surface of the substrate or temperature inhomogeneities during the deposition of the sample.

One of the most remarkable results regarding these equilibrated regions inside the glass is the gigantic length scales corresponding to the separation distance between the initiation sites, of the order of 2-5 μm (in the case of highly stable glasses). These results agree with the observations made by means of atomic force microscopy (AFM), technique that allows a direct visualization of the equilibrated liquid regions and their evolution thanks to the wrinkling patterns formed on the top TCTA layer due to thermal stress.

Using this technique, we could obtain direct visual confirmation of the presence of a small number of pre-existing nuclei (where the transformation seems to start), as well as the emergence of new equilibrated regions with annealing time and the huge separation between equilibrated regions in the first stages of the transformation. From the AFM measurements we were also able to evaluate the growth rate of the liquid regions inside the glass. Interestingly, this study showed that the equilibrated liquid grows at an average velocity that matches well with the velocity obtained for the propagating fronts in non-capped samples at that specific temperature.

Changing the stability of the glass by growing the samples at different deposition temperatures, we are able to study how stability affects the bulk transformation dynamics. We have found that, independently of the stability of glass, the dominating transformation mechanism after a temperature jump well above T_g is the formation and 2D growth of equilibrated liquid regions. In this case, the nucleation rate increases sharply the lower the stability of the glass. As a consequence, the number of nucleation sites increases considerably and the distance between them is strongly reduced (~20nm for glasses deposited at 325K). This result agrees with previous studies that reported a higher number

of high mobility regions in glasses equilibrated at higher temperatures (therefore, less stable).

In parallel, the initial glass that does not transform into the liquid phase during the isotherms (glass matrix or remaining stable glass) goes through a partial softening that can be evaluated by measuring the shift to lower temperature of the corresponding endothermic peak. This mechanism has shown to be almost negligible for ultrastable glasses, however it gains importance the lower the stability of the glass. Up to the point to observe that depending on the stability of the glass and the temperature of the annealing treatment, the softening is the only apparent transformation mechanism.

We propose that the appearance of equilibrated regions during the glass transition can be rationalized from the ratio between the relaxation time of the glass and the alpha relaxation time of the liquid ($\tau_{glass}/\tau_{\alpha}$) at the temperature of the isothermal treatment.

If this ratio is big, the samples transform dominated by the appearance of liquid regions, since their emergence and growth rate is way higher than the relaxation time of the glass matrix. However, if the ratio is small, we are not able to distinguish the appearance of liquid regions since the cooperative dynamics across the sample are fast enough to dominate the transition. In this sense, we have observed how in highly stable glasses the transformation is clearly dominated by the formation and expansion of liquid patches in the glass and the effect of the softening of the glass matrix is practically negligible. However, as stability is decreased, if the annealing temperature is kept unchanged, the cooperative dynamics start to gain a more important role, up to the point where, if the ratio $\tau_{glass}/\tau_{\alpha}$ is small enough, a change in the transformation mechanism can be appreciated: we stop observing a transition with a clear phase separation between the transformed liquid regions and the softening glass matrix, and start seeing a transition mainly dominated by the cooperative dynamics across the film (no phase separation).

The crossover line between these two mechanisms can be rationalized by considering the intrinsic dynamical heterogeneities of the supercooled liquid state. As it is commonly known, although glasses are usually defined by a single structural relaxation time or fictive temperature, they should be described as a mosaic of regions with a certain distribution of relaxation times (or spontaneous density fluctuations in the RFOT theoretical framework). Therefore, the requisite to observe one mechanism or the other is mainly the mobility contrast between the dynamic heterogeneities intrinsic in our glass at

a certain temperature. This contrast can be achieved by measuring at temperatures far above the fictive temperature of the glass, which is easily achieved for highly stable glasses, but requires temperatures much higher than T_g in the case of conventional glasses. Interestingly, we have observed that the existence of the two regimes is independent of the experimental procedure to produce the glass (by physical vapor deposition or by cooling from the liquid phase).

The results presented in this work, provide new insights into the processes behind the glass transition, its transformation mechanism and the main parameters describing the transformation towards equilibrium, establishing new paths on the way to deepen our knowledge in one of the topics most studied and still poorly understood in the field of solids physics.

More specifically, this work opens a path to explore, for example, the relaxation dynamics in glasses with different stabilities and visualize the impact that parameters such as the nanostructure of the sample, surface defects on the substrate or distance between equilibration sites, have on the relaxation mechanism of the glass. It allows also for a direct manipulation of the characteristic microstructure of the sample, granting us the possibility of tailoring glasses with specific structures depending on the future application.

From another perspective, this work also opens the path to a better understanding of the nature of the glass transition as a kinetic or thermodynamic phenomenon. The possibility of establishing a relationship between stability and the length scales involved in the transition can provide a new perspective to the analysis of the glass transition as a critical phenomenon establishing a relation with a thermodynamic (first order) transition at a finite temperature.

List of publications

- J. Ràfols-Ribé, A. Vila-Costa, C. Rodríguez-Tinoco, A.F. Lopeandía, J. Rodríguez-Viejo, M. Gonzalez-Silveira. “Kinetic arrest of front transformation to gain access to the bulk glass transition in ultrathin films of vapour-deposited glasses”. In: *Phys. Chem. Chem. Phys.*, 2018, **20**, 29989-29995.
- A. Vila-Costa, J. Ràfols-Ribé, M. Gonzalez-Silveira, A. Lopeandía, J. Ll. Tamarit, J. Rodríguez-Viejo. “Multiple glass transitions in vapor-deposited orientational glasses of the most fragile plastic crystal Freon 113”. In: *Phys. Chem. Chem. Phys.*, 2019, **21**, 10436-10441
- C. Rodríguez-Tinoco, M. Gonzalez-Silveira, J. Ràfols-Ribé, A. Vila-Costa, J.C. Martinez-Garcia, J. Rodríguez-Viejo. “Surface-bulk interplay in vapor-deposited glasses: crossover length and the origin of front transformation”. In: *Phys. Rev. Lett.* **123**, 155501 (2019).
- A Vila-Costa, Joan Ràfols-Ribé, M González-Silveira, AF Lopeandia, Ll Abad-Muñoz, J Rodríguez-Viejo. “Nucleation and growth of the supercooled liquid phase control glass transition in bulk ultrastable glasses”. In: *Phys. Rev. Lett.* **124**, 076002 (2020).
- A. Vila-Costa, M. Gonzalez-Silveira, C. Rodríguez-Tinoco, M. Rodríguez-López, J. Rodríguez-Viejo. “Emergence of equilibrated liquid regions within the glass”. In: *Nature Physics* (2022).
- J. Alcalá, T. Bar, J. Fraxedas, M. Gonzalez-Silveira, J. A. Plaza, C. Rodriguez-Tinoco, J. Rodríguez-Viejo, M. Ruiz-Ruiz, A. Vila-Costa (in alphabetical order). “Microscopic view of the relaxation of an ultrastable glass”. Submitted.
- A. Vila-Costa, M. Gonzalez-Silveira, C. Rodríguez-Tinoco, J. Rodríguez-Viejo. “Effect of stability on the bulk transformation dynamics”. In preparation.